AD-A118 091 SANTA BARBARA RESEARCH CENTER GOLETA CALIF F/G 17/5
DEVELOPMENT OF LARGE AREA PV HGCDTE DETECTORS FOR 10.6 MICROMET--ETC(U)
JUN 80 P R BRATT, K J RILEY
UNCLASSIFIED DAAB07-76-C-0803
NL

1 of 2
AD A
118091

(12)

DEVELOPMENT OF LARGE AREA PV HgCdTe DETECTORS FOR 10.6 μm

Santa Barbara Research Center
75 Coromar Drive
Goleta, CA 93017

30 June 1980

Final Report
For Period 15 June 1977 to 30 January 1979

Contract Number DAAB07-76-C-0803

Prepared for

U.S. Army Electronics
Research and Development Command
Laser Division, DELNV-L
U.S. Army Night Vision and Electro-Optics Laboratory
Fort Belvoir, Virginia 22060

NOTICES

UNCLASSIFIED
SECURITY CLASSIFICATION OF THIS PAGE (When Data Entered)

REPORT DOCUMENTATION PAGE		READ INSTRUCTIONS BEFORE COMPLETING FORM
1. REPORT NUMBER	2. GOVT ACCESSION NO. AD-A118091	3. RECIPIENT'S CATALOG NUMBER
4. TITLE (and Subtitle) Development of Large Area PV HgCdTe Detectors for 10.6 µm		5. TYPE OF REPORT & PERIOD COVERED Final Report 15 June 1977 to 30 Jan 1980
		6. PERFORMING ORG. REPORT NUMBER
7. AUTHOR(s) P. R. Bratt and K. J. Riley		8. CONTRACT OR GRANT NUMBER(s) DAAB07-76-C-0803
9. PERFORMING ORGANIZATION NAME AND ADDRESS Santa Barbara Research Center 75 Coromar Drive Goleta, California 93117		10. PROGRAM ELEMENT, PROJECT, TASK AREA & WORK UNIT NUMBERS CLIN 0011/B002
11. CONTROLLING OFFICE NAME AND ADDRESS U. S. Army ERADCOM Fort Monmouth, NJ 07703		12. REPORT DATE 30 June 1980
		13. NUMBER OF PAGES 108
14. MONITORING AGENCY NAME & ADDRESS(if different from Controlling Office) U.S. Army NVEOL Laser Division, DELNV-L Fort Belvoir, VA 22060		15. SECURITY CLASS. (of this report) Unclassified
		15a. DECLASSIFICATION/DOWNGRADING SCHEDULE

16. DISTRIBUTION STATEMENT (of this Report)

Approved for public release, distribution unlimited

17. DISTRIBUTION STATEMENT (of the abstract entered in Block 20, if different from Report)

18. SUPPLEMENTARY NOTES

19. KEY WORDS (Continue on reverse side if necessary and identify by block number)

HgCdTe, photodiodes, photovoltaic detectors, laser detectors, quadrant arrays.

20. ABSTRACT (Continue on reverse side if necessary and identify by block number)

The purpose of this program was to develop large area PV HgCdTe detectors for laser receiver systems operating at 10.6 µm. The work accomplished included: growth of HgCdTe single-crystal material by two different methods; design and fabrication of quadrant detector arrays with elemental areas of 1×1 mm^2 and 2×2 mm^2 per quadrant; test and evaluation of quadrant arrays; and packaging of quadrant arrays in evacuated glass/metal

dewars with J-T cryostats for cooling and four-channel preamplifiers for laboratory or field operation.

HgCdTe crystals were produced by both zone melting and solid-state recrystallization processes. Either technique yielded sufficient single-crystal material to fabricate the large area arrays in monolithic form. The uniformity of alloy composition was adequate to give nearly identical spectral response characteristics for each detector quadrant.

Quadrant detector arrays in the 1×1 mm^2 size were producing having D*(10.6 μm, 1 MHz) values in the range 2 to 4×10^{10} cm Hz$^{1/2}$/watt when operated at 80°K under 2π steradian FOV conditions. The uniformity of sensitivity was better than ±5% within each quadrant. Quantum efficiencies averaged around 60%. Analysis of detector and preamplifier noise contributions showed that D* could be improved by about a factor of 2 with a reduction in FOV and use of a cold bandpass filter.

Quadrant detector arrays in the 2×2 mm^2 size were not as successful. The uniformity of sensitivity was poor and D*(10.6 μm, 1 MHz) values were about 4×10^{9} cm Hz$^{1/2}$/watt. Effective quantum efficiencies (averaged over the 2×2 mm^2 area) were only 3 to 4%. The problem was found to be due to the sheet resistance of the top n-layer of the p-n junction being of the same order of magnitude or greater than the junction resistance. Technical approaches to mitigate this problem are known, but further technology development will be necessary to effect a solution.

Two quadrant arrays of 1×1 mm^2 detectors and one array of 2×2 mm^2 detectors were assembled in glass/metal vacuum dewars equipped with Joule-Thomson expansion cryostats for cooling to 80°K. These were delivered to the U.S. Army along with two four-channel high speed (10 MHz) preamplifiers.

PREFACE

The work documented in this report was performed at Santa Barbara Research Center over the period from 15 June 1977 to 30 January 1979 under Contract No. DAAB07-76-C-0803 with the U.S. Army Electronics Command, Fort Monmouth, NJ. The program technical monitor at Fort Monmouth was C. E. Loscoe.

A previous interim report described work performed on large area PV HgCdTe detectors for wavelengths of 2.06 and 3.85 µm. This final report describes work performed on large area PV HgCdTe detectors for 10.6 µm.

Major technical contributions to the detector work were made by P. R. Bratt, D. W. Goebel, J. M. Myrosznyk, S. L. Price, K. J. Riley, and G. G. Silvestri. R. A. Cole directed the work on HgCdTe crystal growth. Preamplifier design and fabrication were under the direction of J. S. Lee and S. P. Ryan, III. C. L. Anderson at Hughes Research Laboratories provided valuable technical consultation and direction of the ion implantation work which was done at the Research Laboratories. P. R. Bratt was the program manager for Santa Barbara Research Center. D. E. Bode provided valuable assistance in preparation of this final report.

CONTENTS

ILLUSTRATIONS

ILLUSTRATIONS (Cont)

ILLUSTRATIONS (Cont)

TABLES

Section 1

INTRODUCTION AND SUMMARY

The objective of this program was to develop technology for the fabrication of large area, fast response HgCdTe photovoltaic (PV) detectors for laser applications. Initial phases of this project focused on detectors for the wavelengths 2.06 and 3.85 μm.

This work was successfully completed 15 June 1977 and an interim report was published[1] that summarized the details of this early effort and presented the data for the demonstration quadrant arrays that were fabricated and delivered. A paper was also presented at the IRIS Detector Specialty Group Meeting at the Air Force Academy in Colorado Springs in March 1977 which described a portion of this work.[2] A reprint of this paper is included in this report as Appendix A.

Subsequent work on this program was directed toward large area photodiode development for laser receivers operating at 10.6 μm. The technical approach was to optimize the material technology for the preparation of large uniform single crystals of HgCdTe and to optimize the device technology for the fabrication of high-speed low-capacitance diodes suitable for a quadrant detector array configuration.

The design goals for these quadrant arrays were:

1. Sensitive area 1× 1 mm^2 and 2× 2 mm^2 in each quadrant
2. Separation between quadrant segments ≤ 0.1 mm
3. Uniformity of responsivity within and between quadrant elements of ±10%.

---

[1] P. R. Bratt, "Development of Large Area PV HgCdTe Detectors for 2.06 and 3.85 μm," Interim Report on Contract No. DAAB07-76-C-0803 for U.S. Army ERADCOM, Laser Division, DELNV-L, Ft. Monmouth, NJ, 31 May 1978.

[2] Meeting of the IRIS Specialty Group on Infrared Detectors - Volume 1, November 1977, p. 221 (Unclassified).

4. Frequency response to 2.5 MHz
5. D*(10.6 μm, 2.5 MHz) ≥ 4× 10^9 cm $Hz^{\frac{1}{2}}$/watt
6. Peak responsivity at 10.6 μm at 77 °K.

Quadrant arrays of 1× 1 mm^2 detectors gave performance well in excess of these design goals. D*(10.6 μm, 2.5 MHz) values gerater than 1× 10^{10} cm-$Hz^{\frac{1}{2}}$/watt were achieved. Two quadrant arrays were fabricated and assembled into permanently evacuated glass dewars utilizing Joule-Thomson cryostats for cooling to approximately 80 °K. These were delivered to the Army along with a four-channel current-mode preamplifier. The results of this work were presented at an IRIS Detector Specialty Group Meeting held at Annapolis, MD, in June 1978.[3] A reprint of this paper is included as Appendix B of this Report.

Attempts to scale up the detector size to 2× 2 mm^2 per quadrant wei not as successful. D*(10.6 μm, 1 MHz) values achieved with these larger detector areas were in the low 10^9 cm $Hz^{\frac{1}{2}}$/watt range and the uniformity of response over the sensitive area was very poor. Analysis of this problem showed that it was due to high sheet resistance in the ion-implanted n-type layer relative to the junction resistance. Thus, photocurrents generated at points far removed from the top metal contact are not able to reach the contact where they would produce a signal current in the external circuit. A number of technical approaches to solve this problem were devised. However, the project funding was exhausted before a satisfactory solution could be implemented.

The remaining sections of this report describe the theory of PV detector operation, HgCdTe material preparation and evaluation methods, PV detector fabrication, detector test and evaluation, and conclusions and recommendations for future work.

---

[3] Joint Meeting of the IRIS Specialty Group on Infrared Detectors and Imaging - Volume 1, August 1978, p. 333 (Unclassified).

Section 2

THEORY OF DETECTOR OPERATION

In this section the physical theory of operation of a PV detector is described. The design features that are important for obtaining good high-frequency performance from large area detectors are noted. A parametric analysis of $D^*(\lambda_p)$ versus frequency which includes the preamplifier noise contribution is also presented.

DETECTIVITY

The detectivity at wavelength λ for a PV detector can be expressed by the equation

$$D^*(\lambda) = \frac{\eta e \lambda \sqrt{A}}{hc\ i_n/(\Delta f)^{\frac{1}{2}}} \tag{1}$$

where η = quantum efficiency
e = electronic charge
λ = wavelength
h = Planck's constant
c = speed of light
A = sensitive area
$i_n/(\Delta f)^{\frac{1}{2}}$ = rms noise current per unit bandwidth

The two important quantities in this equation are the quantum efficiency and the noise current.

Quantum Efficiency

The quantum efficiency of the detector is controlled by optical reflection loss at the front surface and by the efficiency with which minority carriers are collected at the p-n junction. By applying an antireflection coating to the front surface, reflection loss can be limited to less than 5%. The minority collection efficiency depends on the minority carrier diffusion length

$$L = \left(\frac{\mu \tau k T}{e}\right)^{\frac{1}{2}} \tag{2}$$

where μ = minority carrier mobility

τ = minority carrier lifetime

k = Boltzmann's constant

T = absolute temperature

Only those minority carriers generated within a diffusion length of the junction are likely to be collected and measured as a photosignal. The situation is diagrammed in Figure 2-1. Radiation incident through the front surface of the PV detector is absorbed and decays away in exponential fashion. Minority electrons generated on the p side within a diffusion length L_n of the p-n junction will be collected. Minority holes generated on the n side within a diffusion length L_p of the junction will also be collected.

Location of the junction at an appropriate depth below the top surface of the device is also important. Since 90% of the radiation is absorbed in a distance $2/\alpha$ and α is on the order of 5×10^3 cm^{-1} for HgCdTe, the region over which absorption is essentially complete is 4 μm. By proper location of the p-n junction within this absorption region, collection efficiencies can

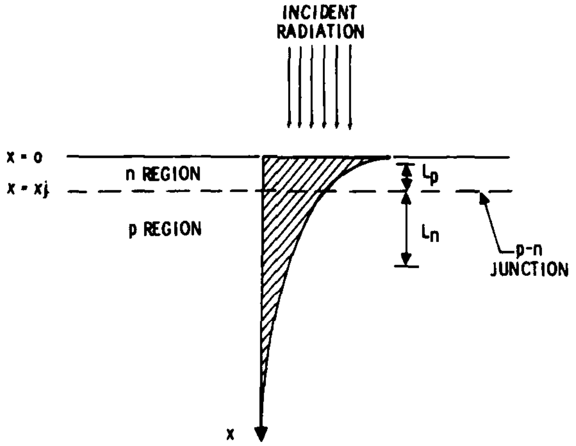

Figure 2-1. Diagram Showing Absorption of Radiation (Shaded Region) in a PV Detector in Relation to the p-n Junction

be in the range 0.5 to 0.9. Thus overall quantum efficiencies should be in the range of 0.5 to 0.8.

Noise Current

The total rms noise current per unit bandwidth originating in the PV detector is given by[4]

$$\frac{i_n}{(\Delta f)^{\frac{1}{2}}} = \left\{\frac{2eI_s}{\beta}\left[\exp\left(\frac{eV}{\beta kT}\right) + 1\right] + 2eI_p + \frac{4kT}{R_s} + \frac{1}{f}\text{ term}\right\}^{\frac{1}{2}} \qquad (3)$$

where I_s = diode saturation current

V = applied voltage across junction

k = Boltzmann's constant

T = absolute temperature

β = a factor between 1 and 2 depending on the generation-recombination current in the space charge layer of the p-n junction

I_p = dc photocurrent due to background photon flux

R_s = diode shunt resistance

f = frequency

It is seen that there are four contributions to the total noise current. These are, in the order in which they appear on the right hand side of equation (3):

1. The shot noise current from thermally generated carriers which diffuse to the junction
2. The shot noise current from background photogenerated carriers which diffuse to the junction
3. The Johnson noise of the shunt resistance
4. 1/f noise due to surface states or other sources

One of the main objectives of the detector engineer is to design the PV detector so as to minimize its noise current and thereby maximize detectivity. From the noise equation, it can be seen how this may be done. Thermally generated shot noise can be minimized by reducing the saturation current I_s.

---

[4] G. R. Pruett and R. L. Petritz, Proc. IRE 47, 1524 (1959).

Background photon generated shot noise is minimized by operating under reduced background photon flux conditions where possible (i. e., cold filters, cold FOV shields, etc.). Surface shunt resistance is made as large as possible by suitable surface passivation treatments and these also may, in some cases, serve to reduce 1/f noise.

The saturation current is controlled by a number of semiconductor properties and is composed of two terms, here expressed as current densities,

$$J_s = J_{diff} + J_{gr} \tag{4}$$

where J_s = saturation current density
J_{diff} = diffusion component
J_{gr} = generation-recombination component.

The diffusion component of the saturation current density is due to thermally generated minority carriers which cross the junction and has been shown to be[5]

$$J_{diff} = e\left\{p\left(\frac{\mu_p k T}{\tau_p e}\right)^{\frac{1}{2}} + n\left(\frac{\mu_n k T}{\tau_n e}\right)^{\frac{1}{2}}\right\} \tag{5}$$

where n = electron concentration on p-side $\approx n_i{}^2/N_A$
μ_n = mobility of electron on p-side
τ_n = lifetime of electron on p-side
p = hole concentration on n-side $\approx n_i{}^2/N_D$
μ_p = mobility of hole on n-side
τ_p = lifetime of hole on n-side
N_A = net acceptor concentration on p-side
N_D = net donor concentration on n-side
n_i = intrinsic carrier concentration

---

[5] W. Shockley, Bell Syst. Tech. J. 28, 435 (1949).

However, this equation holds only for the case where the thickness of the n- and p-regions on either side of the junction is much greater than the minority carrier diffusion length. For PV detectors this is frequently not the case and the equation for the diffusion current must be modified to the form

$$J_{diff} = \frac{e D_p p}{L_p}\left[\frac{(D_p/L_p)\tanh(x_n/L_p) + S_n}{(D_p/L_p) - S_n \tanh(x_n/L_p)}\right] + \frac{e D_n n}{L_n}\left[\frac{(D_n/L_n)\tanh(x_p/L_n) - S_p}{(D_n/L_n) - S_p \tanh(x_p/L_n)}\right] \tag{6}$$

where D_p = hole diffusion coefficient ($\mu_p kT/e$)
L_p = hole diffusion length [see equation (2)]
x_n = thickness of n-region
S_n = surface recombination velocity for n-region
D_n = electron diffusion coefficient ($\mu_n kT/e$)
L_n = electron diffusion length [see equation (2)]
x_p = thickness of p-region
S_p = surface recombination velocity for p-region

It can be seen that, for the case where $x_n >> L_p$ and $x_p >> L_n$, the tanh terms are approximately unity and equation (6) reduces to

$$J_{diff} = \frac{e D_p p}{L_p} + \frac{e D_n n}{L_n} \tag{7}$$

which is the same as equation (5). On the other hand, when $x_n \leq L_p$ and $x_p \leq L_n$, we have

$$J_{diff} = \frac{e D_p p}{L_p}\tanh(x_n/L_p) + \frac{e D_n n}{L_n}\tanh(x_p/L_n) \tag{8}$$

where it has also been assumed that $S_n = S_p = 0$. Since the tanh function is a decreasing function of its argument, it is seen that the diffusion current may be decreased by decreasing the ratios x_n/L_p and x_p/L_n. In fact, for small enough values of these ratios, $\tanh(x_n/L_p) \approx x_n/L_p$ and equation (8) becomes

$$J_{diff} = \frac{e p x_n}{\tau_p} + \frac{e n x_p}{\tau_n} \tag{9}$$

In the PV detector illustrated by Figure 2-1, the thickness of tne n-region x_n is necessarily small because the junction must be located near the incident surface. Thus, the first term in equation (9) will, by design, be small in relation to the second. The equation also predicts that a reduction in the thickness x_p of the p-type base region can significantly decrease the diffusion current. However, it must be remembered that this reduction in diffusion current is only obtained if the back surface recombination velocity can be made small enough. Detailed calculations using equation (6) and parameters appropriate for 10.6-μm PV HgCdTe detectors at 77°K have shown that, for $S_p > 10^5$ cm/sec, no decrease in J_{diff} is obtainable with a thin-base design. However, if $s_p < 10^3$ cm/sec, then a reduction in J_{diff} by about one order of magnitude appears feasible. During this program some investigations of a thin-base PV detector design were carried out to determine experimentally whether the predictions of equation (6) might be realized.

The generation-recombination current density has a thermal component which, near zero bias, can be represented by[6]

$$J_t = \frac{en_i W}{\sqrt{\tau_{no}\tau_{po}}}\left(\frac{2kT}{e\phi_b}\right), \qquad (10)$$

and a background photon component given by

$$J_b = \frac{e n_B W}{\sqrt{\tau_{no}\tau_{po}}}\left(\frac{2kT}{e\phi_b}\right) = (1 - r) Q_B e \alpha W \left(\frac{2kT}{e\phi_b}\right) \qquad (11)$$

where W = depletion layer width

τ_{no} = electron lifetime in depletion layer

τ_{po} = hole lifetime in depletion layer

ϕ_b = junction built-in voltage

r = front surface reflectance

α = absorption coefficient

Q_B = background photon flux density

n_B = background generated carrier concentration

---

[6] C. T. Sah, R. N. Noyce and W. Shockley, Proc. IRE 45, 1228 (1957).

The total g-r current is therefore

$$J_{gr} = J_t + J_b \tag{12}$$

Both J_{diff} and J_t are highly temperature dependent because the intrinsic carrier density n_i depends exponentially on T. Thus, J_{diff} goes as $\exp(-E_g/kT)$ and J_t goes as $\exp(-E_g/2kT)$ where E_g is the bandgap energy. Higher operating temperatures produce higher values of these current components and result in higher noise levels in the detector. At low temperatures, the saturation current density will be determined by J_b, provided that surface or bulk leakage current does not dominate.

Reverse Bias Operation

If the detector is operated at temperatures where thermally generated shot noise makes the dominant contribution to the noise current, then according to equation (3), the application of a reverse bias voltage $-V \gg \beta kT/e$ should make the exponential term much less than unity and this could conceivably result in a decrease in noise current by $\sqrt{2}$.

However, past experience has shown that the 1/f noise due to surface states may increase rapidly under reverse bias conditions. This depends on the surface passivation treatment used and the density and distribution of fast interface states at the semiconductor-insulator interface.

The possibility of noise reduction with reverse bias should be experimentally investigated. However, it cannot be counted on happening so the theoretical analysis of this section will not include this effect.

Resistance-Area Product

The resistance-area (R_0A) product of a PV detector is an important parameter because it sets the upper limit on achievable detectivity. To see how this comes about, consider again the noise equation (3). Photovoltaic detectors are usually operated at zero bias. This condition eliminates the exponential factor in the first term in equation (3) and minimizes the 1/f noise. Neglecting the 1/f noise term, the equation then simplifies to

$$\frac{i_n}{(\Delta f)^{\frac{1}{2}}} = \left\{\frac{4eI_s}{\beta} + \frac{4kT}{R_s} + 2eI_p\right\}^{\frac{1}{2}} \tag{13}$$

The first two terms involving the saturation current and the shunt resistance can be related to the zero bias dynamic resistance R_o of the photodiode by differentiating the diode equation

$$I = I_s\left[\exp\left(\frac{eV}{\beta kT}\right) - 1\right] - I_p + \frac{V}{R_s} \tag{14}$$

to get

$$R_o = \frac{dV}{dI}\bigg|_{V=0} = \left[\frac{eI_s}{\beta kT} + \frac{1}{R_s}\right]^{-1} \tag{15}$$

Combining equation (15) with (13) we can write the noise current per unit bandwidth as

$$\frac{i_n}{(\Delta f)^{\frac{1}{2}}} = \left[\frac{4kT}{R_o} + 2eI_p\right]^{\frac{1}{2}} \tag{16}$$

The background photon generated current from the base region is related to background photon flux density Q_B by

$$I_p = \eta e Q_B A \tag{17}$$

When equation (17) is substituted into (16) and the result substituted into equation (1), an expression for detectivity is obtained which is

$$D^*(\lambda) = \frac{\eta e\lambda}{hc}\left[\frac{A}{\frac{4kT}{R_o} + 2\eta e^2 Q_B A}\right]^{\frac{1}{2}} \tag{18}$$

Thus, at high background photon flux levels where the second term in the denominator dominates,

$$D^*(\lambda) = \frac{\eta\lambda}{hc}\left[\frac{1}{2\eta Q_B}\right]^{\frac{1}{2}} \tag{19}$$

which is the well-known expression for a BLIP photovoltaic detector. On the other hand, at low backgrounds or at higher operating temperatures, the first term in the denominator of equation (18) dominates and

$$D^*(\lambda) = \frac{\eta e \lambda}{hc}\left[\frac{R_0 A}{4kT}\right]^{\frac{1}{2}} \tag{20}$$

Therefore, $D^*(\lambda)$ depends on the R_0A product to the $\frac{1}{2}$ power and higher R_0A values permit higher $D^*(\lambda)$.

FREQUENCY RESPONSE

The frequency response of a photodiode will in general be limited by either:

1. Diffusion of carriers to the p-n junction
2. Drift across the junction or junction transit time (important for graded p-n junctions)
3. The diode junction capacitance

Diffusion Limited Frequency Response

Photogenerated minority carriers are generated near the surface of the device and must diffuse to the p-n junction before they can be "counted" in the photocurrent. This diffusion process requires a certain amount of time. The situation is shown schematically in Figure 2-2 for the case of an n-on-p junction with the junction located quite close to the top surface. In this case the diffusing minority carriers are electrons.

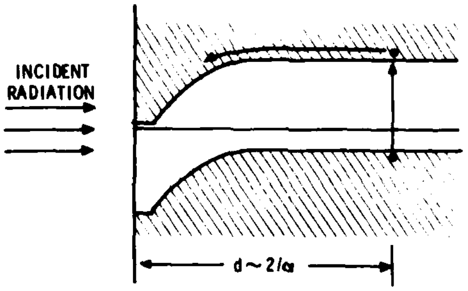

Figure 2-2. Diffusion Limited Photodiode

The frequency response for the diffusion limited photodiode has been treated by Sawyer and Rediker.[7] They found that the upper limit to the frequency response (0.707 point) is given approximately by

$$f_c = \frac{2.4\ D_n}{2\pi\ d^2} \tag{21}$$

where d is the distance from the point of origin of the minority carriers to the junction; and D_n is the diffusion coefficient,

$$D_n = \mu_n \frac{kT}{e} \tag{22}$$

Assuming $d = 2/\alpha \approx 4 \times 10^{-4}$ cm, $\mu_n = 1 \times 10^5$ cm^2/volt sec and $T = 77\,^\circ$K, we find that $D_n = 6.65 \times 10^2$ cm^2/sec, and $f_c = 1.6$ GHz. It seems clear from this calculation that the frequency response of the large area photodiodes will not be diffusion limited.

Drift Limited Frequency Response

This situation occurs when photogenerated carriers are produced within the depletion region of a p-n junction and are then swept out by the large electric field existing there. This type of junction is illustrated in Figure 2-3.

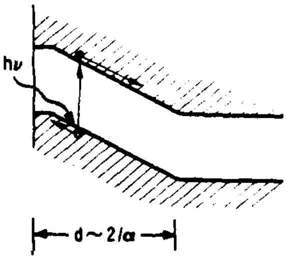

Figure 2-3. Drift Type Photodiode

Such a structure may be realized in p-i-n, or graded junction devices. This case has been analyzed by Gärtner,[8] who shows that the upper frequency limit (0.707 point) is

---

[7] D.E. Sawyer and R.H. Rediker, Proc. IRE 46, 1122 (1958).

[8] W.W. Gärtner, Phys. Rev. 116, 84 (1959).

$$f_c = \frac{2.8v}{2\pi W} \tag{23}$$

where v is the carrier velocity and W the width of the depletion region. Assuming $W = 2/\alpha$ and $v = 10^7$ cm/sec, then $f_c = 11$ GHz. Thus, the photodiode for the present application will not be drift limited.

Capacitance Limitations

In addition to the frequency response limitation imposed by drift or diffusion of carriers, we must also be concerned with the capacitance of the p-n junction. As shown in the equivalent circuit diagram of Figure 2-4, this capacitance acts as a shunt in parallel with the photodiode and will cause attenuation of the photocurrent at high frequencies.

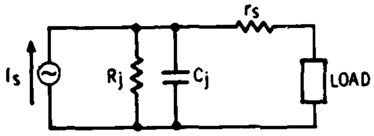

Figure 2-4. Equivalent Circuit for a Photodiode

The capacitance depends on the junction depletion layer width W, dielectric constant κ_s, and junction area A_j, as follows:

$$C_j = \kappa_s \epsilon_o \frac{A_j}{W} \tag{24}$$

where ϵ_o is the permittivity of empty space. To get a rough idea of the magnitude of capacitance that would be encountered, we consider the step junction situation in which the depletion layer width, W, is given by[9]

$$W = \left[\frac{2\kappa_s \epsilon_o}{eN} (\phi_b + V)\right]^{\frac{1}{2}} \tag{25}$$

where e is the electronic charge, N is the impurity concentration in the base region, ϕ_b is the built-in potential of the junction, and V is the externally applied potential.

---

[9] See, for example, A.S. Grove, "Physics and Technology of Semiconductor Devices," J. Wiley and Sons, New York, Chapter 6 (1967).

Using the following representative values for 0.1 eV HgCdTe

$\kappa_s = 18$

$\epsilon_o = 8.85 \times 10^{-14}$ fd/cm

$N = 10^{15}/\text{cm}^3$

$\phi_b = 0.05$ volt

$V = 0$ volt

we obtain a depletion layer width $W = 0.32 \times 10^{-4}$ cm. The junction capacitance for a 2× 2 mm² diode would then be $C_j = 2.0 \times 10^{-9}$ fd.

According to equation (25), application of an external reverse bias will increase the depletion width of the p-n junction and therefore decrease the junction capacitance. For example, a reverse bias of 0.5 volt will increase W to 1.0×10^{-4} cm and decrease C_j to 6.4×10^{-10} fd.

For this capacitance limited case, the high-frequency response limit (0.707 point) is given approximately by

$$f_c = \frac{1}{2\pi C_j R_{||}} \tag{26}$$

where C_j is the junction capacitance and $R_{||}$ is the parallel combination resistance of detector and load resistor. If we assume that $R_j >> R_L$, $C_j = 6.4 \times 10^{-10}$ fd, and $R_L = 50$ ohms, then $f_c = 5.0$ MHz.

It is clear from this example that the junction capacitance presents the major limitation to the high-frequency response of large area photodiodes. The frequency response can be improved somewhat by using a current-mode preamplifier. This type of amplifier presents an effective input impedance less than 50 ohms; therefore, the frequency response limit calculated from equation (26) will be greater than the value obtained above. A detailed discussion of detector operation when coupled to a current-mode preamplifier will be given subsequently.

It is theoretically possible to further reduce junction capacitance by constructing a linearly graded junction or a p-i-n structure. For the linearly graded junction, the depletion layer width is

$$W = \left[\frac{12\kappa_s\epsilon_o}{e\gamma}(\phi_b + V)\right]^{1/3} \qquad (27)$$

where all symbols have been previously defined, except γ which represents the impurity gradient at the junction. It is clear from this equation that, if γ can be kept small enough, the depletion layer width will be increased, thereby decreasing junction capacitance.

To increase the frequency response to much greater than 1 MHz, the capacitance of the junction must be considerably less than 10^{-9} fd. The depletion layer width required is then

$$W > 3.1 \times 10^{-4} \text{ cm}$$

This would require the gradient, γ, to be

$$\gamma \sim 1 \times 10^{18} \text{ cm}^{-4}$$

Such a gradient could only be achieved in very pure material. It implies a change in doping concentration of $10^{14}/\text{cm}^3/\mu\text{m}$ of distance into the crystal. The base doping of the crystal would therefore have to be much less than $10^{14}/\text{cm}^3$. Although such material has been seen, it occurs only rarely in fortuitously compensated ingots.

Likewise, a p-i-n structure would require some way to obtain material with impurity concentration in the i region much less than $10^{14}/\text{cm}^3$. Since there seemed to be small likelihood of obtaining such material in large enough quantity to make the large area detectors required for this program, these approaches were not pursued. A step junction approach was selected and the base doping was minimized to keep the junction capacitance as low as possible.

DETECTOR-PREAMPLIFIER ANALYSIS

For high frequency applications, a current-mode preamplifier is desired to reduce the capacitive loading due to the high junction capacitance of the PV detector. Preamplifier noise may be the limiting noise at high frequencies. Therefore, an analysis of detector frequency response and sensitivity must also include the preamplifier. In this section, such an analysis is performed.

Signal Response

Figure 2-5 shows the equivalent circuit for the PV detector-preamplifier combination. Consider first the signal current produced by the ideal current generator i_s. If detector series resistance is not negligible, the signal current reaching the preamplifier input will be given by

$$i_i = i_s \left(\frac{Z_j}{Z_j + r_s} \right) \qquad (28)$$

where the junction impedance Z_j is given by

$$Z_j = R_j \, (1 + \omega^2 R_j^2 C_j^2)^{-\frac{1}{2}} \qquad (29)$$

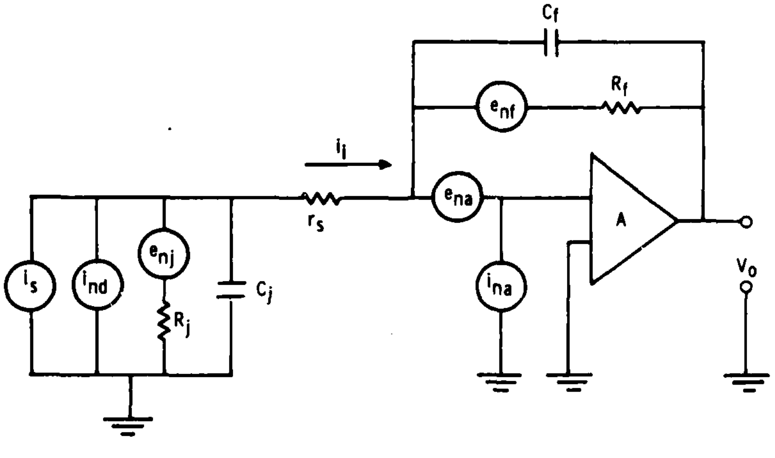

Figure 2-5. Equivalent Circuit Diagram for the PV Detector-Preamplifier Combination

At high frequencies, the capacitive reactance may dominate, thus

$$Z_j \approx \frac{1}{\omega C_j} \tag{30}$$

Consider a case where the junction capacitance is 4000 pf. Then, at a frequency of 1 MHz, Z_j = 40 ohms and the series resistance must be much less than this value to avoid loss of signal current.

The output signal voltage from the preamplifier is given by

$$V_{os} = \frac{-AZ_f i_s}{A + 1 + \left(\frac{Z_f}{Z_j + r_s}\right)} \left(\frac{Z_j}{Z_j + r_s}\right) \tag{31}$$

where the feedback impedance Z_f is

$$Z_f = R_f \left(1 + \omega^2 R_f^2 C_f^2\right)^{-\frac{1}{2}} \tag{32}$$

and A is the amplifier open loop gain. For low frequencies, where $Z_f \approx Z_j$, $r_s << Z_j$ and $A >> 1$, equation (31) reduces to

$$V_{os} \approx -R_f i_s \tag{33}$$

The high frequency response is reduced to 1/2 the low frequency value at some frequency given by

$$f_h \approx \left[2\pi \left(\frac{R_f}{1 + A}\right) C_j\right]^{-1} \tag{34}$$

The factor $R_f/(1 + A)$ is the "equivalent" input impedance of the current-mode preamplifier. It turns out that a practical value for A is about 50 and for R_f about 1000 ohms. Therefore, the junction capacitance C_j must be minimized to allow high frequency response. If C_j = 4000 pf, and the above values for A and R_f are used, then f_h = 2 MHz.

Noise

The major noise sources are shown in the equivalent circuit diagram of Figure 2-5. They are: amplifier voltage and current noise, feedback resistor Johnson noise, detector Johnson noise, and detector photon generated shot noise. These combine to give a total noise voltage per unit of frequency bandwidth at the preamplifier output which can be expressed by the equation

$$\frac{V_{on}}{\sqrt{\Delta f}} = \left[\left(1 + \frac{Z_f}{Z_j}\right)^2 \left(e_{na}^2 + i_{na}^2 Z_f^2\right) + \left(\frac{4kT_f}{R_f}\right) Z_f^2 + \left(\frac{4kT_j}{R_j}\right) Z_f^2 + 2e^2 \eta Q_B A_d Z_f^2\right]^{\frac{1}{2}} \qquad (35)$$

The four terms in this equation represent the noise sources in the order listed above.

The preamplifier current noise can be neglected at high frequencies. With this approximation and some algebraic manipulations of equation (35), one can obtain

$$\frac{V_{on}}{\sqrt{\Delta f}} = \left\{\left|\left(\frac{1}{R_f} + \frac{1}{R_j}\right) + j\omega(C_f + C_j)\right|^2 e_{na}^2 + \frac{4kT_f}{R_f} + \frac{4kT_j}{R_j} + 2e^2 \eta Q_B A\right\}^{\frac{1}{2}} Z_f \qquad (36)$$

This equation shows that the preamplifier voltage noise is boosted at higher frequencies while the other noise terms remain flat. The degree of high frequency boost is dependent on the magnitude of detector junction capacitance. Thus a minimized junction capacitance is necessary not only for extending the signal response to high frequency but also for minimizing noise at high frequency.

The corner frequency at which preamplifier noise boost commences is obtained by setting

$$\left(\frac{1}{R_f} + \frac{1}{R_j}\right) = 2\pi f(C_f + C_j)$$

and solving for f. This yields

$$f = \frac{1}{2\pi(C_f + C_j)}\left(\frac{1}{R_f} + \frac{1}{R_j}\right) \qquad (37)$$

For a case where $R_f = R_j = 1000$ ohms, $C_j = 4000$ pf and C_f is negligible, one obtains $f = 8 \times 10^4$ Hz. The noise boost cannot continue indefinitely but will ultimately be rolled off at higher frequencies due to frequency limitations inherent in the transistors used or to high frequency rolloff purposely built into the preamplifier for stability reasons.

D* versus Frequency

Using equation (31) to calculate responsivity and equation (36) to calculate noise, D* may then be obtained as a function of frequency from the usual equation

$$D^*(\lambda_p, f) = \frac{R_v(\lambda_p, f)\sqrt{A_d}}{V_{on}(f)/\sqrt{\Delta f}} \tag{38}$$

A parametric study was made to ascertain the effect on $D^*(\lambda_p, f)$ produced by variations in the detector parameters, R_j, C_j, and r_s. Values for D* versus frequency were calculated holding two parameters fixed, and allowing the third to vary. Figures 2-6, 2-7, and 2-8 show the results of this study. Other fixed parameters used in the calculations were as follows.

R_f = 1000 ohms
A = 50
T_f = 295°K
T_d = 77°K
e_{na} = 0.7 nv/Hz$^{\frac{1}{2}}$
A_d = 0.284 cm^2
η = 0.84
Q_B = 2×10^{15} photons/sec/cm^2
$I_s(\lambda_p)$ = 2.5 amps/watt
λ_p = 3.85 μm

Figure 2-6 shows that little effect on D* is produced by variations in R_j. This is as expected since the junction impedance at high frequencies is controlled by the capacitive reactance, not by the junction resistance. Figure 2-7 shows that series resistance up to 10 ohms does not cause serious degradation of high frequency D*. Figure 2-8 shows that junction capacitance has the strongest effect on high frequency D*.

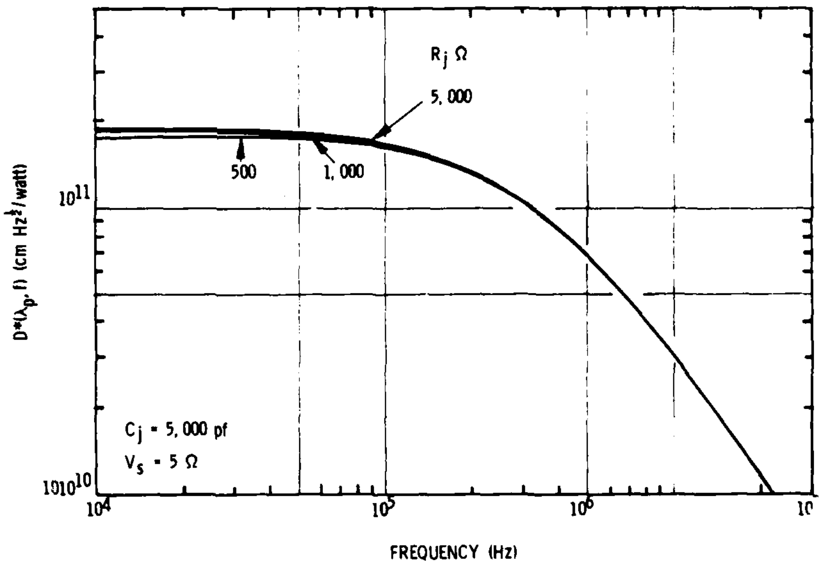

Figure 2-6. High Frequency D* Dependence on Junction Resistance

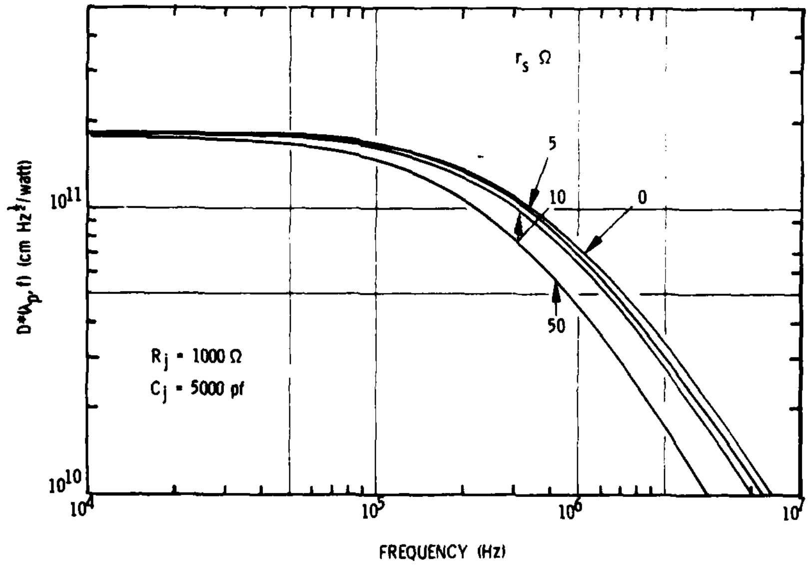

Figure 2-7. High Frequency D* Dependence on Series Resistance

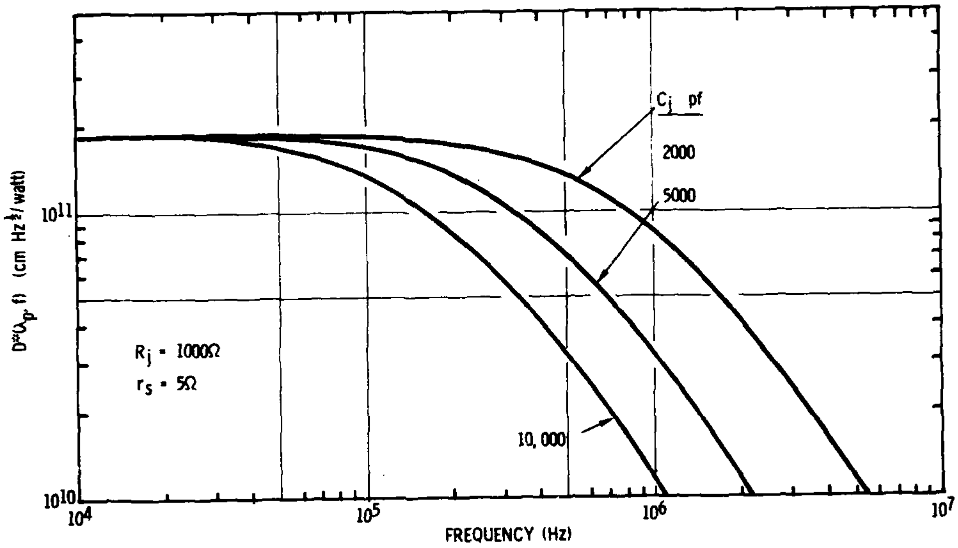

Figure 2-8. High Frequency D* Dependence on Junction Capacitance

Section 3

HgCdTe MATERIAL PREPARATION

Because of its versatility, HgCdTe is one of the most popular infrared detector materials presently in use. Of all the variable bandgap ternary alloy systems, it alone provides the widest span of detection wavelengths, from 0.9 μm (pure CdTe) to beyond 30 μm (16% CdTe/84% HgTe). However, it is also one of the most difficult to prepare in single-crystal form because of the high vapor pressure of Hg encountered at the melting temperature. In this section are presented some of the basic physical and thermodynamic properties of the HgCdTe alloy system, the crystal growth methods adopted by SBRC for this program, and typical results of the crystal growing study.

PHYSICAL AND THERMODYNAMIC PROPERTIES

HgCdTe is a variable bandgap alloy semiconductor made by combining CdTe (a wide-bandgap semiconductor) and HgTe (a semimetal). HgCdTe photodetectors have been made over the 1- to 30-μm spectral region by varying the composition of the alloy (Figure 3-1).

The dependence of the energy gap of $Hg_{1-x}Cd_xTe$ alloys on composition x and absolute temperature T is given by[10]

$$E_g = -0.25 + 1.59x + 5.233 \times 10^{-4} (1 - 2.08x) T + 0.327x^3 \qquad (39)$$

Solution of this equation for 2.06-, 3.85-, and 10.6-μm peak wavelengths and operating temperatures of 245°K, 195°K, and 77°K gives approximate values for x of 0.48, 0.31, and 0.21, respectively. This calculation assumes energy bandgap values of 0.55, 0.29, and 0.11 eV corresponding to detector cutoff wavelengths of 2.27, 4.24, and 11.3 μm, respectively.

---

[10] J. L. Schmit and E. L. Stelzer, J. Appl. Phys. 40, 4865 (1969).

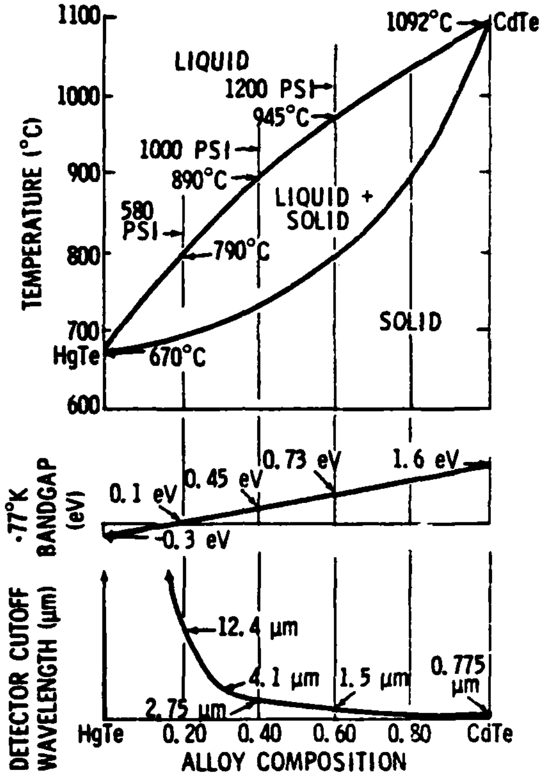

Figure 3-1. Physical and Thermodynamic Properties of HgCdTe Alloys

To understand the difficulties of crystal growth of HgCdTe material, and the specific techniques that have been developed to overcome them, it is useful to consider the thermodynamic properties and phase diagram of the Hg-Cd-Te system.

Figure 3-1 illustrates the pseudobinary HgTe-CdTe temperature-composition phase diagram. This diagram shows the wide separation between liquidus and solidus curves, which results from the significant difference in the melting points of the end compounds, and their large heats of fusion.[11] This leads to the well-known segregation of the alloy upon freezing from the melt, and therefore to nonuniformity of material composition.

---

[11] J. Steininger, J. Appl. Phys. 41, 2713 (1970).

Another less-known segregation effect results from the difference in the density of alloys of different compositions. The alloy density ρ for a composition x is given by

$$\rho\ (\mathrm{gm/cm^3}) = 8.076 - 2.226x \tag{40}$$

The CdTe-rich solid material which freezes out first is much lighter than the HgTe-rich melt, and therefore tends to float to the surface of the melt giving rise to vertical segregation in the ingot.

Figure 3-2 illustrates the pressure-temperature phase diagram for various sections of the Hg-Cd-Te system. Shown here is recent data[12] on

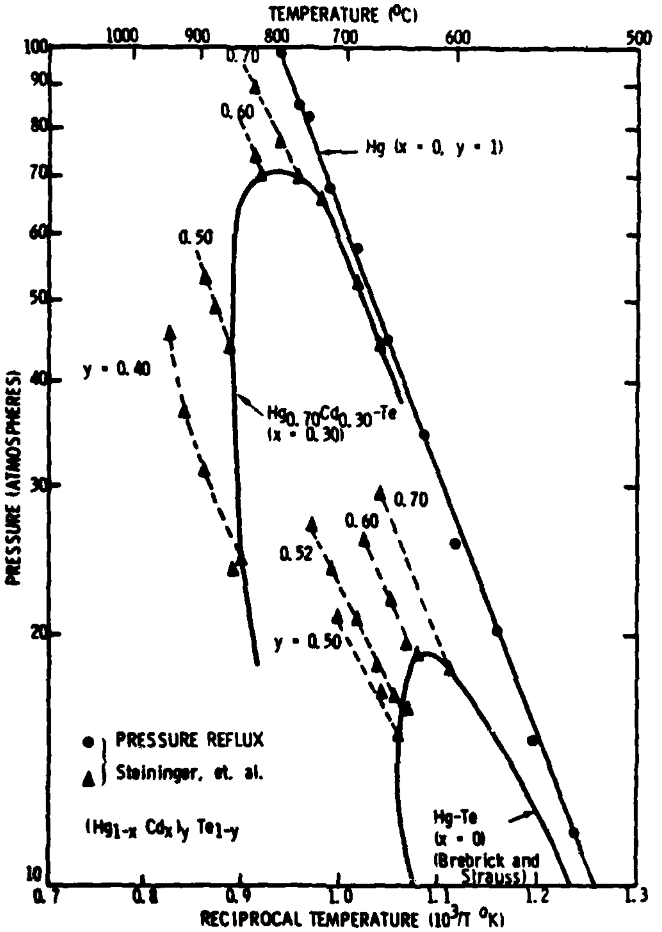

Figure 3-2. Hg-Cd-Te Pressure-Temperature Phase Diagram

---

[12] J. Steininger, J. Electronic Materials 5, 299 (1976).

the variation of Hg vapor pressure over liquid melts of pure Hg, binary Hg-Te and ternary $Hg_{0.70}Cd_{0.30}Te$. The alloy compositions are represented by the formula $(Hg_{1-x}Cd_x)_yTe_{1-y}$, where x is the usual pseudobinary alloy composition, and y represents the deviations from pseudobinary stoichiometry (y = 0.50); i.e., excess metal (y > 0.50) or excess Te (y < 0.50). The significant feature of these data, from the point of view of crystal growth, is the rapid variation of the Hg vapor pressure over the melt with composition, and particularly near the stoichiometric compositions. The variation of vapor pressure of pure Hg, P_{Hg}, is given by

$$\ell n \, P_{Hg}(atm) = 11.238 - 7,100/T \; (^\circ K) \qquad (41)$$

For stoichiometric melts, the variation of vapor pressure, P_{HCT}, is given by

$$\ell n \, P_{HCT}(atm) = 10.206 - 7,149/T \; (^\circ K) \qquad (42)$$

This expression is valid for $0 \leq x \leq 0.60$ and for $670 \leq t \leq 965^\circ C$. This points out the requirement for good control of the Hg overpressure to maintain stoichiometry in the melt, and therefore uniform solidification. If the Hg vapor pressure is too high, this results in Hg inclusions and blowholes. If it is too low, it leads to partial decomposition and Te inclusions. In both cases, this will also lead to variations in the alloy composition, x. This effect is a significant but often overlooked cause of nonuniformity in HgCdTe material and detectors.

Figure 3-3 shows the actual temperature and pressure parameters for alloy compositions corresponding to 2.06-, 3.85-, and 10.6-μm detectors. The liquidus temperatures of 920°C, 845°C, and 800°C correspond to vapor pressures of 67 atm (980 psi), 45 atm (655 psi), and 35 atm (510 psi) for stoichiometric melts. At the same temperatures, free Hg has pressures in excess of 200 atm (3,000 psi), 140 atm (2,100 psi), and 102 atm (1,490 psi), respectively. These should be considered minimum values since in crystal growth from the melt, the charge has to be superheated by 20°C to 25°C to ensure complete dissolution and homogenization.

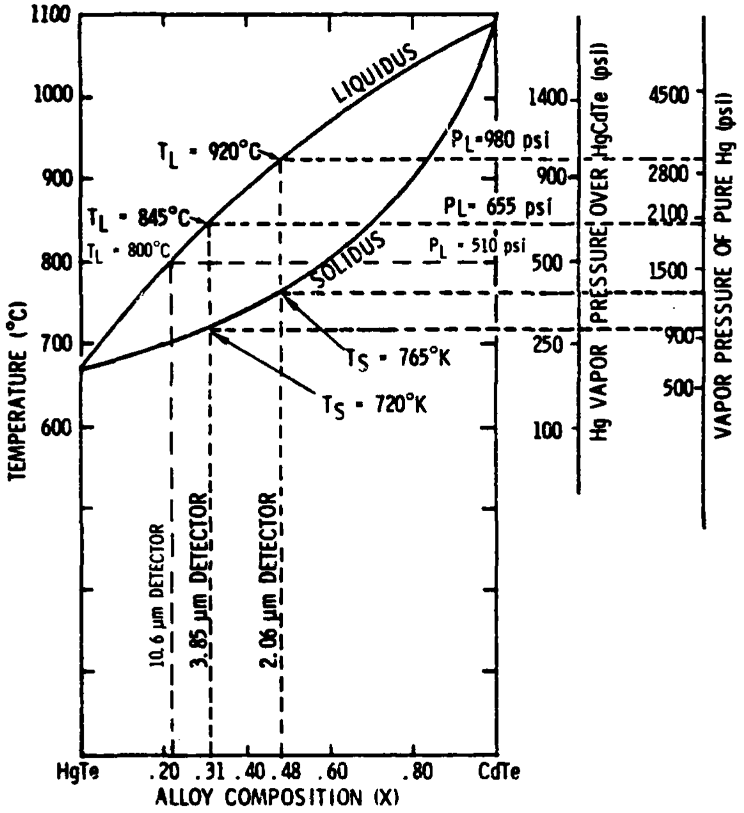

Figure 3-3. Thermodynamic Properties of HgCdTe Alloys for 2.06, 3.85, and 10.6 µm

CRYSTAL GROWTH METHODS

The preceding discussion of the thermodynamic properties of HgCdTe alloys points up the significant factors and main difficulties to be considered in the growth of high quality material. These can be summarized as follows:

1. The high Hg vapor pressure over the melt makes it difficult to contain the charge (explosion of quartz ampoules), and to control its stoichiometry.
2. Alloy segregation upon freezing can lead to severe lack of uniformity in the material.
3. Additional segregation results from density differentials.

All these problems which are already severe for long-wavelength 8- to 14-µm material (x = 0.20) are significantly increased for shorter wavelength material due to the much higher vapor pressures that have to be contended with.

Based on past experience with a variety of HgCdTe crystal growth methods, it was decided to adopt two different growth methods for this program. These were solid-state recrystallization (SSR) and zone melting (ZM).

Solid-State Recrystallization

The solid-state recrystallization technique uses a fast quench to minimize alloy segregation. The dendritic, polycrystalline material is then recrystallized by high-temperature annealing. Figure 3-4a illustrates this method. The macroscopic uniformity may sometimes be poorer because of trapped inclusions of excess Hg or Te at grain boundaries. Also, impurities in the melt during quench are frozen into the ingot and remain there.

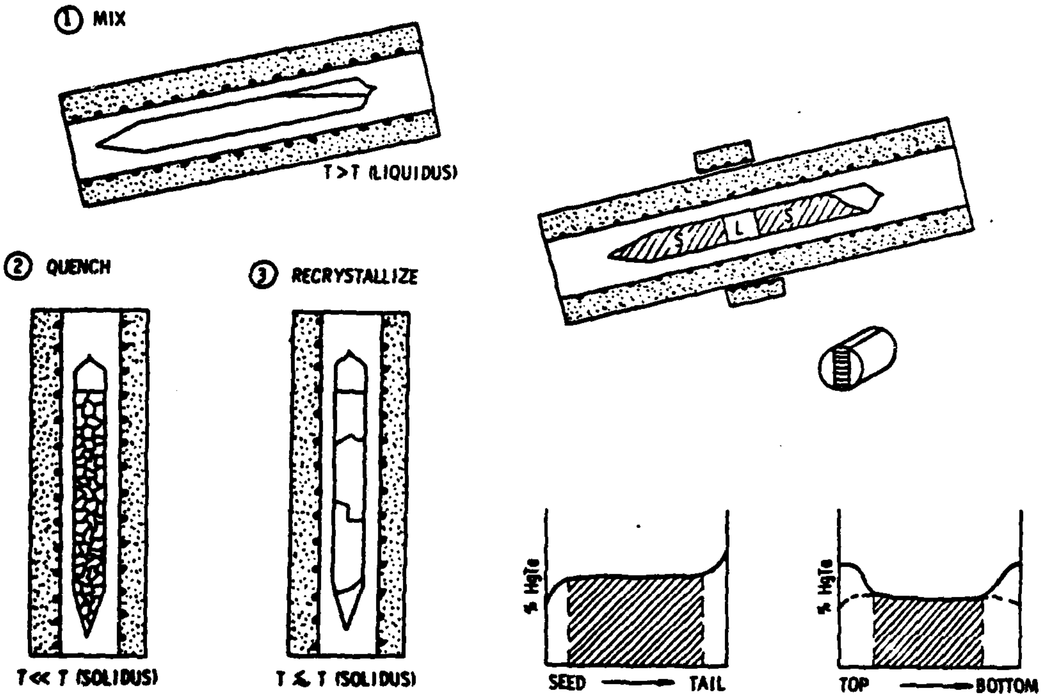

(a) Solid State Recrystallization Method (b) Zone Melting Method

Figure 3-4. HgCdTe Crystal Growth Techniques in Sealed Quartz Ampoule

Zone Melting Technique

A more sophisticated technique previously developed at SBRC on IR&D funding is zone melting in a closed tube (Figure 3-4b). In this process, the charge is first reacted and quenched in a rocking furnace. It is then placed in a zone melting furnace for crystal growth. This is achieved by passing a molten zone through the charge at a slow rate to assure crystal perfection. A pointed tip is made at one end of the quartz ampoule to promote single-crystal growth. Either a vertical or horizontal zone melting furnace may be employed.

Normal segregation produces compositional nonuniformity at the seed and tail ends of the ingot. There may also be a radial composition variation as shown in the diagram in Figure 3-4b. This is dependent on zone size, the shape of the liquid-solid interface, and the furnace temperature gradients. By empirical methods, it has been possible to minimize the radial nonuniformity to the extent shown by the dashed lines in the figure. This provides an adequate supply of uniform material in the central core of the ingot. An additional advantage to the ZM method is the reduction in impurity content by the zone refining action provided as the molten zone is moved down the ingot.

Another advantage of the zone melting technique for the preparation of HgCdTe material arises because crystal growth takes place at the much lower solidus temperature T_s (Figure 3-3). Consequently, the pressure during crystal growth remains below 30 atm (450 psi) if the melt is stoichiometric. The critical step, however, is compounding and quenching of the charge, which still requires temperatures above the liquidus with a resultant high Hg vapor pressure.

MATERIAL SELECTION AND EVALUATION

Wafers of HgCdTe were chosen from stock ingots grown by both SSR and ZM methods. The first evaluation of a wafer consists of a visual inspection to check for grain boundaries. Since a grain bondary may provide a location for various impurity atoms or crystal defects, it is not desirable to fabricate a PV detector on a grain boundary. This would most likely short out the p-n junction. Most of the HgCdTe ingots produced have single-crystal regions varying in size from about 1 cm^3 up to several cm^3. The ingots are typically 1.2 cm in diameter and 15 to 20 cm in length as shown in Figure 3-5. Therefore, selection of wafers with very few or no grain boundaries is a simple procedure, and a high yield of useful material is obtained from each ingot.

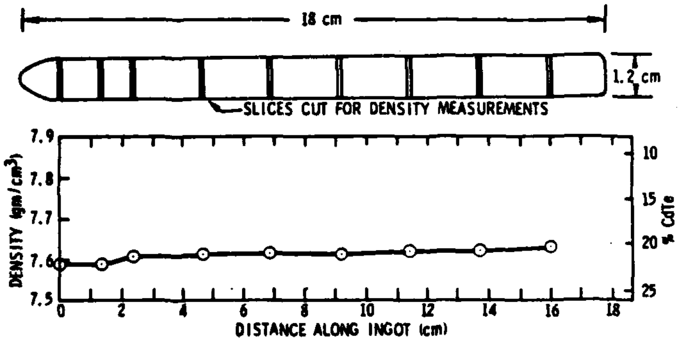

a) Ingot No. V12, Grown by the ZM Method

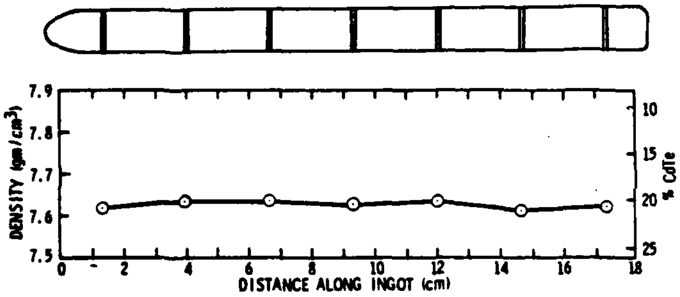

b) Ingot No. EYS7, Grown by the SSR Method

Figure 3-5. Density Profiles of Typical HgCdTe Ingots Produced by ZM and SSR Methods

Density measurements are made on selected wafers from each ingot to provide a rough check of the compositional uniformity of the ingot. The density is determined by a simple hydrostatic weighing method. The measured density can then be related to compositional x-value by use of equation (40). Figure 3-5 illustrates the resulting data obtained on one typical SSR ingot and one ZM ingot. The estimated error in the density value is ±0.01 gm/cm^3

and this is represented by the diameter of the data point circles on the figure. According to equation (40), a variation in density of 0.02 gm/cm^3 implies a variation in x-value of 0.01. For 10.6-μm $Hg_{1-x}Cd_xTe$ material, this results in a variation in cutoff wavelength of about 1.5 μm. Thus, the density measurement does not give a high precision determination of the cutoff wavelength. Furthermore, a density measurement on a given wafer determines the average density of that wafer and says nothing about variations within the wafer. More precise determinations of variations in alloy composition are indicated by detector cutoff wavelength measured after fabrication of multielement arrays.

X-ray topographic techniques were employed to evaluate the crystallographic lattice perfection of the HgCdTe material. Figure 3-6 illustrates the Berg-Barrett back-reflection technique which was utilized.[13] A polished

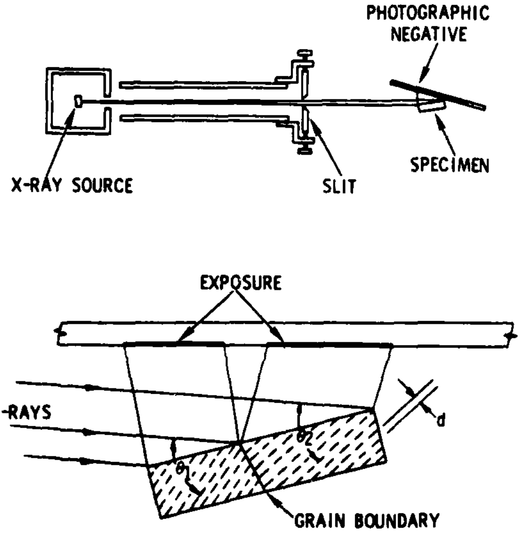

$n\lambda = 2d \sin\theta$

λ = X-RAY WAVELENGTH

n = INTEGER

d = DISTANCE BETWEEN PLANES

$\theta_1 \neq \theta_2$ FOR BICRYSTAL

Figure 3-6. Berg-Barrett Back-Reflection Topography Method

---

[13] X-ray topographic services were provided by Technology of Materials, Inc. of Santa Barbara, California.

HgCdTe wafer is placed in a well-collimated X-ray beam, and a high-resolution photographic plate is placed in close proximity to the wafer where it may be exposed by X-rays reflected from the HgCdTe. Crystallites in the HgCdTe wafer having different crystallographic orientations reflect the X-rays at different Bragg angles according to the relation

$$n\lambda = 2d \sin \theta \tag{43}$$

where λ is the X-ray wavelength, n is an integral number, d is the spacing between lattice planes and θ is the Bragg angle. A region in the crystal where the lattice angle changes with respect to the X-ray beam will produce a shifted image on the film plate. This technique is capable of determining misorientation to within a few tens of seconds of arc. Other lattice imperfections such as pits, inclusions, or scratches may also be observed.

Figure 3-7 shows an X-ray topograph of a wafer from ingot EYS17 which was grown by the SSR method. Most of this wafer was single crystal of high quality. Two images are seen due to reflections from two different sets of lattice planes. The image of one edge of the wafer is shifted by a large amount because this part of the wafer was a grain with different

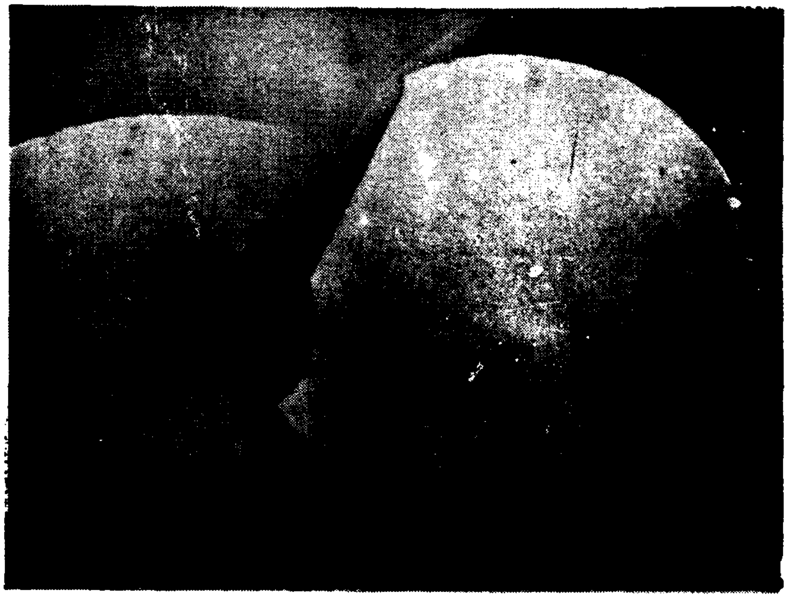

Figure 3-7. X-Ray Topograph of Wafer No. EYS17-16

orientation from the rest. Also seen on the topograph are some pits and scratches. The pits are due to excess Hg in the crystal during growth. They are confined to the edge of the wafer and do not normally present a problem for detector fabrication. The scratches are due to handling with tweezers and are not intrinsic lattice defects.

Figure 3-8 shows the topograph of a wafer from ingot V8 grown by the ZM method. Again, most of this wafer is single crystal. The jagged edge denotes a grain boundary, and the images of the neighboring crystal grains are, for the most part, off the negative. A more striking thing about this picture is the extensive network of low-angle tilt boundaries throughout this wafer. This result has been found to be typical of all HgCdTe material grown by the ZM method. Chemical etching studies have shown a high concentration of edge dislocation etch pits running along these tilt boundaries. This is sometimes referred to as lineage. This is thought to be due to the fact that ZM crystals are grown in a sealed quartz capsule. If the HgCdTe expands slightly during freezing, then it will be subjected to a compressive stress,

Figure 3-8. X-Ray Topograph of Wafer No. V8-79

which could result in a slight "buckling" of the crystal lattice. SSR crystals are not closely confined during growth and, therefore, do not exhibit this type of lattice defect. Since good large area photodiodes were made from the ZM material, it appears that the low-angle tilt boundaries do not significantly degrade the p-n junction.

Annealing

HgCdTe crystals as grown usually contain on the order of 10^{17} to 10^{18}/cm^3 Hg vacancies. Since these vacancies produce acceptor centers in the crystal, the material is highly p-type. To obtain the low acceptor concentration material necessary for low-capacitance p-n junctions, the number of vacancies must be reduced. This is easily accomplished by heating the material to temperatures on the order of 300°C in the presence of Hg vapor.[14, 15] A sufficient time must be allotted so that Hg atoms from the vapor phase can diffuse into the HgCdTe and fill the vacancies. A judicious choice of annealing temperature and Hg vapor pressure can leave the material with the desired density of Hg vacancies, and therefore provide p-type material with the desired low acceptor concentration.

On the other hand, it is also possible to dope the crystals with certain impurity atoms which produce acceptor centers. In previous work, SBRC has utilized Au atoms for acceptor doping of HgCdTe. Au has a high enough diffusion coefficient so that it can be introduced into the HgCdTe by solid-state diffusion.[16] Alternatively, it can be introduced from the melt during crystal growth. Most of the p-type material produced for this program was Au-doped by diffusion. The Au diffusion was done in the presence of Hg vapor so as to fill Hg vacancies at the same time the diffusion process was taking place.

---

[14] R. A. Reynolds, M. J. Brau, H. Kraus, and R. T. Bate, "Proc. of Conf. on Narrow Gap Semiconductors," Dallas (1970), Ed. by Carter and Bate, Pergamon Press, New York, p. 511 (1971).

[15] B. E. Bartlett, J. Deans and P. C. Ellen, J. Materials Science 4, 266 (1969).

[16] A. I. Andrievskii, A. S. Teodorovich, and A. D. Schneider, Sov. Phys., Semicond. 7, 1112 (1974).

Hall Effect Measurements

After annealing, the electrical properties of the HgCdTe material were determined by Hall effect measurements. These measurements give the net acceptor doping concentration, the hole mobility, and the resistivity. Figure 3-9 shows Hall coefficient data versus reciprocal temperature acquired on three Au-doped samples of $Hg_{0.79}Cd_{0.21}Te$. In the extrinsic temperature range (i.e., below 77°K), the Hall coefficient R_H is related to free hole concentration p by the expression

$$R_H = \frac{1}{ep} \tag{44}$$

At high temperatures (about 77°K) all Au acceptors are ionized and the hole concentration is given by

$$p = N_{Au} - N_D \tag{45}$$

where N_{Au} is the Au atom concentration and N_D is the residual donor impurity concentration. For N_D small compared to N_{Au}, then $p \approx N_{Au}$ and the Au concentration can be obtained from the measured Hall coefficient. Au concentrations calculated in this way are indicated in Figure 3-9 for the three samples.

At low temperatures, holes "freeze out" on the Au acceptor atoms and the equilibrium free-hole concentration decreases, thereby causing the measured Hall coefficient to increase. From the slope of the R_H versus 1/T curve in this "freeze-out" region, the activation energy for the Au acceptor site is obtained. A typical value is 0.01 eV. Some R_H versus 1/T curves, such as the one for sample V8-28, do not show the proper slope in the low temperature range and this is thought to be due to the effect of surface contamination on the sample. The very lightly doped p-type samples are much more susceptible to such surface effects than the heavily doped samples. At temperatures above 77°K, thermal generation of intrinsic electrons and holes becomes significant. The electrons, because of their much larger mobility, begin to dominate the Hall effect measurement and cause the sign of the Hall coefficient to change from positive to negative.

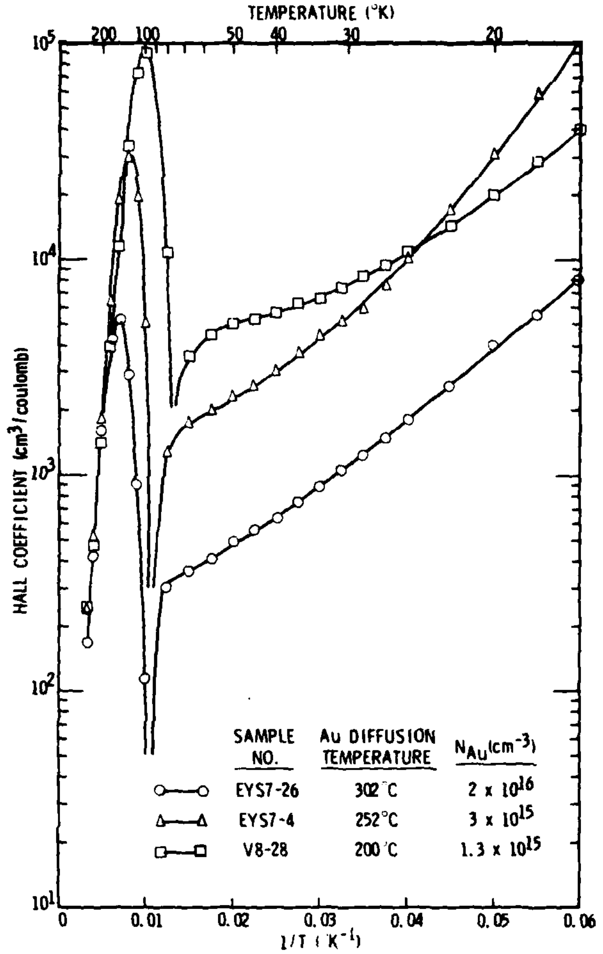

Figure 3-9. Hall Coefficient versus 1/T for Three Representative Au-Doped $Hg_{0.79}Cd_{0.21}Te$ Samples

Figure 3-10 shows measured resistivity versus reciprocal temperature curves for the same three Au-doped samples. The Hall mobility is found from the ratio of the Hall coefficient to resistivity. These values are plotted in Figure 3-11. All three samples have nearly the same mobility values over the temperature range from 77°K to 16°K.

Photodiode Fabrication

After evaluation of selected wafers from the various ingots by the methods discussed, other wafers were selected for photodiode fabrication. Selections were made from seven different SSR ingots and nine different ZM ingots during the course of this work on 10.6-μm quadrant arrays. These wafers

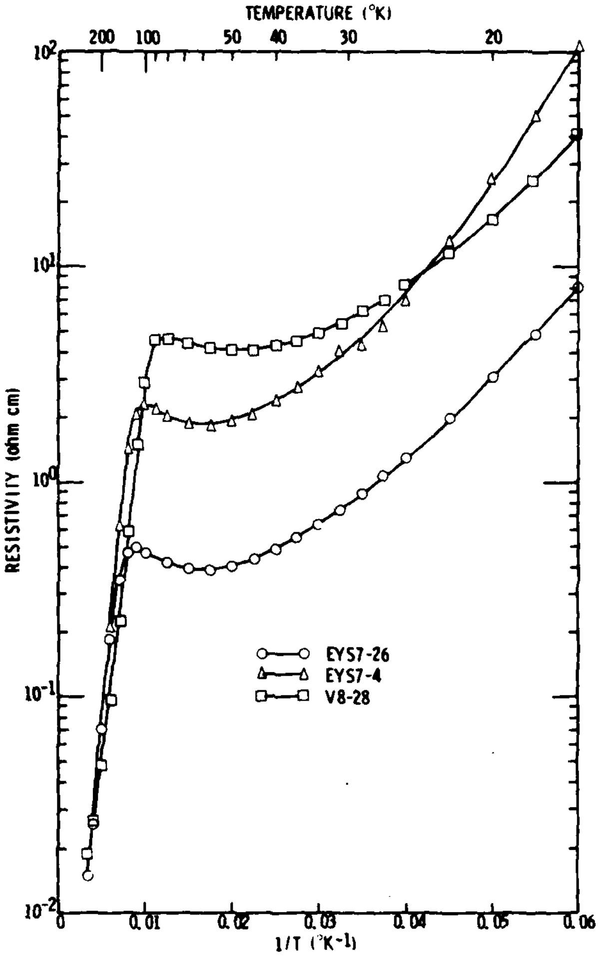

Figure 3-10. Resistivity versus 1/T for Three Representative Au-Doped $Hg_{0.79}Cd_{0.21}Te$ Samples

were usually inspected visually to establish freedom from pits or inclusions and grain boundaries.

Each wafer was polished on one side by a chemical-mechanical polishing process. A final cleanup etch in Br_2:methanol solution is done prior to p-n junction formation. The p-n junction formation techniques employed are described in the next section.

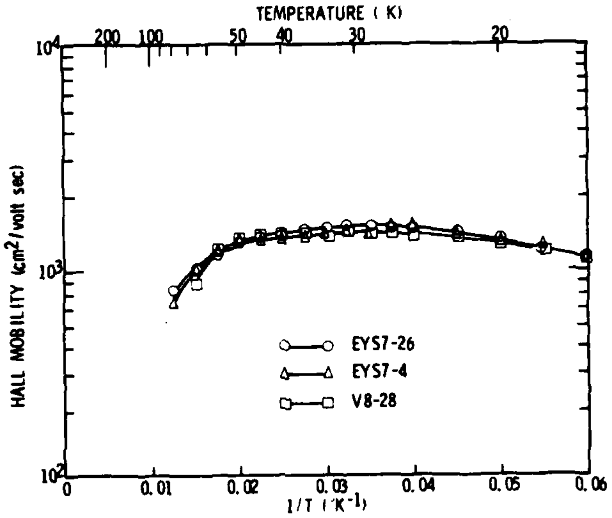

Figure 3-11. Hall Mobility versus 1/T for Three Representative $Hg_{0.79}Cd_{0.21}Te$ Samples

Section 4

PHOTODIODE FABRICATION

JUNCTION FORMATION

The primary method selected for junction formation in the large area PV HgCdTe detectors was ion implantation. This produced an n-on-p structure where the n-layer was formed by ion implantation into p-type base material. The primary reason for selection of this method was its capability for producing uniform doping concentrations at a precisely controlled depth in the material. Other workers have reported p-n junction formation in HgCdTe using Al,[17] Hg,[18] In,[19] and H^{20} ions. Previous work on this program[21] showed that uniform p-n junctions up to 5 × 5 mm^2 in area could be obtained for 2.06-μm and 3.85-μm detectors by utilization of B ion implants. Therefore, we sought to develop the same technique for 10.6-μm detectors.

During the initial investigations of B ion implanted 10.6-μm diodes, it was found that the ion dose had to be significantly altered from that used on short-wavelength diodes. While ion doses that produced donor doping concentrations on the order of $10^{18}/cm^3$ were suitable for junctions in short-wavelength material, such doses were found to result in high tunneling leakage current when used for long-wavelength junctions. The reason for this is illustrated in Figure 4-1. Because the conduction band density of states is low in HgCdTe, the Fermi level for $10^{18}/cm^3$ n-type material will lie high up in the conduction band as shown in part (a) of the figure. This allows direct

---

[17] J. Marine and C. Motte, Appl. Phys. Lett. 23, 450 (1973).

[18] G. Fiorito, G. Gasparrini and F. Svelto, Appl. Phys. Lett. 23, 448 (1973).

[19] Unpublished reports from Honeywell Radiation Center and Arthur D. Little Corp.

[20] A. G. Foyt, T. C. Harman and J. P. Donnelly, Appl. Phys. Lett. 18, 321 (1971).

[21] See reference No. 1.

(a) High n-Side Doping $\approx 10^{18}/\text{cm}^3$

(b) Low n-Side Doping $\approx 10^{16}$ cm^3

p-Side Doping $\approx 10^{15}/\text{cm}^3$ for Both Cases

Figure 4-1. Energy Band Diagrams for 10.6-µm HgCdTe p-n Junctions at 77°K

band-to-band tunneling of electrons from the conduction band into empty states in the valence band (holes). Such junctions exhibit ohmic current-voltage characteristics and no PV effect. The lower barrier height and width in 10.6-µm material are also conducive to high tunnel current relative to the 2.06-µm and 3.85-µm materials.

To minimize tunnel current, donor concentrations on the n-side must be kept below $10^{16}/\text{cm}^3$. Under this condition, the band diagram is that of Figure 4-1(b) and direct band-to-band tunneling is prohibited, excepting perhaps under reverse bias conditions. The best junctions made on this program were achieved with n-type implant doping levels between 5×10^{15} and $1 \times 10^{16}/\text{cm}^3$.

The initial investigation also showed that a second ion-implant dose was required to lower the sheet resistance of the n-layer so as to provide a more uniform photoresponse over the sensitive area. This second implant was done with a high dose at lower implant energy. The resultant structure was therefore an n^+-n-p structure as shown in Figure 4-2(a). Also shown in part (b) of this figure is the relative generation rate of photo-excited free carriers plotted versus depth into the HgCdTe material. This is given by the expression

$$g = I_o(1 - r)\alpha \exp(-\alpha x) \quad (46)$$

where I_o is the incident radiant intensity, r the front surface reflectivity, α the absorption coefficient, and x is distance. A value for α of 5×10^3/cm was chosen for the curve plotted in Figure 4-2(b). It is seen from these data that about 90% of the radiation penetrating the front surface is absorbed in the first 4 μm of material. Free carriers produced within a diffusion length of the junction have a high probability of being collected and therefore contributing to the photocurrent. The diffusion length L is given by

$$L = \sqrt{D\tau} = \left[\frac{\mu kT}{e}\tau\right]^{\frac{1}{2}} \tag{47}$$

where D is the carrier diffusion coefficient, τ its lifetime, k is Boltzmann's constant, T the absolute temperature, and e the electronic charge. Since it is the minority carrier which is being collected, the diffusion length is either that of a hole on the n-side of the junction or that of an electron on the p-side.

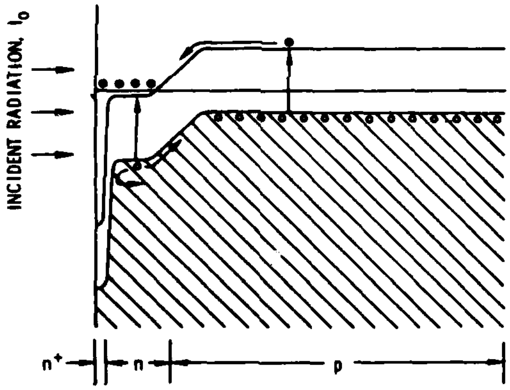

(a) Energy Band Diagram for n^+-n-p Photodiode Structure

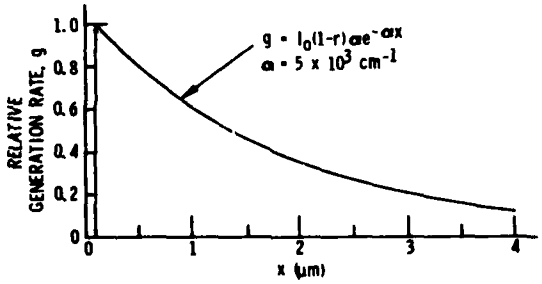

(b) Relative Carrier Generation Rate versus Depth

Figure 4-2. Optical Model for Photodiode Structure

Based on measured mobilities and lifetimes, it is estimated that

$$\mu_n = 1.5 \times 10^5 \text{ cm}^2/\text{volt-sec}$$
$$\mu_p = 8 \times 10^2 \text{ cm}^2/\text{volt-sec}$$
$$\tau_n = 1 \times 10^{-7} \text{ sec}$$
$$\tau_p = 1 \times 10^{-8} \text{ sec}$$

Substituting these values in equation (47) and taking T = 77°K gives $L_n = 100\ \mu m$ and $L_p = 2.3\ \mu m$. Thus, it is seen that minority carriers on both sides of the junction will be efficiently collected with this junction design.

In addition, an antireflection coating of ZnS or In_2S_3 was applied to the front surface to prevent the loss of incident radiation by the front surface reflectance. An uncoated HgCdTe surface reflects about 36% of the incident radiation. With the antireflection coating, this is reduced to less than 5% at a wavelength of 10.6 μm.

Another feature of the n^+-n-p junction design which is shown in Figure 4-2(a) is that the heavily doped n^+ layer produces a barrier, which prevents hole flow to the front surface thereby reducing the front surface recombination velocity to essentially zero. Besides contributing to the very efficient collection of holes produced in the n-layer, this feature also reduces thermally generated diffusion current from the n-layer which could make a significant contribution to the dark current if the surface recombination velocity is high.

Figure 4-3 shows the calculated implant ion profiles used for the final junction design. Projected ranges and standard deviations were calculated using the theory of Linhard, et al.,[22] and data tables provided in the book by Gibbons, et al.[23] For the n-type junction-forming implant at 110 keV, the projected range R_p was 0.2552 μm and the standard deviation ΔR_p was

---

[22] J. Linhard, M. Scharff, and H.E. Shiøtt, Kgl. Danske Vid. Selsk., Matt.-Fys. Medd. 33, No. 14 (1963).

[23] J.F. Gibbons, W.S. Johnson, and S.W. Mylroie, "Projected Range Statistics," Published by Dowden, Hutchinson and Ross, Stroudsberg, PA (1975).

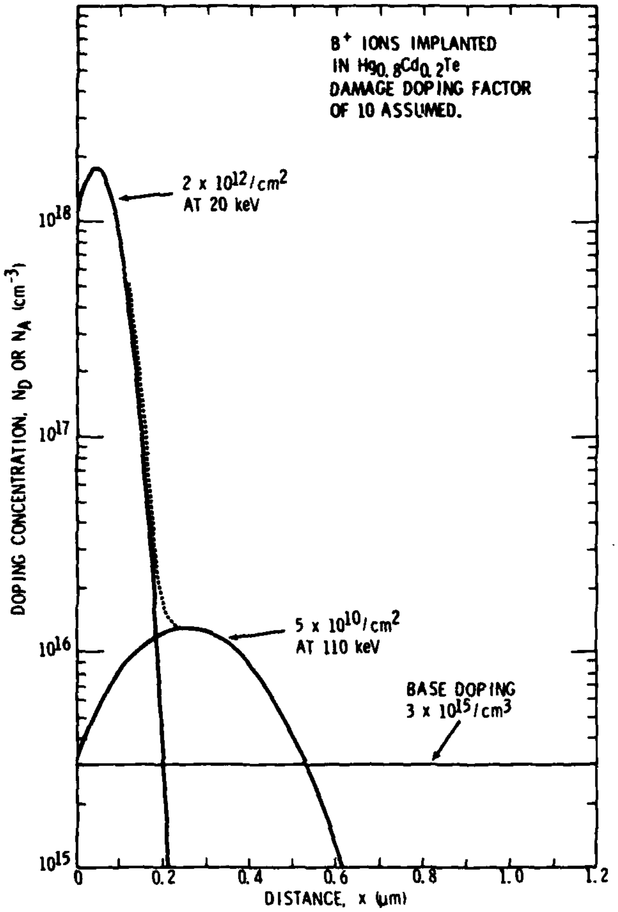

Figure 4-3. Calculated Implanted Ion Profiles for B^+ into $Hg_{0.8}Cd_{0.2}Te$ (Assumed Damage Factor of 10)

0.1600 μm. For the n^+ surface implant at 20 keV, the projected range was 0.0442 μm and the standard deviation was 0.0440 μm.

Assuming a base doping concentration of $3\times10^{15}/cm^3$, it is seen from Figure 4-3 that the junction will be located about 0.53 μm below the implanted surface.

It has been assumed that the n-regions are predominantly damage doped. Previous work has indicated that the damage doping is n-type in character and about 10 times the actual B implant concentration.[24] The damage can be

---

[24] SBRC IR&D funded work (1978).

removed by a post-implant anneal; however, this was not done for the junctions made during this program. In the case of a light ion being implanted into a heavy lattice (which is the case for B into HgCdTe) calculations have shown that the peak of the damage distribution is very close to the peak of the implanted ion distribution.[25] The width (standard deviation) of the damage distribution is somewhat narrower (≈2/3) than the implanted ion distribution. Thus, the data in Figure 4-3 should be accurate in regard to the position of the peaks, but only approximate in regard to width of the distribution.

An alternate approach to p-n junction formation was also tried during this program. This involved diffusion of Hg atoms into unannealed p-type material at a temperature of about 250°C. The Hg atoms fill up Hg vacancies and convert a thin layer near the surface to n-type. Thus, this approach also produces an n-on-p structure. To produce the n^+ layer, a shallow B ion implant or 500Å of indium was deposited prior to the Hg diffusion process.

This approach was not as successful as the ion-implant junction formation method. About a dozen quadrant arrays in the 2×2 mm^2 size were fabricated and tested in two different lots. The best photodiodes were inferior to the best fabricated by the ion-implant technique. Therefore, the diffused junction approach was not pursued further during the course of the program.

This is not to be construed that the diffused junction technique is impractical. The number of arrays tested was only a small sample in a statistical sense; furthermore, the results could have been affected by other processing variables. The decision to abandon the diffused junction approach was dictated primarily by the lack of sufficient time and funding to pursue an additional parallel approach to junction formation.

---

[25] J.W. Mayer, et al., "Ion Implantation into Semiconductors," Academic Press, New York, p. 73 (1970).

ARRAY FABRICATION METHODS

A set of procedures was worked out for fabrication of quadrant arrays with either 1 × 1 mm^2 or 2 × 2 mm^2 sensitive areas per quadrant. The array designs are shown in Figures 4-4 and 4-5. Each quadrant array is a monolithic structure with four individual mesa-type photodiodes having a 0.1-mm spacing between them. The spacing was an arbitrary value chosen for ease of fabrication. A much closer spacing, down to about 0.01 mm could be achieved if necessary. The top electrode was confined to the outer edges of the array so that there would be no obscuration in the center. Because of the area taken up by the top contact, the actual junction area is greater than the nominal sensitive area. In the case of 1 × 1 mm^2 quadrants, the junction area

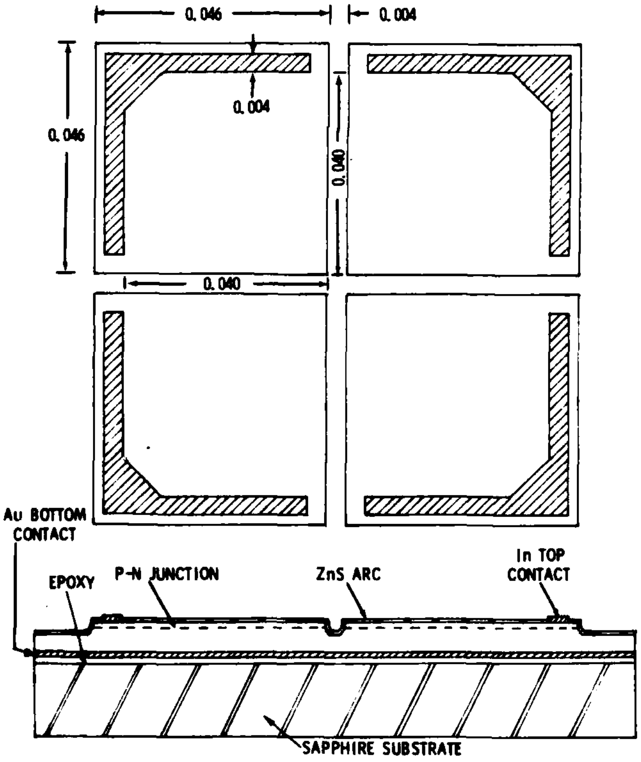

Figure 4-4. Diagram of 1 × 1 mm^2 Quadrant Array (Dimensions in inches)

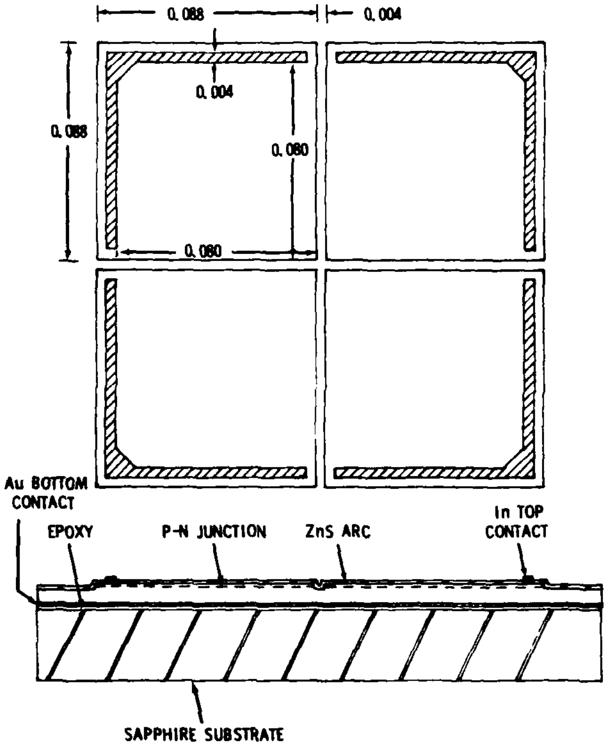

Figure 4-5. Diagram of 2 × 2 mm^2 Quadrant Array (Dimensions in inches)

was 1.36 mm^2 and in the case of 2 × 2 mm^2 quadrants, the junction area was 4.99 mm^2. The top contact metal was indium and the bottom contact metal was gold. An antireflection coating (ARC) of ZnS or In_2S_3 was deposited over the top of the mesa by thermal evaporation. This coating was nominally a one-quarter-wave coating which reduced the reflection loss at 10.6 μm to less than 5%. The antireflection coating also served to provide a passivation of the HgCdTe surface.

The processing procedure worked out for the fabrication of these large area PV HgCdTe detectors was as follows:

1. Obtain annealed p-type HgCdTe wafer
2. Lap and etch back side
3. Plate back side with Au

4. Saw wafer into chips of appropriate size
5. Mount chip on Ti/Au metallized sapphire substrate with conducting epoxy
6. Polish and etch top side
7. Ion implant top side
8. Apply photoresist pattern to define area for top metal contact
9. Evaporate In top metal
10. Remove photoresist and excess evaporated In
11. Apply photoresist pattern to define desired quadrant array
12. Etch mesas
13. Remove photoresist
14. Attach Au lead wire to corner of In contact with conducting epoxy
15. Attach gold wire to base contact on the Ti/Au metallization of the sapphire substrate
16. Evaporate antireflection coating
17. Mount in dewar for test.

This basic processing procedure was employed for all of the 1 × 1 mm^2 quadrant arrays and most of the 2 × 2 mm^2 quadrant arrays fabricated on this program.

Subsequently, in an effort to improve the performance of 2 × 2 mm^2 quadrant arrays, a new design was tried which utilized a planar device structure with gate-control electrodes around the perimeter of the p-n junctions. This design is shown in Figure 4-6. Also included with the quadrant array were two small area diodes (0.010-inch diameter junctions) and two MIS capacitors (0.010 inch diameter) to evaluate the surface properties of the insulator coating.

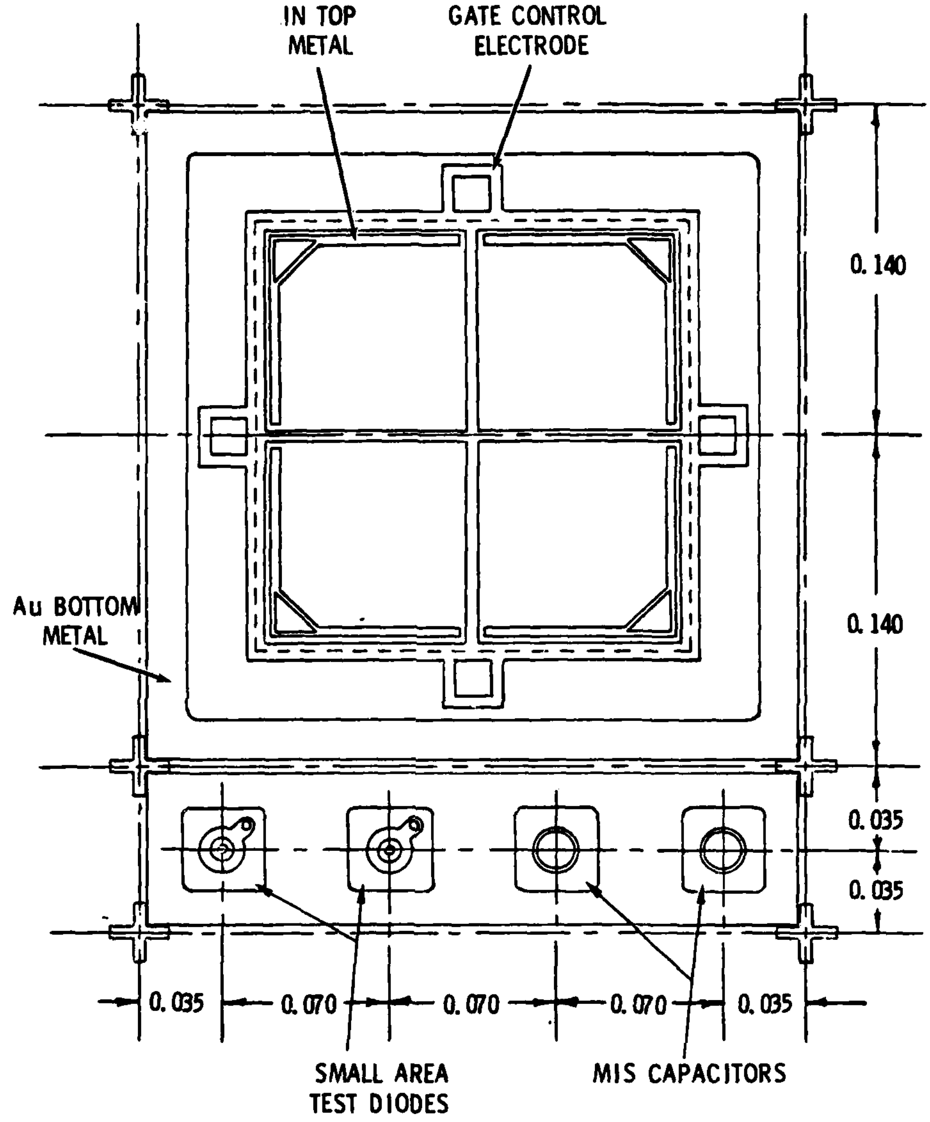

Figure 4-6. Diagram of 2×2 mm^2 Quadrant Array Planar Structure with Gate Control Electrode (Dimensions in inches)

Section 5

DETECTOR TEST RESULTS

This section provides information on the test results from both 1 × 1 mm^2 and 2 × 2 mm^2 quadrant detector arrays. The early part of the program was devoted to an exploratory development effort designed to work out practical fabrication procedures and to evaluate various HgCdTe wafers from different ingots. Many of these early quadrant arrays exhibited poor performance and it would serve no purpose to report those test results here. Only the results on the best arrays will be given since these represent the latest state of the art, and are of more interest to the user organizations. The results on 1 × 1 mm^2 quadrant arrays will be presented first, followed by the results on 2 × 2 mm^2 quadrants.

1 × 1 mm^2 QUADRANT ARRAYS

Data are reported on two 1 × 1 mm^2 quadrant arrays, both of which were packaged in glass dewars and shipped as deliverable contract items. The testing included current versus voltage, 500 °K blackbody responsivity, spectral response, noise versus frequency, spot scan, and pulse response measurements to radiation from a GaAs laser diode. From these basic test data, the relevant detector parameters were obtained either directly or after suitable calculations.

The two quadrant arrays were designated QD-3 and QD-4. Figures 5-1 and 5-2 show the measured current-voltage curves at a temperature of approximately 80 °K. Note that the current scale changes by a factor of 10 between the two figures. The photodiodes of QD-4 have a lower dynamic resistance than those of QD-3.

Figures 5-3 and 5-4 show the relative spectral response curves for the two arrays. The point to be noted here is that the long-wavelength cutoff λ_c of QD-4 is greater than that of QD-3. This implies that the HgCdTe energy

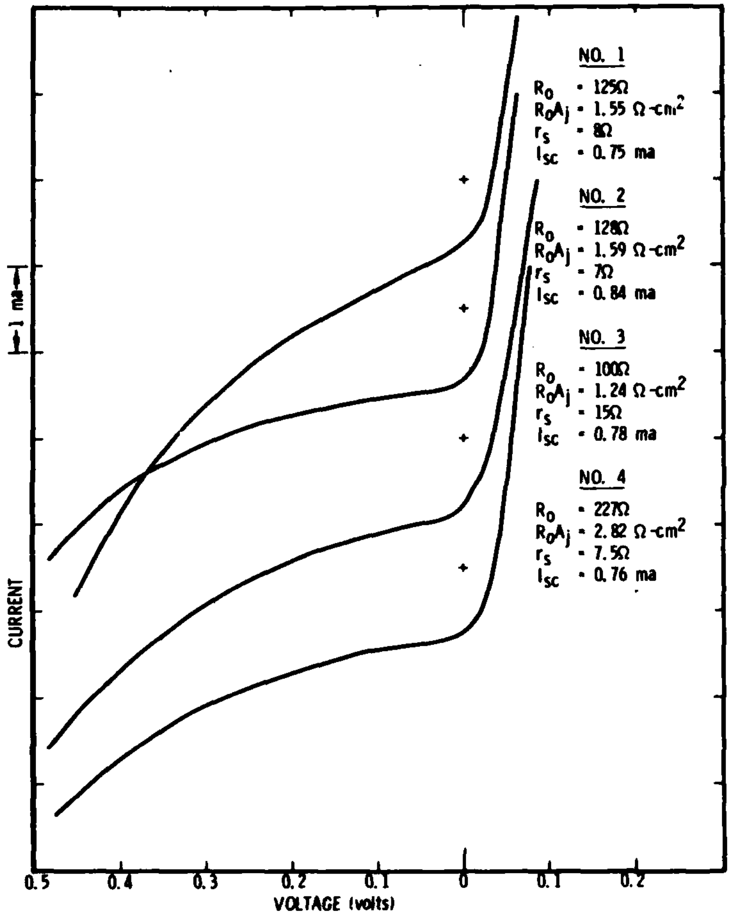

Figure 5-1. Current versus Voltage Characteristics for QD-3 Array (The Zero for the Current Scale has been Displaced for Clarity)

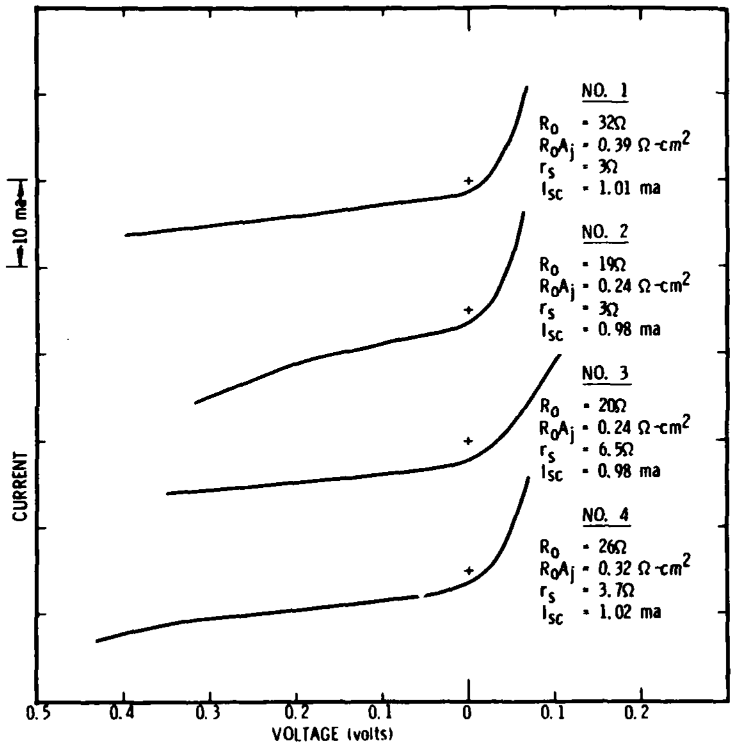

Figure 5-2. Current versus Voltage Characteristics for QD-4 Array (The Zero for the Current Scale has been Displaced for Clarity)

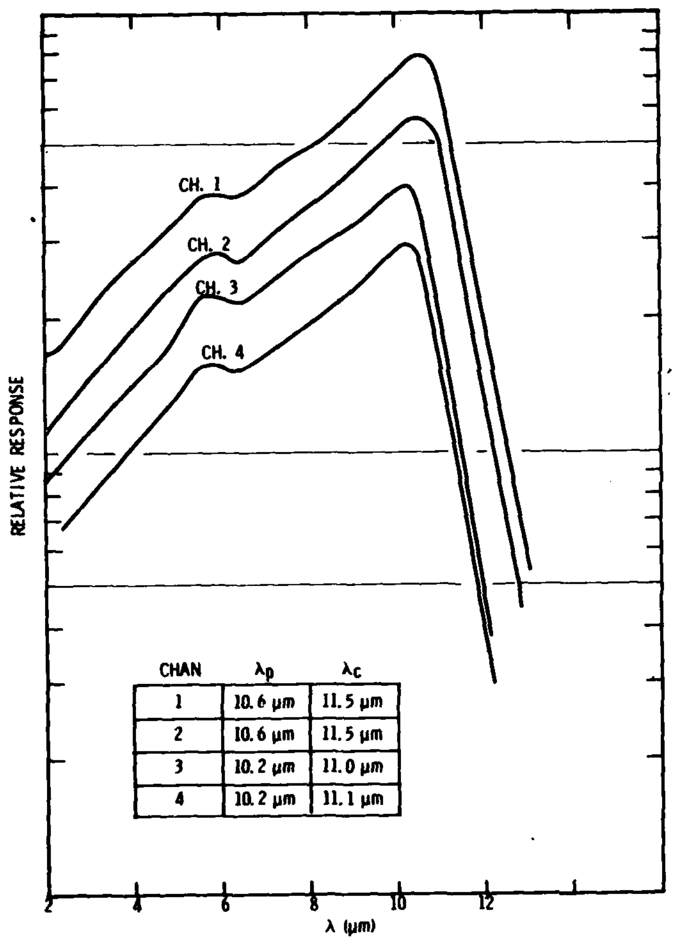

CHAN	λ_p	λ_c
1	10.6 μm	11.5 μm
2	10.6 μm	11.5 μm
3	10.2 μm	11.0 μm
4	10.2 μm	11.1 μm

Figure 5-3. Relative Spectral Response Curves for QD-3 Array at 80°K

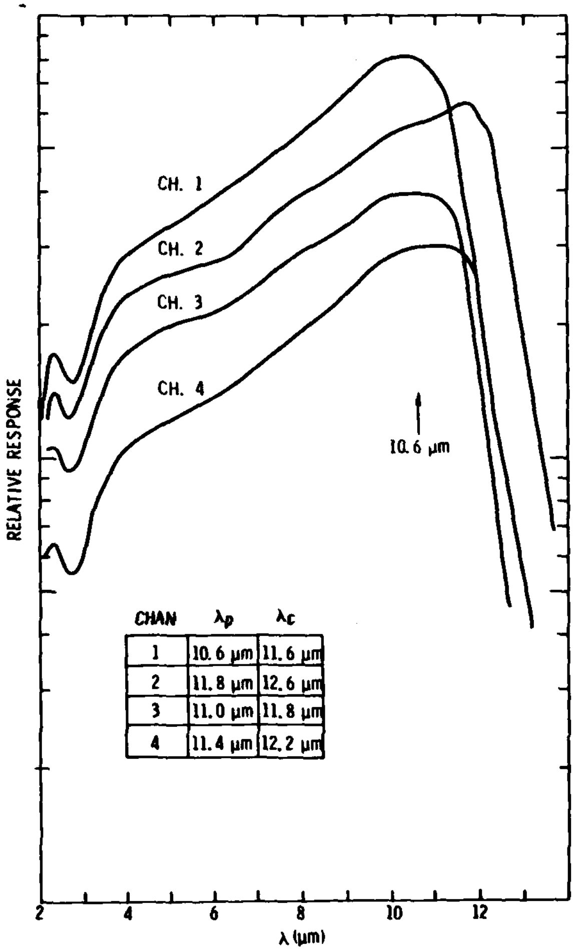

CHAN	λ_p	λ_c
1	10.6 μm	11.6 μm
2	11.8 μm	12.6 μm
3	11.0 μm	11.8 μm
4	11.4 μm	12.2 μm

Figure 5-4. Relative Spectral Response Curves for QD-4 Array at 80°K

bandgap is slightly smaller for the QD-4 array. This smaller bandgap is, for the most part, responsible for the lower resistance of the QD-4 array.

The current responsivity of the quadrant arrays was measured using a 500°K blackbody radiation source chopped at 1800 Hz. With the known spectral response shape for each detector, and the measured blackbody value, the current responsivity at the wavelength of peak response was obtained by standard calculations. These peak values were found to be about 6 amps/watt. From the well-known equation for current responsivity of a photodiode

$$I_R(\lambda) = \frac{\eta e \lambda}{hc} \tag{48}$$

the quantum efficiency η was then calculated and found to be in the range 40% to 70% for the two quadrant arrays. Another method for calculating quantum efficiency was also employed. This utilized the equation for the short-circuit dc photocurrent observed in the current-voltage characteristics. This equation is

$$I_{sc} = \eta e Q_B A \tag{49}$$

By calculating the ambient background photon flux density Q_B falling on the detector's sensitive area A, and using measured values of I_{sc} from Figures 5-1 and 5-2, quantum efficiencies in the range 50% to 60% were obtained. These are considered to be in good agreement with the values obtained from blackbody ac response measurements.

The responsivity at high frequencies was obtained by measuring the detector's response to a square pulse of radiation from a GaAs laser diode. The details of this measurement are described in the interim report previously provided.[26] This measurement results in a value for the detector response time τ. Knowing this and the responsivity at some low frequency, then the responsivity at any frequency may be obtained from

$$I_R(f) = \frac{I_R(o)}{\sqrt{1 + (2\pi f \tau)^2}} \tag{50}$$

---

[26] See Reference 1.

where $I_R(o)$ is the measured low-frequency value.

Figures 5-5 through 5-8 show the calculated responsivity values plotted as a function of frequency. Here we plot voltage responsivity rather than current responsivity. The voltage responsivity is given by

$$R_v(f) = I_R(f)R_f \tag{51}$$

where R_f is the feedback resistor in the current-mode preamplifier which had a value of 1000 ohms.

Also shown in Figures 5-5 through 5-8 are measured noise data as a function of frequency. The noise values in volts/Hz$^{\frac{1}{2}}$ are referred to the input of the preamplifier. In the midband frequency range, the noise is predominantly background photon generated shot noise in the p-n junction. This can be seen from the following calculations. The photon generated shot noise is given by

$$v_n/\sqrt{\Delta f} = (2eI_{sc})^{\frac{1}{2}} R_f \tag{52}$$

From Figures 5-1 and 5-2 it is seen that I_{sc} is about 0.8 ma for QD-3 and 1.0 ma for QD-4. Using these values in equation (52) along with the R_f value of 1000 ohms, the calculated detector noise voltage is 1.6×10^{-8} volt/Hz$^{\frac{1}{2}}$ for QD-3 and 1.8×10^{-8} volt/Hz$^{\frac{1}{2}}$ for QD-4. If we also include the measured preamplifier noise of 0.8×10^{-8} volt/Hz$^{\frac{1}{2}}$ by taking the square root of the sum of the square of the individual noise voltages, we find

$$v_n/\sqrt{\Delta f} = 1.8\times 10^{-8} \text{ volt/Hz}^{\frac{1}{2}} \text{ for QD-3}$$

and

$$v_n/\sqrt{\Delta f} = 2.0\times 10^{-8} \text{ volt/Hz}^{\frac{1}{2}} \text{ for QD-4}$$

These calculated values are seen to be in good agreement with the measured noise data in the midband frequency range. At lower frequencies, 1/f noise from both detector and preamplifier is seen to be present. At higher frequencies, the noise is boosted by the preamplifier feedback circuit as predicted by the theory presented in Section 2.

It is concluded from this analysis of the noise data that these two quadrant arrays are operating close to the background limited (BLIP) condition.

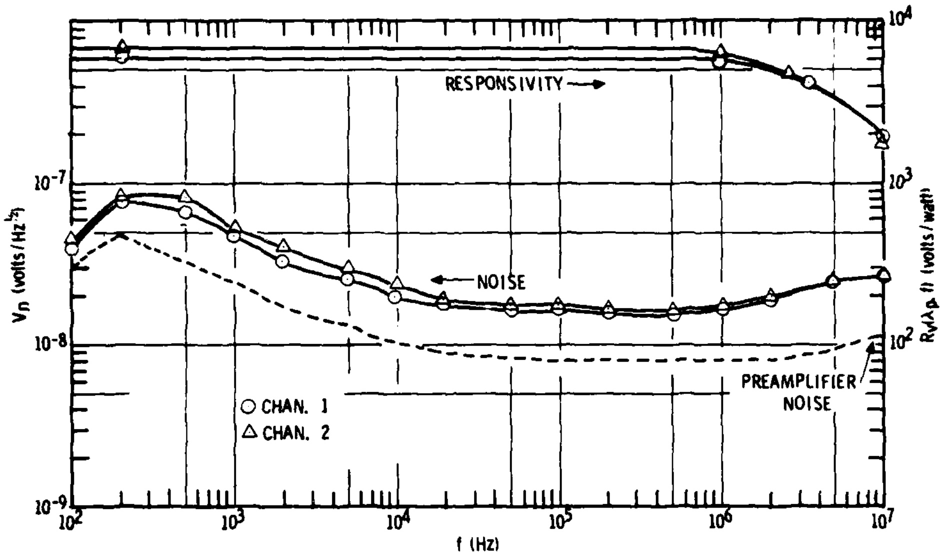

Figure 5-5. Responsivity and Noise as a Function of Frequency for Channels 1 and 2 of QD-3

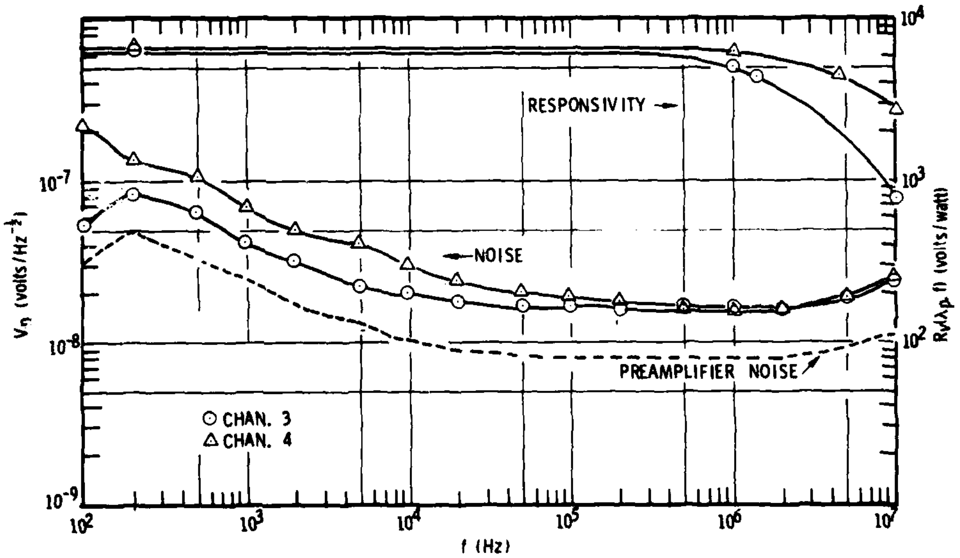

Figure 5-6. Responsivity and Noise as a Function of Frequency for Channels 3 and 4 of QD-3

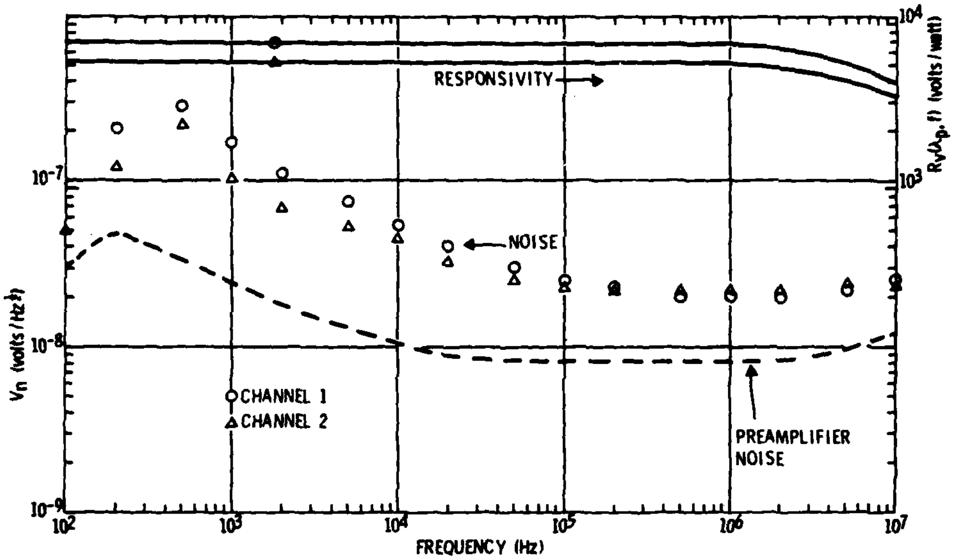

Figure 5-7. Responsivity and Noise versus Frequency for Channels 1 and 2 of QD-4

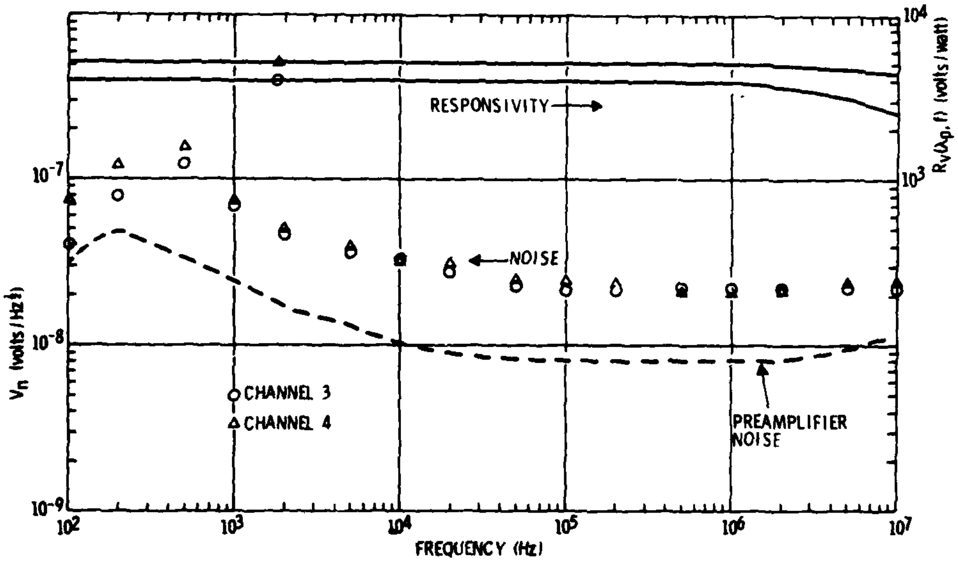

Figure 5-8. Responsivity and Noise versus Frequency for Channels 3 and 4 of QD-4

A reduction in background photon flux either by reduction of the field-of-view angle or by using a cold spike filter in front of the detector could be expected to cause a reduction in noise level and an increase in detectivity. By doing this, the noise could be reduced to about 0.8×10^{-8} volt/Hz$^{\frac{1}{2}}$ with a resultant increase in detectivity by a factor of 2 to 2.5.

The detectivity for these two quadrant arrays may be calculated at any frequency from the responsivity and noise data of Figures 5-5 through 5-8 using the expression

$$D^*(\lambda_p, f) = \frac{R_v(\lambda_p, f)\sqrt{A}}{v_n(f)/\sqrt{\Delta f}} \qquad (53)$$

When this is done, we find $D^*(\lambda_p, f)$ values of about 4×10^{10} cm Hz$^{\frac{1}{2}}$/watt for QD-3 and about 3×10^{10} cm Hz$^{\frac{1}{2}}$/watt for QD-4 at a frequency of 1 MHz. At a frequency of 10 MHz, the $D^*(\lambda_p, f)$ values drop to the order of 1×10^{10} cm Hz$^{\frac{1}{2}}$/ watt or less for both arrays.

The sensitivity contours of these two quadrant arrays were determined by scanning a small spot of focused blackbody radiation (≈ 0.001 inch diameter) across the sensitive areas. Details of the apparatus used for this measurement were presented in the interim report previously furnished on this program. The sensitivity contours are shown in Figures 5-9 and 5-10. Each of these figures gives composite contours for the full quadrant array. Only one quadrant was active for each scan (i.e., the same preamplifier was used for each of the four channels). Therefore, the scans only give information as to optical crosstalk between channels. No data indicating the amount of electrical crosstalk were taken.

The uniformity of sensitivity across each element of the quadrants is seen to be quite good. The uniformity was calculated to be ±2% for each element of QD-3 and from ±3% to ±5% for QD-4. The sharp dips in sensitivity at the left- and right-hand edges of each quadrant are due to obscuration by the top metal contacts.

Tables 5-1 and 5-2 summarize the relevant detector parameters for the two demonstration 1×1 mm^2 quadrant arrays.

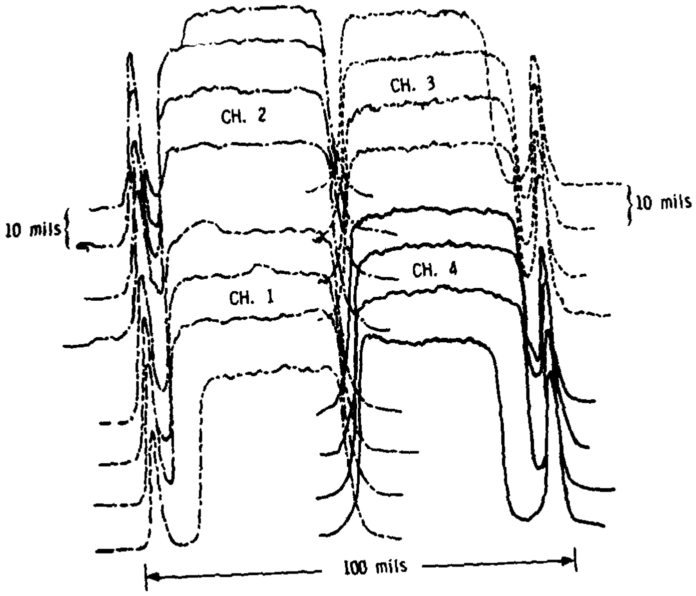

Figure 5-9. Sensitivity Contours of QD-3

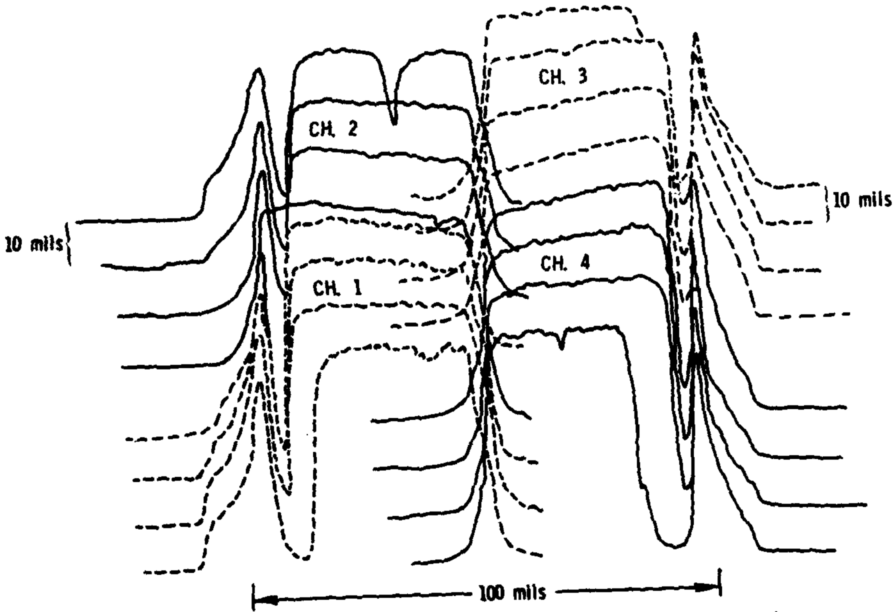

Figure 5-10. Sensitivity Contours of QD-4

Table 5-1. Summary of Detector Parameters for QD-3 at 80 °K

MEASUREMENT	CH. 1	CH. 2	CH. 3	CH. 4
RESPONSE TIME (ns)	45	60	110	35
λ_p (μm)	10.6	10.5	10.2	10.3
λ_c (μm)	11.5	11.5	11.0	11.1
R_o (Ω-cm^2)	125	128	100	227
R_oA (Ω-cm^2)	1.55	1.59	1.24	2.82
I_{sc} (ma)	0.75	0.84	0.78	0.76
$\eta(I_{sc})$ (%)	51	57	60	57
$\eta(I_r)$	64	74	68	72
SPOT SCAN UNIFORMITY (%)	±2	±2	±2	±2
I_r (λ_p, 0) (amps/watt)	5.90	6.89	6.30	6.69
I_r (λ_p, 1M) (amps/watt)	5.68	6.45	5.18	6.53
R_v (λ_p, 0) (volts/watt)	5900	6890	6300	6090
R_v (λ_p, 1M) (volts/watt)	5677	6447	5183	6534
D^*(λ_p, 1M) (cm Hz$^{1/2}$/watt)	4.00×10^{10}	4.38×10^{10}	3.52×10^{10}	4.61×10^{10}
f_{3db} (MHz)	3.5	2.7	1.4	4.5

Table 5-2. Summary of Detector Parameters for QD-4 at 80 °K

MEASUREMENT	CH. 1	CH. 2	CH. 3	CH. 4
RESPONSE TIME (ns)	30	25	25	10
λ_p (μm)	10.6	11.8	10.6	11.0
λ_c (μm)	11.6	12.6	11.8	12.2
R_o (Ω-cm^2)	32	19	20	26
R_oA (Ω-cm^2)	0.39	0.24	0.24	0.32
I_{sc} (ma)	1.01	0.98	0.98	1.02
$\eta(I_{sc})$ (%)	67	52	62	60
$\eta(I_r)$	74	52	41	53
SPOT SCAN UNIFORMITY (%)	±3	±5	±5	±4
I_r (λ_p, 0) (amps/watt)	6.89	5.31	3.94	5.21
I_r (λ_p, 1M) (amps/watt)	6.77	5.25	3.89	5.20
R_v (λ_p, 0) (volts/watt)	6890	5310	3892	5210
R_v (λ_p, 1M (volts/watt)	6771	5246	3892	5200
D^*(λ_p, 1M) (cm Hz$^{1/2}$/watt)	3.73×10^{10}	2.72×10^{10}	2.02×10^{10}	2.69×10^{10}
f_{3db} (MHz)	5.3	6.4	6.4	15.9

OTHER TEST RESULTS

Certain other tests and data analysis were performed on the photodiodes made during this program. These are described in this section.

Junction Capacitance

Measurements of junction capacitance versus reverse bias voltage were performed as a means to determine the doping profile at the p-n junction. Accurate capacitance measurements could not be obtained on large area photodiodes because of their low resistance. Therefore, smaller area diodes were made by the same fabrication procedures and used for C-V analysis. These diodes were 0.008× 0.009 inch square (total junction area of 4.6×10^{-4} cm^2). The measurements were made using a PAR 410 C-V plotting instrument operating at a frequency of 1 MHz. Figure 5-11 shows representative C-V data. The slope of the straight line region indicates that $C \propto V^{-0.59}$ which is close to the expected $V^{-0.5}$ dependence expected for an

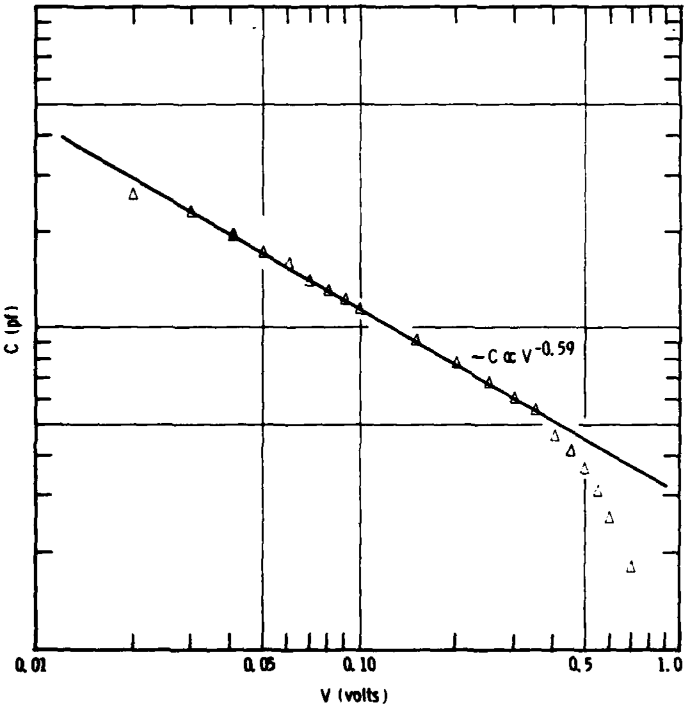

Figure 5-11. *Junction Capacitance as a Function of Reverse Bias for a Small Area Diode*

abrupt junction. A plot of $1/C^2$ versus V yielded a value of 4.3×10^{14} cm^{-3} for the effective doping concentration $N_A N_D/(N_A+N_D)$ in the junction depletion region. This is considerably less than the base acceptor doping concentration measured by the Hall effect which was in the range 3 to 6×10^{15} cm^{-3} for these samples. (See Section 2 for typical Hall data.) We infer from this result that a close compensation is occurring between the implanted B donor atoms and the base material Au acceptor atoms.

Diffusion Limited R_oA_j

An analysis of R_oA_j product values for the better junctions made on this program indicates that they are diffusion limited. Figure 5-12 shows measured R_oA_j plotted versus energy bandgap for three different 1 × 1 mm^2 quadrant arrays at a temperature of 78 °K. The energy bandgap was determined for each diode from its spectral cutoff and the relation

$$E_g = \frac{hc}{\lambda_c} \tag{54}$$

There is a strong dependence of R_oA_j on E_g which varies approximately as $1/n_i^2$. The diodes with the highest R_oA_j are those made on HgCdTe material

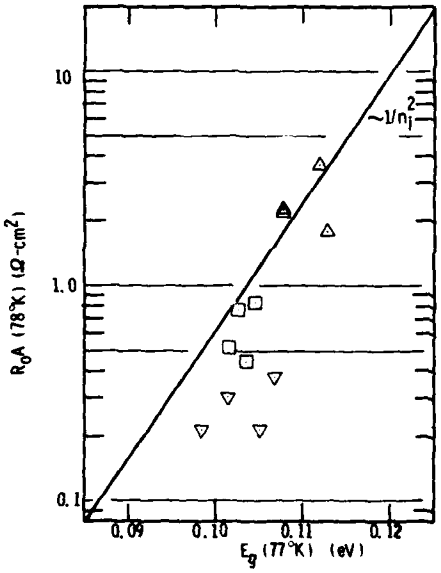

Figure 5-12. R_oA Product Measured at 78 °K as a Function of the Energy Gap

having a λ_c value close to 10.6 μm; i.e., an E_g value of about 0.11 eV. Diodes made on material with smaller bandgaps suffer a reduction in R_oA_j value.

From the theory presented in Section 2, an expression for R_oA_j can be written as follows.

$$R_oA_j = \frac{kT}{eJ_s} = \frac{N_a}{n_i^2 e}\left(\frac{\tau_n kT}{\mu_n e}\right)^{\frac{1}{2}} \tag{55}$$

This represents the R_oA_j value determined by minority carrier (electron) diffusion from the p-side of the junction. Minority carrier (hole) diffusion from the n-side can be neglected because it is so thin. This equation shows explicitly the inverse relation between R_oA_j and n_i. Values for n_i as a function of energy bandgap and temperature can be obtained from Schmit's formula[27]

$$n_i = [9.908 - 5.21x + 3.07(10^{-4})T + 5.94(10^{-3})Tx]10^{14} E_g^{3/4} T^{3/2} \exp(-E_g/2kT). \tag{56}$$

Other bulk material parameters are also known which will permit a theoretical calculation of R_oA_j. Measured electron lifetimes were about 2×10^{-7} sec for acceptor doping concentrations N_A in the range 3 to $5\times 10^{15}/\text{cm}^3$. A typical value for electron mobility μ_n at 78°K is 1.5×10^{15} cm^2/volt-sec. With the following set of values

$E_g = 0.1$ eV
$T = 78$°K
$n_i = 6.5\times 10^{13}$ cm^{-3}
$\mu_n = 1.5\times 10^{5}$ cm^2/volt-sec
$\tau_n = 2\times 10^{-7}$ sec
$N_A = 4\times 10^{15}$ cm^{-3}

the calculated R_oA_j from equation (55) is 0.56 ohm-cm^2. This determines one point on the theoretical curve of Figure 5-12 and is seen to be in reasonable agreement with the experimental R_oA_j values. This, plus the $1/n_i^2$

---

[27] J. L. Schmit, unpublished data (1972).

dependence shown, leads to the conclusion that these photodiodes are diffusion limited at 78°K.

Pulse Response versus Bias

The detector response time τ was determined by observing on an oscilloscope the signal decay after illumination by a 100-nsec wide pulse from a GaAs laser diode. The response time is defined as the time taken for the signal pulse to decay to 1/e (37%) of its peak amplitude. At low reverse bias voltage, response times were generally in the range 10 to 100 nsec.

The response time is expected to be RC limited with C determined mainly by junction capacitance and R being the load resistance. Since C decreases with reverse bias, it is expected that τ will also reflect this decrease. Figure 5-13 shows a plot of measured τ values plotted versus reverse bias using a 50-ohm load.

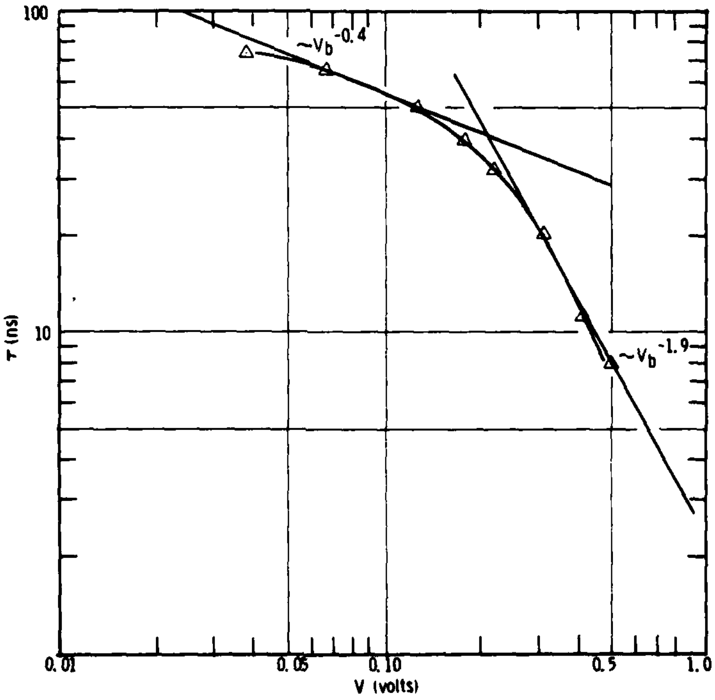

Figure 5-13. RC Limited Lifetime Plotted as a Function of Reverse Bias for One Element from QD-3

For small reverse bias ($\lesssim 0.1$ volt) the response time decreases roughly as $V_R^{-0.4}$. This is approximately as expected from the dependence of junction capacitance on reverse bias [see equations (24) and (25) in Section 2]. At large reverse bias (>0.2 volt) the response time drops much more rapidly. This is presumably due to the reduced dynamic impedance of the junction in this bias range; that is, the junction impedance is approaching or becomes less than 50 ohms.

2 × 2 mm^2 QUADRANT ARRAYS

After successful completion of the demonstration 1 × 1 mm^2 quadrant arrays, work was started on 2 × 2 mm^2 arrays using the same fabrication techniques with a simple scale-up to the larger element size. The array configuration was previously shown in Figure 4-5. About 50 of these quadrant arrays were fabricated from various HgCdTe wafers and probe tested for I-V characteristics at 77°K. The results of most I-V curves were generally poor, showing zero bias dynamic resistance of about 10 ohms and nearly ohmic characteristics. The better diodes exhibited I-V curves such as shown in Figure 5-14. Part (a) of this figure shows a set of I-V curves from a 2 × 2 mm^2 quadrant array made by the B ion implantation process. Part (b) shows a set of curves for a similar array where the junction was formed by Hg in-diffusion.

At first glance, one might conclude that these would be reasonably good photodiodes. Calculated R_oA_j values were in the range 0.5 to 1.0 ohm-cm^2 and reverse to forward resistance ratios were on the order of 10 to 1. However, the measured short-circuit currents were too small, indicating a low quantum efficiency. For a 2 × 2 mm^2 element, the measured short-circuit current under a 2π steradian FOV of room temperature background should be greater than 3 ma. This calculation is made with equation (49) using a quantum efficiency of 0.7. The diodes in Figure 5-11 have values of 1 to 2 ma.

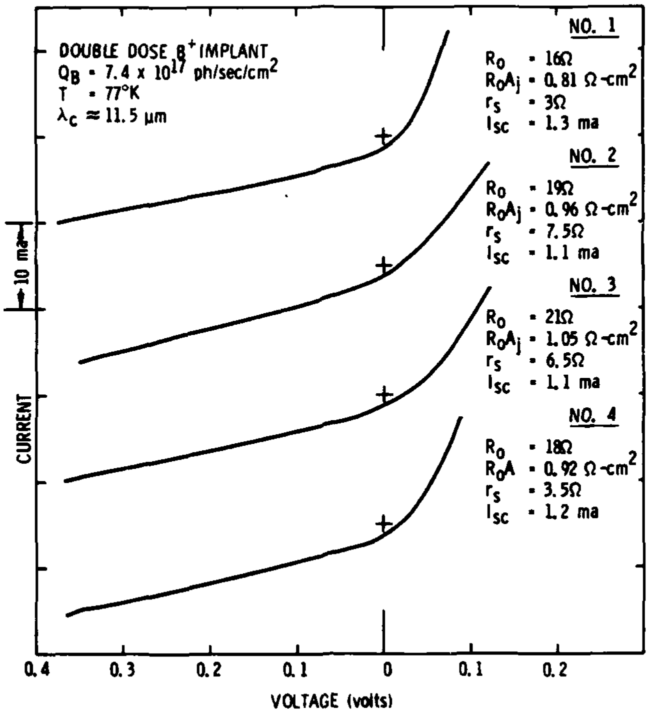

(a) Array No. V34-1G-B

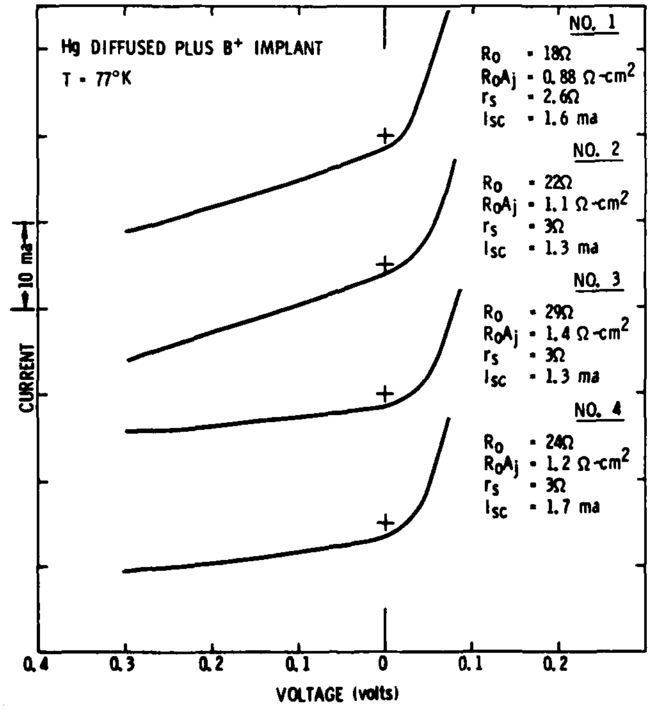

(b) Array No. V46-1D-C

Figure 5-14. Current versus Voltage Curves for Two 2×2 mm^2 Quadrant Arrays

When the sensitivity contours were measured on these large area detectors, it was found that the problem was not due to low quantum efficiency but was a result of a poor sensitivity contour as illustrated in Figure 5-15. These data show that the sensitivity is peaked near the top metal electrodes and falls off as the light spot is moved away. The effective sensitive area of the detector is actually much less than the geometrical 2×2 mm^2 area.

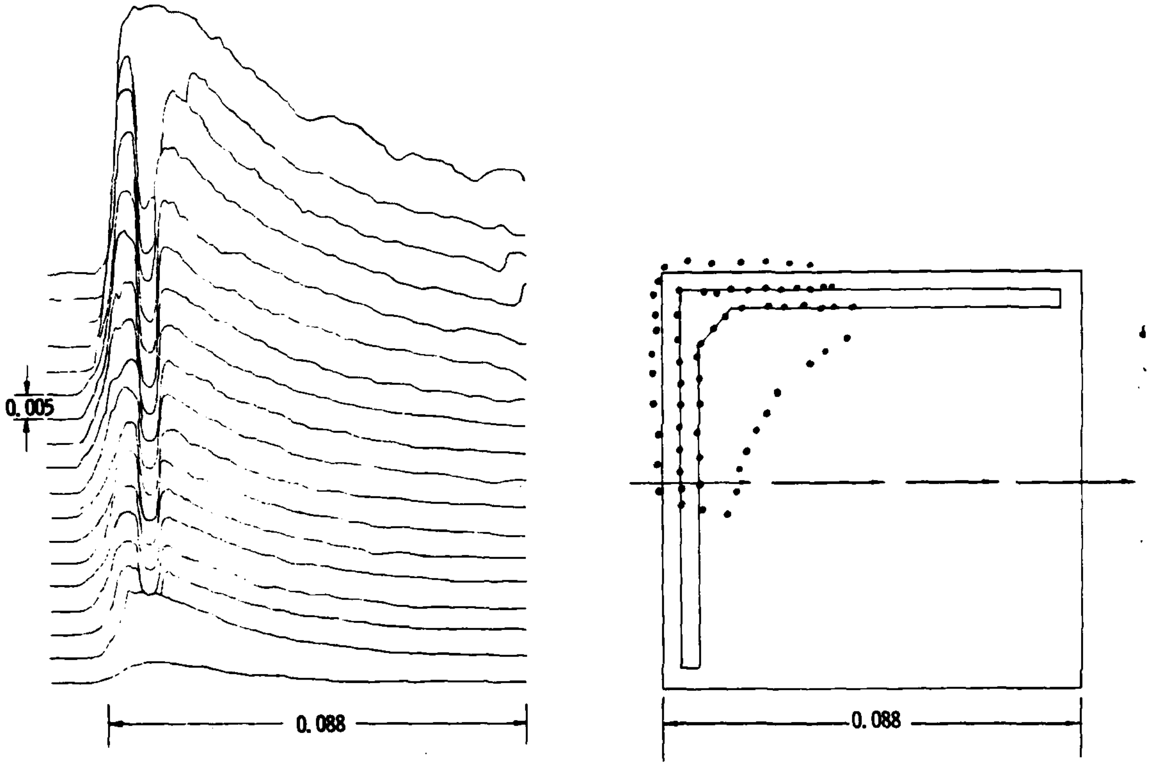

(a) Spot Scan Profiles at 0.005-inch Intervals. Arrows on (b) Show Direction of Spot Scan Across Element

(b) 50% Response Points Superimposed on an Outline of the Detector's Physical Dimensions

Figure 5-15. Spot Scan Uniformity Data Taken on One 2×2 mm^2 Element of Quadrant Array No. V34-1G-B

The reason for this behavior is that the sheet resistance of the n-type top layer of the p-n junction is of the same order of magnitude as the junction resistance. This impedes the flow of photocurrent to the top electrode and forces some fraction of the photocurrent to flow back across the junction. Thus, the externally measured photocurrent is reduced.

To further illustrate this situation, an electrical equivalent circuit for the photodiode is shown in Figure 5-16. The photodiode is broken up into a large number of elemental areas each with its own elemental photocurrent generator I_{pi} and elemental junction resistance R_{ji}. These elemental areas are interconnected by sheet resistance elements r_{si}. A single resistor R_B is sufficient to account for the resistance of the base region.

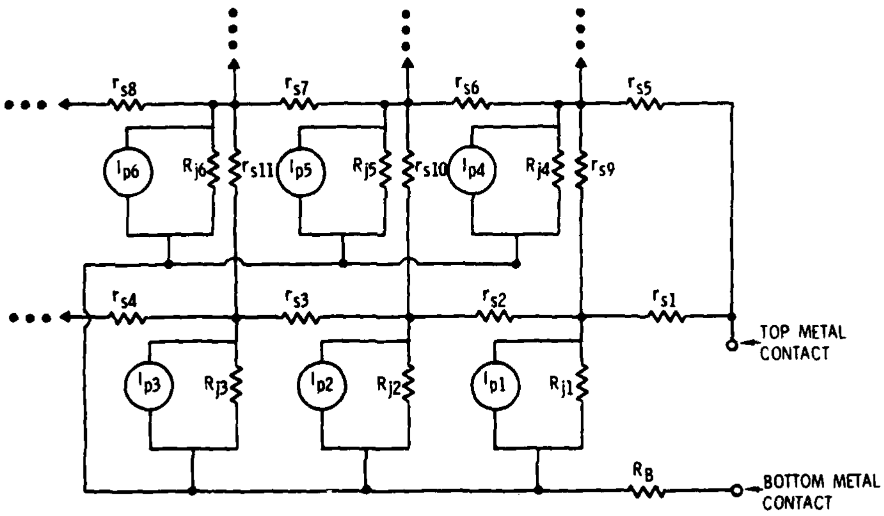

(a) Distributed Circuit Network

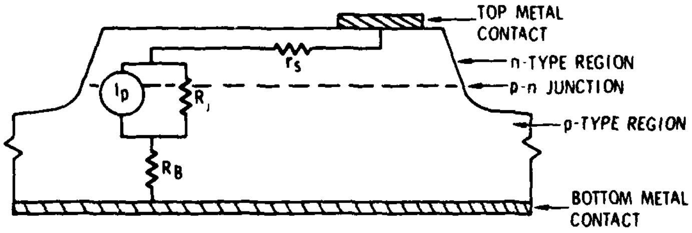

(b) Circuit for a Single Elemental Region

Figure 5-16. Electrical Equivalent Circuits for a Large Area Photodiode Including Sheet Resistance

A detailed analysis of this circuit would be beyond the scope of this report. However, the effect of sheet resistance may be adequately illustrated by considering a single elemental area not too close to the top metal electrode. We then have a simple series circuit as shown in Figure 5-16(b). It can be shown that the externally measured short-circuit photocurrent from this circuit is given by

$$I_{sc} = \frac{I_p R_j}{(R_j + R_B + r_s)} \tag{57}$$

R_B can be calculated from

$$R_B = \rho_B \frac{x_p}{A_j} \tag{58}$$

where ρ_B is the base material resistivity, x_p the base thickness and A_j the junction area. Using the values

$\rho_B = 1$ ohm-cm
$x_p = 0.01$ cm
$A_j = 0.04$ cm^2

we find that $R_B = 0.25$ ohm which is negligible compared to expected R_j and r_s values. Then equation (57) can be written

$$I_{sc} = \frac{I_p R_j}{(R_j + r_s)} \tag{59}$$

It is clear from this equation that when R_j and r_s are approximately equal the measured external short-circuit photocurrent will be reduced by about a factor of 2. As r_s becomes larger than R_j even more reduction in I_{sc} results. This occurs for elemental areas farther removed from the top contact.

Subsequent work on this program was directed toward attempts to increase R_j and decrease r_s so that a more uniform sensitivity contour could be achieved. Most of the effort was put toward attempts to increase R_j.

Thin-base structures were incorporated into several of the photodiode lots which were fabricated. Base thicknesses in the range 0.1 to 0.01 mm were employed. The theory described in Section 2 showed that thin-base devices were potentially capable of an order of magnitude increase in R_j

provided that back surface recombination velocity was small enough. None of the thin-base experiments tried showed any indication of R_j increasing as base thickness was decreased. It was concluded from these results that the back surface, which was a gold-plated metal contact, did not constitute a low surface recombination velocity boundary; therefore, no increase in R_j could be achieved with this design.

Another approach toward increasing R_j was based on the idea that surface leakage around the perimeter of the p-n junction might be producing a shunt resistance that would lower the effective R_j. Such a leakage path could have a particularly severe effect in the central part of the quadrant array, and this is just what was being observed in the sensitivity contour plots. A new photoetch mask set was designed which incorporated a gate-control electrode around the perimeter of all four diodes in the quadrant array. By applying a potential to this gate electrode, the energy band bending at the surface could be adjusted so as to minimize surface leakage current. The layout of this new structure was shown previously in Figure 4-6. This design employed a planar approach to photodiode fabrication as opposed to the mesa approach used earlier in the program.

About 30 quadrant arrays were fabricated using this new design. Gold-doped base material was used from several different HgCdTe ingots and the junctions were produced by B ion implantation. The depth of the second implant dose for the n^+ layer was increased by using a 40 keV energy instead of 20 keV. The junction-forming first dose was kept the same at 110 keV.

Current-voltage probe testing of these arrays revealed that no significant improvement in R_j was obtained with this new design. The gate electrode had essentially no effect toward increasing R_j. In many cases, application of gate bias potential decreased detector performance because the gate was shorted to the base material through pin holes in the ZnS insulator.

At this point in the program, further work on the large area detector problem had to be stopped due to lack of time and funding. The best $2 \times 2\ mm^2$ array obtained up to this point was selected for packaging in a glass dewar as a demonstration array. The final test data taken on this array are shown in the following figures.

Figure 5-17 shows the measured I-V curves at a temperature of 80°K. The same symptoms exhibited by the previous 2×2 mm^2 arrays are evident, namely, low junction resistance and low short-circuit photocurrent.

Figure 5-18 shows the measured relative spectral response curves.

Figure 5-19 shows a composite of spot scan sensitivity profiles for each quadrant of the array taken at three different reverse bias voltages, 0 mv, 20 mv, and 40 mv. A slight improvement in signal strength is seen with increasing reverse bias. However, the signal strength from the central area of the quadrant away from the top contact electrodes still contributes a negligible amount of photocurrent.

Figure 20 shows the measured noise versus frequency data obtained from the quadrant array. It was found that the noise spectra were essentially independent of reverse bias voltage up to 0.40 mv. Also shown is a noise spectrum taken with the detector disconnected from the current-mode preamplifier. This is labeled as preamplifier noise. However, this is not a true measure of preamplifier noise with the detector connected because the detector loads down the input to the preamplifier and causes an increase in preamplifier noise. This can be understood by referring to the analysis given in Section 2.

Figure 5-21 presents $D^*(\lambda_p)$ values versus frequency and reverse bias voltage. It is seen that $D^*(\lambda_p)$ increases by about a factor of 3 with 40 mv applied. This is due to the slight improvement in sensitivity contours previously shown in Figure 5-19. Even so, the $D^*(\lambda_p)$ is still down by about one order of magnitude from what was obtained with the 1×1 mm^2 quadrant arrays. The "effective" quantum efficiency (averaged over detector area) for the 2×2 mm^2 arrays is on the order of 3% to 4%, whereas, it was 50% to 70% for the 1×1 mm^2 arrays.

Table 5-3 gives a summary of the relevant detector parameters for the packaged 2×2 mm^2 quadrant array.

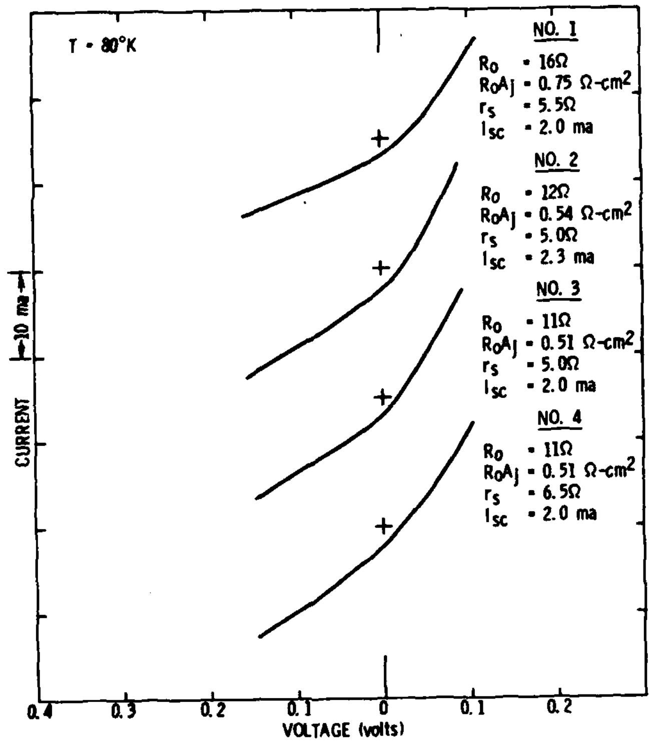

Figure 5-17. Current versus Voltage Curves for 2×2 mm^2 Quadrant Array No. QD-5

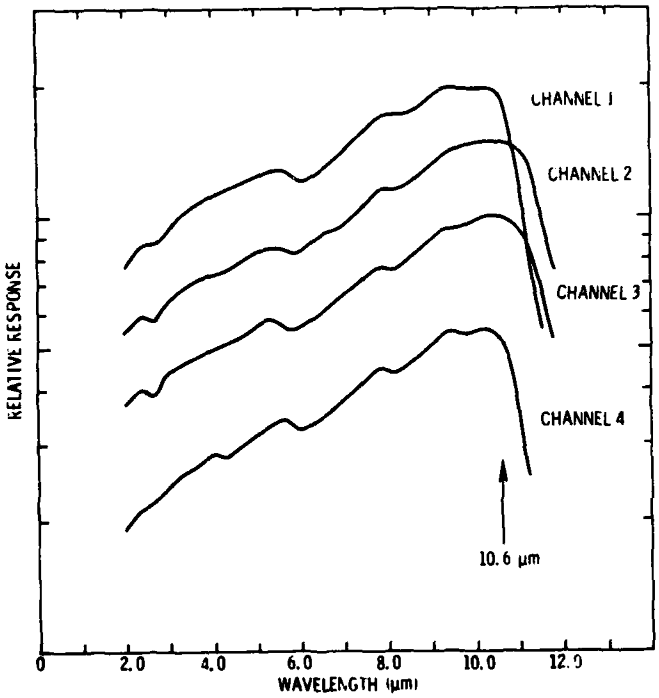

Figure 5-18. Relative Spectral Response for 2×2 mm^2 Quadrant Array No. QD-5

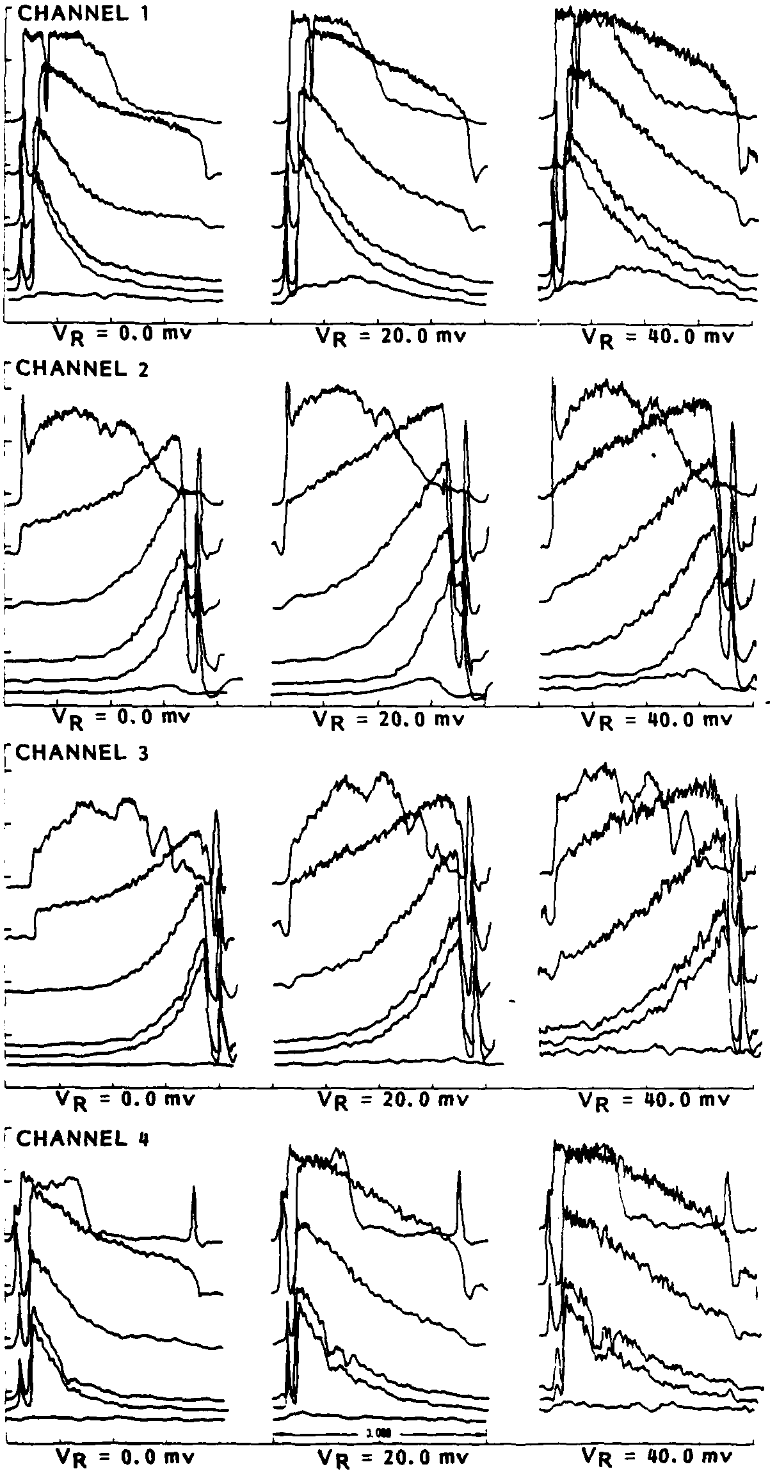

Figure 5-19. Spot Scanner Sensitivity Profiles for 2 × 2 mm^2 Quadrant Array No. QD-5 versus Bias Voltage (T = 80°K)

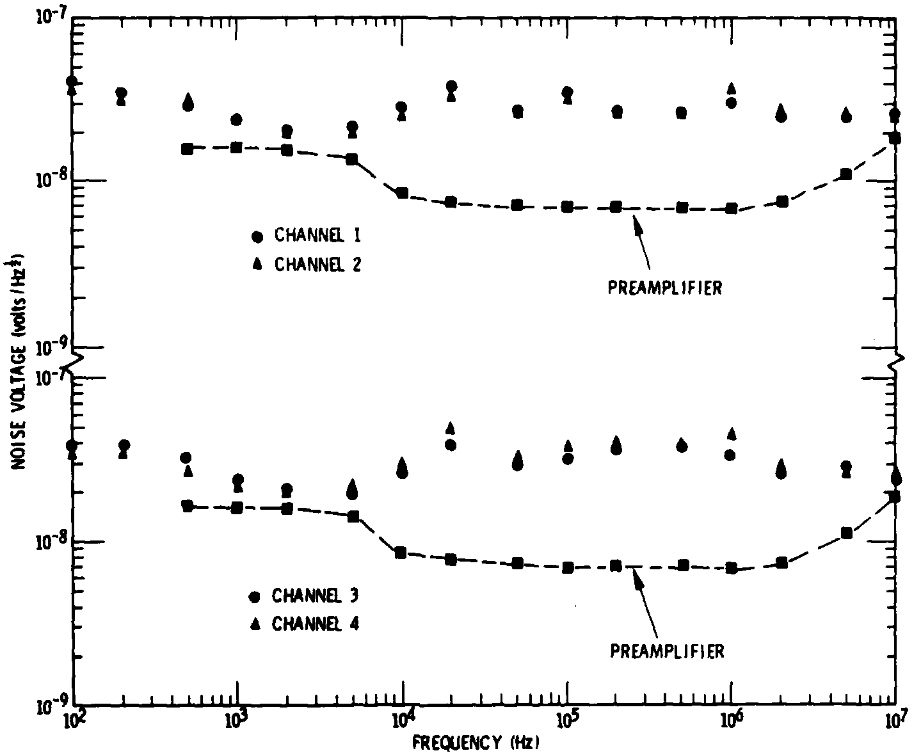

Figure 5-20. Noise versus Frequency for 2×2 mm^2 Quadrant Array No. QD-5

Table 5-3. Test Data Summary - Detector No. QD-5

MEASUREMENT	CHANNEL 1 V_r (mv)			CHANNEL 2 V_r (mv)			CHANNEL 3 V_r (mv)			CHANNEL 4 V_r (mv)		
	0	20	40	0	20	40	0	20	40	0	20	40
τ_r (nsec)	16	20	20	36	40	44	34	36	36	20	26	32
λ_p (μm)	10.4			10.5			10.4			10.3		
λ_c (μm)	11.2			11.8			11.8			11.2		
R_0 (ohms)	16			12			11			11		
R_0A (ohm-cm^2)	0.75			0.54			0.51			0.51		
I_{sc} (ma)	2.0			2.3			2.0			2.0		
$\eta(I_R)$ (%)	1.4	3.0	4.4	1.3	2.5	3.6	1.1	2.2	3.4	0.9	1.7	2.5
$I_R(\lambda_p, 0)$ (amps/watt)	0.165	0.36	0.52	0.16	0.31	0.43	0.14	0.27	0.41	0.11	0.21	0.29
$I_R(\lambda_p, 1\text{MHz})$ (amps/watt)	0.164	0.36	0.52	0.16	0.30	0.41	0.14	0.26	0.40	0.11	0.21	0.28
$R_V(\lambda_p, 0)$ (volts/watt)	165	360	520	160	310	430	140	270	410	110	210	290
$R_V(\lambda_p, 1\text{MHz})$ (volts/watt)	164	360	520	160	300	410	140	260	400	110	210	280
$D^*(\lambda_p, 1\text{MHz})$ (x 10^9 cm Hz$^{\frac{1}{2}}$/watt)	1.1	2.5	3.9	0.85	1.7	2.5	0.80	1.7	2.6	0.46	0.92	1.4
f_{3db} (MHz)	9.9	8.0	8.0	4.4	4.0	3.6	4.7	4.4	4.4	8.0	6.1	5.0

T = 80°K

V_r = REVERSE BIAS VOLTAGE

SENSITIVE AREA = 4.1 x 10^{-2} cm^2 FOR EACH ELEMENT

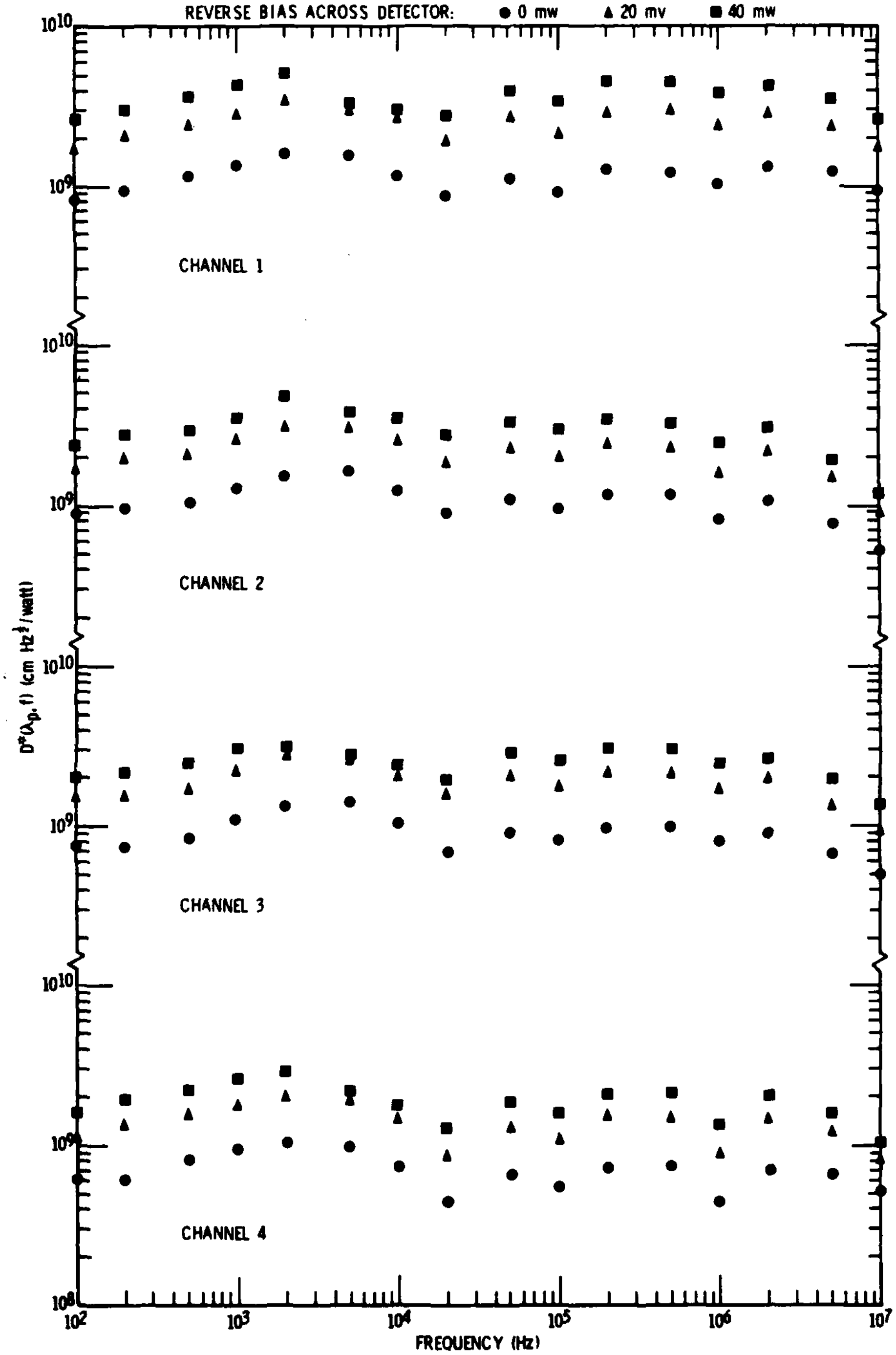

Figure 5-21. Detectivity as a Function of Frequency and Reverse Bias for 2×2 mm^2 Quadrant Array No. QD-5

PACKAGING OF QUADRANT ARRAYS

The quadrant arrays for shipment to ERADCOM were packaged in permanently evacuated glass dewars designed to accept a Joule-Thomson (J-T) expanding gas cryostat to cool the detector. The detector dewar assembly is shown in Figure 5-22. The glass vacuum dewar containing the quadrant array is housed in a protective aluminum housing. The housing is made in two sections which screw together and clamp onto the dewar flange to retain it. A foam material is placed between the glass dewar wall and the metal housing for cushioning against shock and for thermal insulation. For these exploratory development models, the foam material is removable and the glass vacuum dewar can be easily removed from the metal housing. In a production model, the foam would form a permanent seal and the glass vacuum dewar would not be removable.

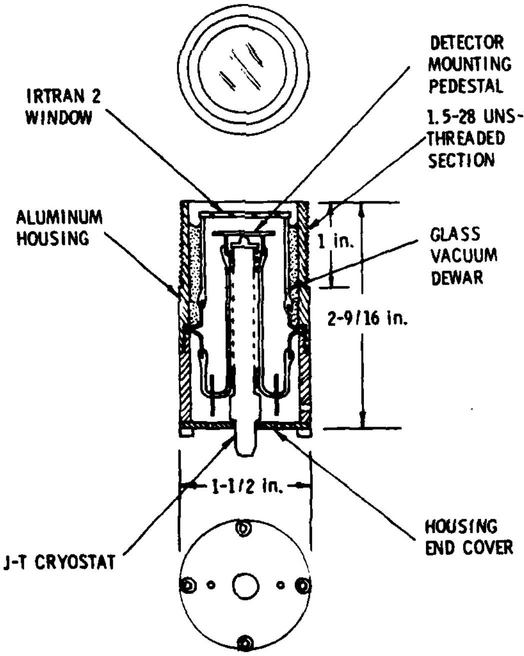

Figure 5-22. Dewar Package Assembly for Large Area PV HgCdTe Quadrant Arrays

An end cover to the metal housing provides protection for the electrical connections to the glass vacuum dewar, and also serves to prevent the J-T cryostat from slipping out of the dewar. This cover is held in place by four socket head screws.

The four detector elements of the quadrant array are designated channels 1 through 4. Figure 5-23 shows a view of the detector housing looking through the Irtran 2 window. This sketch identifies the position of each detector element with respect to channel number.

Four coaxial cables, each 12 inches long, serve to connect the detector elements to the preamplifiers.

The J-T cryostat slips into the cold finger of the glass vacuum dewar. The dewar cold finger is precision honed to 0.3260 ± 0.0002 inch ID, and the cryostat is made to fit tightly into the bore of the cold finger. Included with the J-T cryostat is a molecular sieve filter (Part No. 5684), a 4-foot length of small-diameter high-pressure tubing (Part No. 9169), and a reducer coupling (Part No. 8994) which goes on the end of the filter and couples to the small-diameter tubing.

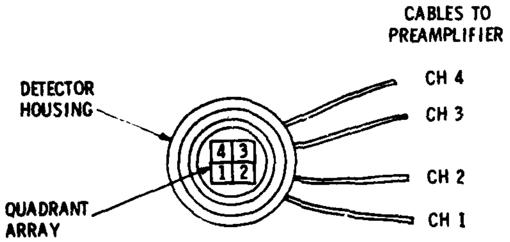

Figure 5-23. View of Quadrant Array Looking through Window

Preamplifiers

The four preamplifier channels are housed in a single box. Power requirement to operate the preamplifiers is 15 volts at 240 ma. Each channel consists of a current-mode first stage with a 1-kilohm feedback resistor followed by a voltage-mode gain stage with a voltage gain of 10.

The frequency response is from less than 1 kHz to greater than 10 MHz without detectors connected. With detectors connected, the frequency response is detector limited to about 3.0 MHz for the high-frequency -3 db point.

The preamplifier output is a negative-going signal. Maximum undistorted output is 0.3 volt if the output is terminated in 50 ohms, or 2 volts if unterminated.

An internal biasing network in each preamplifier channel provides a reverse bias to the detector connected to that channel. For the two 1 × 1 mm^2 quadrant arrays, the reverse bias is 0.03 volt for QD-3 and 0.005 volt for QD-4. For the 2 × 2 mm^2 quadrant array the reverse bias is 0.04 volt.

Figure 5-24 shows the completed detector dewar assembly with detectors connected to the preamplifier.

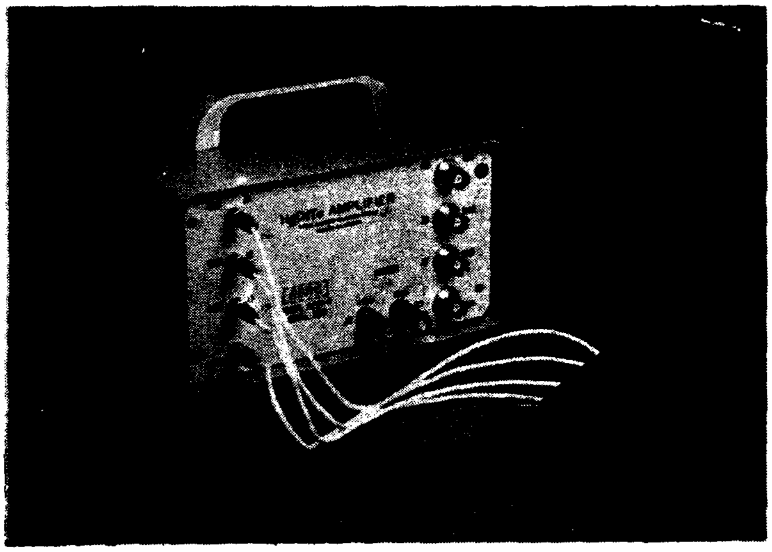

Figure 5-24. PV HgCdTe Large Area Quadrant Array in Dewar Package Coupled to Four-Channel Preamplifier

Section 6

CONCLUSIONS AND RECOMMENDATIONS

Earlier work on this program demonstrated the feasibility of large area PV HgCdTe detectors for laser wavelengths of 2.06 μm and 3.85 μm. Detector elements made from HgCdTe with the alloy composition adjusted for peak response at about 3.85 μm were successfully fabricated up to 5×5 mm^2 in sensitive area and assembled into quadrant arrays with a total area of 10×10 mm^2. Detector elements peaked for 2.06 μm were successfully demonstrated up to 2×2 mm^2 in area, and test results indicated that the technology could be extended to larger areas if desired. Demonstration quadrant arrays and single elements were delivered to ERADCOM for test and evaluation.

For a wavelength of 10.6 μm, detectors up to 1×1 mm^2 in sensitive area were successfully demonstrated. *Monolithic* quadrant arrays with total area of 2×2 mm^2 were fabricated and delivered to ERADCOM for test and evaluation. Attempts to extend the same technology to larger areas were not so successful. The PV HgCdTe detectors with 2×2 mm^2 sensitive areas had low quantum efficiency and nonuniform sensitivity contours due to their low junction resistance being comparable to the sheet resistance of the top n-layer of the p-n junction. The sheet resistance prevents collection of charge from those regions of the sensitive area furthest removed from the top metal contact.

A number of changes in the detector fabrication process have been devised to solve this problem. However, lack of time and funding prevented the successful implementation of these ideas. In any future work on large area detectors for 10.6 μm the following recommendations are made.

- Increase the n^+ layer doping concentration from 10^{18} to 10^{19} cm^{-3}.
- Increase the thickness of the n^+ layer by using a higher implant energy.
- Apply a narrow line metal grid top contact in place of the edge contacts in the present design.
- Develop thin-base technology that will increase junction R_oA_j values.

Alternatively, it would be of interest to attempt to apply a newer technology to the problem of large area PV HgCdTe detectors. This new technology employs heterojunction structures mode by a liquid phase epitaxial technique. Superior p-n junction properties have recently been demonstrated in work at SBRC under other DOD contracts.[28] Additionally, this technology offers the best hope for implementing the thin-base approach toward increasing R_oA_j values in large area PV HgCdTe detectors.

---

[28] K. J. Riley and A. H. Lockwood, Proc SPIE, 217, 206 (1980).

Appendix A

LARGE AREA PV HgCdTe DETECTORS FOR LASER DETECTION AT 3.85 μm

Appendix A

LARGE AREA PV HgCdTe DETECTORS FOR LASER DETECTION AT 3.85 μm*

P. R. Bratt and A. H. B. Vanderwyck
Santa Barbara Research Center
Goleta, California

ABSTRACT

This paper describes the results of a program to develop large area PV HgCdTe detector quadrant arrays for detection of pulsed laser radiation at 3.85 μm. The nominal size of each element of the quadrant was 5×5 mm^2. Detectors were made by boron ion implantation into p-type base material having an acceptor concentration of about 1×10^{15} per cm^3. Detector design criteria were chosen to minimize junction capacitance and series resistance, and to maximize quantum efficiency and speed of response. Typical devices, when operated with an appropriate current-mode preamplifier, had response times of 100 ns. Responsive quantum efficiencies ranged between 60 and 90%. The low frequency detectivities were in the range 2 to 4×10^{11} cm Hz$^{\frac{1}{2}}$/watt which is close to the BLIP limit. High frequency detectivity was 5 to 6×10^{10} cm Hz$^{\frac{1}{2}}$/watt at 1 MHz. Operating temperature was 77°K.

INTRODUCTION

The objective of this work was to design and fabricate large area PV HgCdTe detectors for applications in laser tracking with DF lasers at 3.85 μm. The goal was to make quadrant arrays with each element of the quadrant having a 5×5 mm^2 sensitive area. The response time and sensitivity of the detectors should be sufficient to detect laser pulses having a 100-ns pulse width. This mandates a frequency response extending into the 1- to 5-MHz range.

DETECTOR DESIGN

The usual requirements for a sensitive PV detector are high quantum efficiency and high junction impedance. For the case of high frequency application, there are two additional requirements, namely, low junction capacitance and low series resistance. The detector design criteria were chosen with these factors in mind. A detailed analysis of the high frequency performance of the detector-preamplifier combination is given as an appendix to this paper.

Figure 1 illustrates the detector design. An n$^+$ layer was formed on p-type base material by ion implantation of boron. The implant depth was approximately 0.2 μm. Donor concentrations produced in the n$^+$ layer were in the range 10^{18} to 10^{19} per cm^3. The sheet resistance of the implanted layer was about 5 ohms/□. Figure 1 shows a planar structure which was produced by

---

*This work was carried out for the U.S. Army Electronics Command, Ft. Monmouth, NJ, under Contract No. DAAB07-76-C-0803, Technical Monitor, C. Burke.

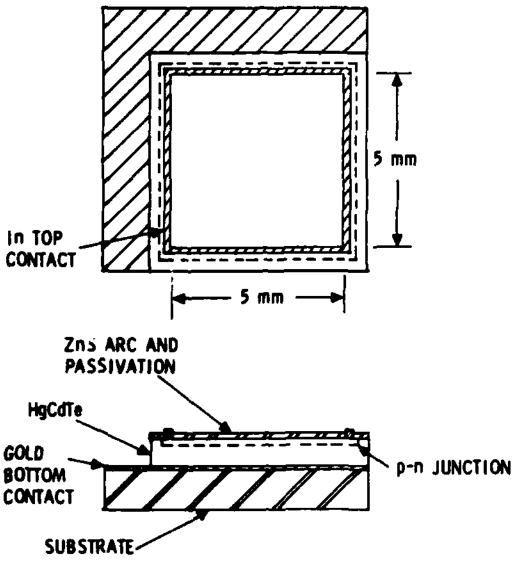

FIGURE 1. LARGE AREA PV HgCdTe DETECTOR DESIGN

masking certain areas of the HgCdTe surface with photoresist to stop the ions. Mesa structures were also made by standard photoresist masking and etching procedures after ion implantation of the whole surface.

Since the n^+ layer is doped to degeneracy, it will be transparent to incident radiation having energy near that of the bandgap due to the Burstein-Moss effect. This radiation will therefore penetrate into the p-type base region and be absorbed there. The minority carrier electrons thus generated have long diffusion lengths and can easily reach the n^+-p junction. Thus, high collection efficiency can be expected.

To reduce junction capacitance, the acceptor concentration in the p-type base region was minimized so as to increase the junction depletion width. The device could thus be classified as a one-sided abrupt junction. The capacitance of such a junction is given by

$$C_j = A_j \left[\frac{\epsilon \epsilon_o q N_B}{2(\phi_B + V)} \right]^{\frac{1}{2}}$$

where ϵ is the HgCdTe dielectric constant, ϵ_o the permittivity of empty space, q the electronic charge, N_B the base doping concentration, ϕ_B the built-in potential, V the external applied voltage, and A_j the junction area. Base acceptor concentrations on the order of 10^{15} per cm^3 were achieved by annealing as-grown HgCdTe wafers in Hg vapor at appropriate temperatures for 4 to 6 weeks. This produced a junction capacitance per unit area of 150 to 200 pf/mm^2. A 5×5 mm^2 detector would therefore exhibit a capacitance of 3750 to 5000 pf.

The bottom contact to the p-type base material was made by gold plating the HgCdTe and then bonding to a gold plated sapphire substrate. The top contact to the n^+ region was evaporated indium. A quarter-wave ZnS antireflection coating was applied on the top of the device. Reflectance measurements made at SBRC have shown that this coating can reduce the reflectance to about 3% at the design wavelength for the coating.

The placement of the HgCdTe detector chip on the sapphire substrate was such that four such detectors could be assembled together to form a quadrant array. Figure 2 shows a photograph of an assembled quadrant.

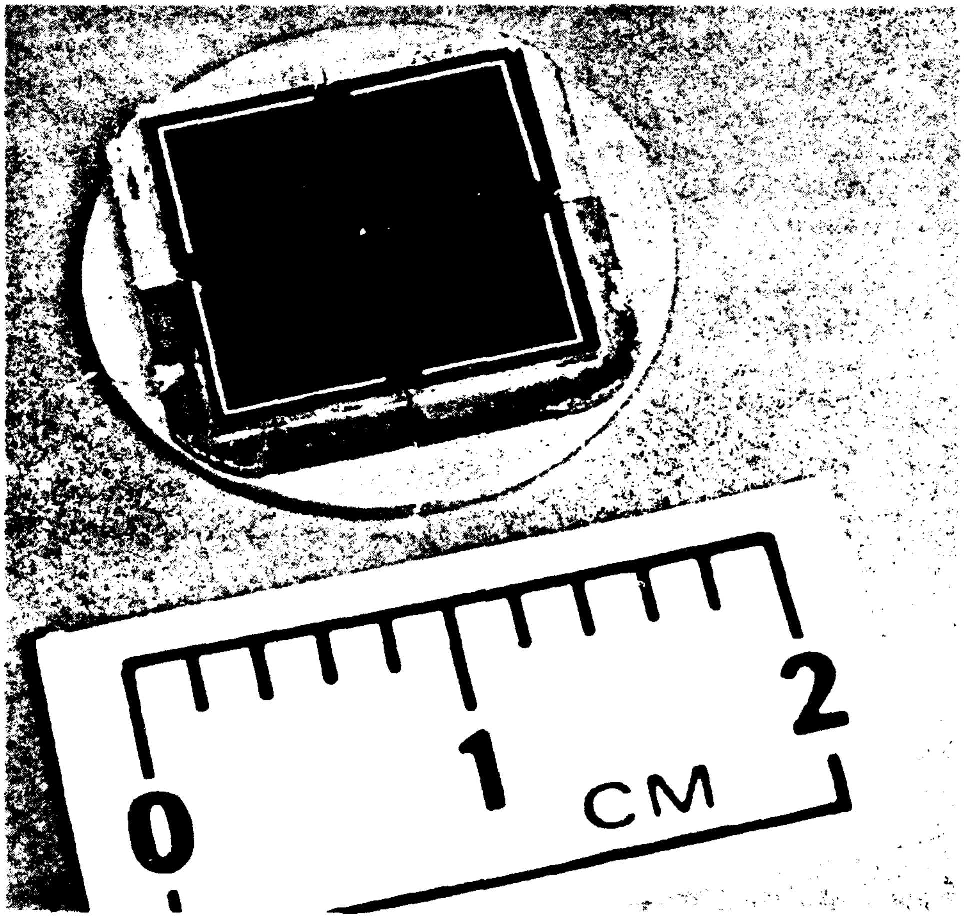

FIGURE 2. PHOTOGRAPH OF LARGE AREA PV HgCdTe DETECTOR QUADRANT ARRAY

The detector element was designed to have a clear area inside the top indium electrode of at least 5 × 5 mm. The actual junction area is 5.6 × 5.6 mm for a total area of 31 mm^2.

DETECTOR PERFORMANCE MEASUREMENTS

Detector performance characteristics were measured on individual elements before assembly into quadrant arrays. In this section, illustrative data are shown for the various measurements that were performed. All data were taken at an operating temperature of 77°K.

CURRENT-VOLTAGE CURVES

Figure 3 shows the current-voltage curve for a representative large area PV HgCdTe detector element. The zero bias dynamic resistance value is 1500 ohms. The series resistance, determined from the large forward current range, is 7 ohms. The reverse breakdown current shows a "soft" characteristic. It is not known at this time whether this is a result of surface leakage or bulk leakage across the junction plane. Zero bias dynamic resistance values for these large area devices have typically ranged from 1000 to 3000 ohms. With a junction area of 0.31 cm^2, this corresponds to an R_0A product of 310 to 930 ohms cm^2.

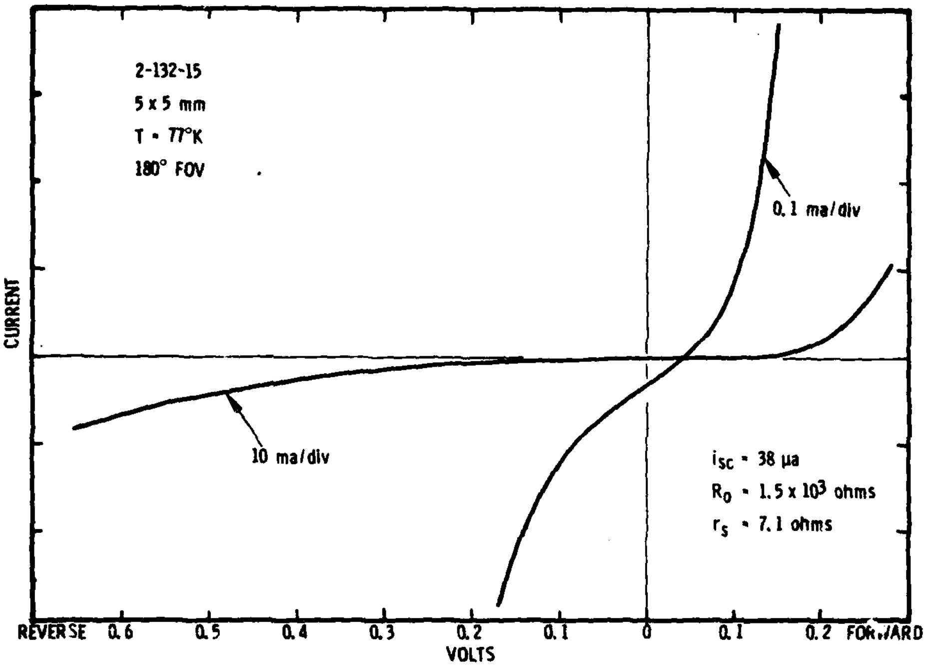

FIGURE 3. TYPICAL CURRENT-VOLTAGE CHARACTERISTICS FOR A LARGE AREA PV HgCdTe DETECTOR

SPECTRAL RESPONSE

A typical spectral response curve is shown in Figure 4. The $Hg_{1-x}Cd_xTe$ starting material was grown with an alloy composition of x = 0.31. As seen in the figure, this gives a peak spectral response at 77°K very close to the 3.85-μm laser wavelength.

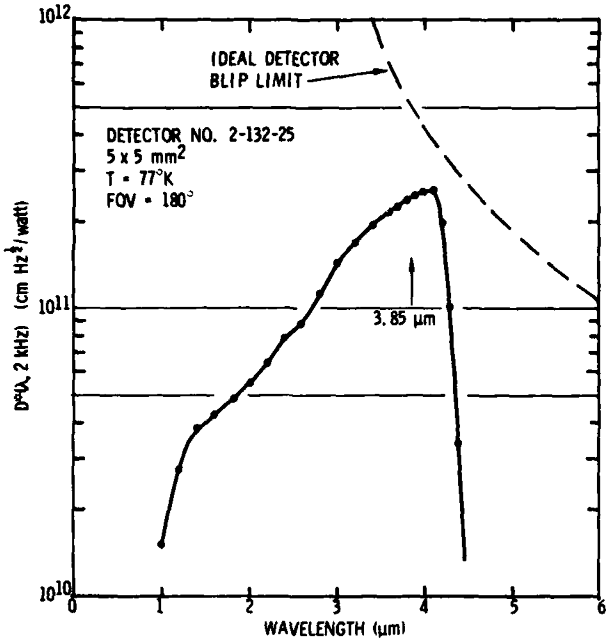

FIGURE 4. SPECTRAL DETECTIVITY OF A TYPICAL LARGE AREA PV HgCdTe DETECTOR

SENSITIVITY CONTOUR

The sensitivity contour was tested using a fine spot scanner. The radiation source in the scanner was an 800°K blackbody. Radiation from the blackbody was focused to a spot size approximately 0.002 inch in diameter. Translation of the spot across the detector sensitive area was achieved by keeping the spot fixed and moving the detector which was attached to an x-y precision translation table. Figure 5 shows typical contour curves obtained for one x and one y scan across a nominal 5 × 5 mm^2 detector.

PULSE RESPONSE TIME

Detector pulse response times were measured using a GaAs laser diode. The laser output pulse width was 100 ns with a pulse rise and fall time of less than 1 ns. Figure 6 shows a tracing from an oscilloscope picture which indicates the response time of a typical detector when illuminated by such a pulse. The response time, defined as the time taken for the signal amplitude to decay from maximum to 37% of maximum, was measured as 120 ns for this detector. The measurement was taken using the current-mode preamplifier designed for this program. The "effective" input impedance of the preamplifier was 20 ohms.

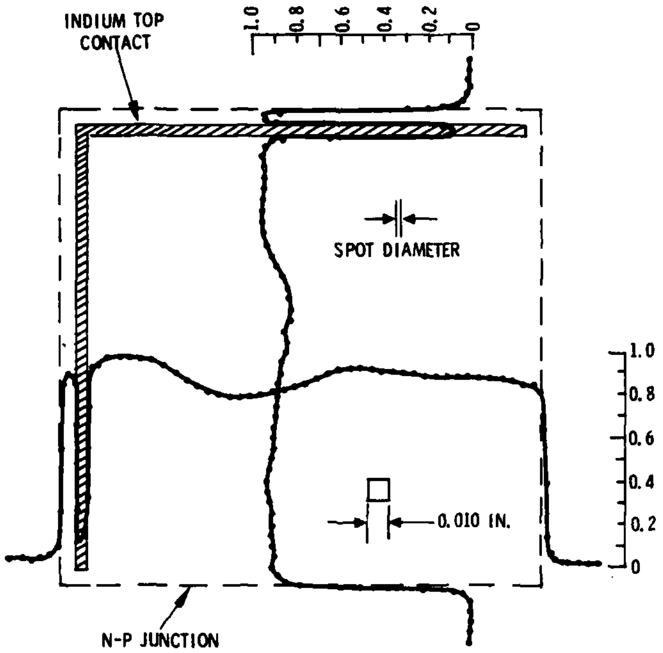

FIGURE 5. LARGE AREA PV HgCdTe SENSITIVITY CONTOURS.
Detector No. 2-132-103

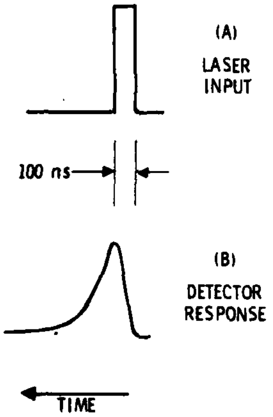

FIGURE 6. RESPONSE OF A TYPICAL LARGE AREA
PV HgCdTe DETECTOR TO A LASER PULSE.
Detector No. 2-132-15, τ = 120 ns

DETECTIVITY

Detectivity data were acquired on these detectors by direct measurements at low frequencies and by an indirect method at high frequencies. Low frequency measurements were made with a low-noise current-mode preamplifier having a 10-kohm feedback resistor. Signal and noise measurements were made in the conventional manner by chopping a blackbody source and reading values of signal and noise voltage on a wave analyzer. For a measuring frequency of 2 kHz, detectivities at spectral peak were in the range 2 to 4×10^{11} cm $Hz^{\frac{1}{2}}$/watt. Table I shows data on several detectors which were fabricated on this program. The D* values for the higher resistance devices are close to the BLIP limit for an ideal detector. Values of responsive quantum efficiency calculated from the short circuit current responsivity ranged between 60% and 90%.

TABLE I. MEASURED CHARACTERISTICS OF SEVERAL LARGE AREA PV HgCdTe DETECTORS

ELEMENT NO.	R_0 (ohms)	C_0 (pf)	λ_p (μm)	λ_c (μm)	$I_r(\lambda_p, 0)$ (amps/watt)	η (%)	$R_v(\lambda_p, 0)$ (volts/watt)	$D^*(\lambda_p, 2\ kHz)$ (cm $Hz^{\frac{1}{2}}$/watt)	τ (ns)	$R_v(\lambda_p, 1\ MHz)$ (volts/watt)	N_1 (1 MHz) (volts/$Hz^{\frac{1}{2}}$)	$D^*(\lambda_p, 1\ MHz)$ (cm $Hz^{\frac{1}{2}}$/watt)
2-132-11	2420	4407	3.8	3.9	2.46	81	2460	3.8×10^{11}	100	2080	20.6	5.4×10^{10}
2-132-13	1700	3927	3.7	---	2.50	84	2500	2.9×10^{11}	100	2120	17.7	6.4×10^{10}
2-132-14	2200	5750	3.7	3.9	2.37	80	2370	3.2×10^{11}	100	2010	19.0	5.6×10^{10}
2-132-15	1500	3923	3.8	3.9	1.85	61	1850	2.4×10^{11}	120	1480	15.2	5.2×10^{10}
2-132-25	800	--	4.1	4.3	2.82	85	2820	2.6×10^{11}	100*	2390	--	
2-132-94	1700	4930	3.6	3.8	2.48	86	2480	2.8×10^{11}	100*	2100	--	
2-132-103	1090	4331	3.6	3.8	2.58	89	2580	3.0×10^{11}	100*	2180	--	

*ESTIMATED VALUE OPERATING TEMPERATURE = 77°K FOV = 180° DETECTOR AREA = 0.284 cm^2

Such high D* cannot be maintained at high frequencies because of device capacitance. To obtain high frequency D* data, a current-mode preamplifier with a 1-kohm feedback resistor was used. Noise data were taken by direct measurements in the MHz range with a high-frequency wave analyzer. Signal values for the MHz range were calculated by assuming that the current responsivity $I_r(\lambda_p, f)$ has a frequency dependence which goes as

$$I_r(\lambda_p, f) = I_r(\lambda_p, 0)\,[1 + (2\pi f \tau)^2]^{-\frac{1}{2}}$$

where $I_r(\lambda_p, 0)$ is the low frequency value obtained from a chopped blackbody measurement and τ is the detector response time measured with the GaAs laser diode. Once these latter values are known, the current responsivity at any frequency can be obtained from the above equation. Voltage responsivity referred to the output of the preamplifier was then obtained from the equation

$$R_v(\lambda_p, f) = I_r(\lambda_p, f)\,R_f$$

where R_f is the 1-kohm feedback resistance. From this calculated value of voltage responsivity and the measured noise voltage, D* at any frequency can be obtained. Table I shows D* values for a frequency of 1 MHz obtained in this manner. Typical values are 5 to 6×10^{10} cm $Hz^{\frac{1}{2}}$/watt.

Figure 7 shows a plot of responsivity, noise and D* for a typical large area PV HgCdTe detector. The various contributions to the total noise spectrum are indicated by dashed lines. Noise measurements were taken with two different sets of measuring equipment, one for the low frequency range and one for high frequencies. The overlap range is 10 to 50 kHz. Agreement to within 40% was obtained in this overlap range.

Some indication of 1/f noise is evident in Figure 7 at the lower frequencies. This originates mainly in the preamplifier. This noise will not make a significant contribution to the total broadband noise of the system.

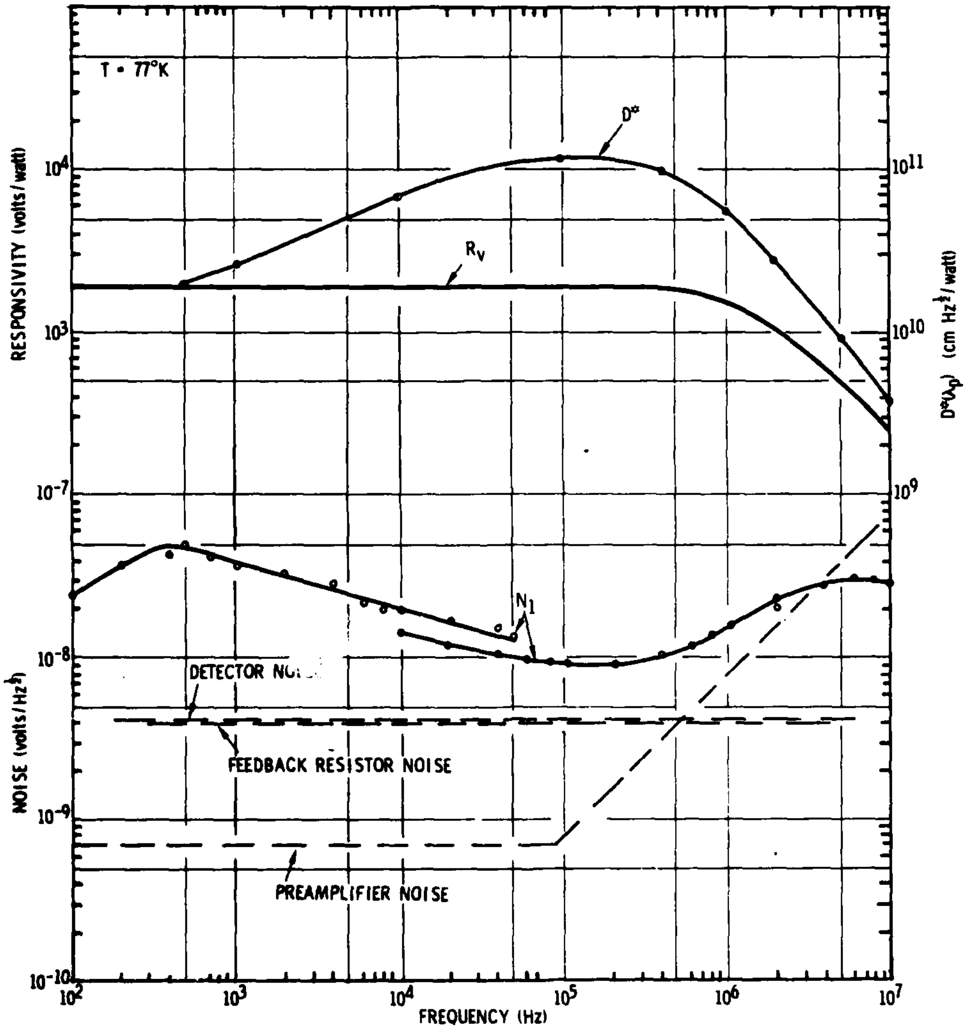

FIGURE 7. FREQUENCY RESPONSE CHARACTERISTICS OF A TYPICAL LARGE AREA PV HgCdTe DETECTOR.
Detector No. 2-132-15

CONCLUSIONS

Techniques were developed for the fabrication of large area PV HgCdTe quadrant detector arrays for use in 3.85-μm DF laser detection applications. P-type base material with acceptor concentrations of about 1×10^{15} per cm^3 was used to minimize device capacitance. An n^+ layer was produced on the p-type base material by boron ion implantation to minimize series resistance. A low-noise current-mode preamplifier was constructed to provide optimized detector performance in the 1- to 5-MHz frequency range.

The measured response time of the detector-preamplifier combination was approximately 100 ns and $D^*(\lambda_p)$ values of about 5×10^{10} cm $Hz^{\frac{1}{2}}$/watt were obtained at 1 MHz.

ACKNOWLEDGMENTS

Others who contributed to this work are R.A. Cole, who produced the HgCdTe crystals, D.J. Calhoun, who performed Hall effect measurements, K.J. Riley, who assisted in device measurements, and J.S. Lee and S.P. Ryan, III, who designed and built the preamplifier. Their help is gratefully acknowledged. J.M. Steininger also made significant contributions to this program during the early phases. The program technical monitor at Ft. Monmouth was Claire Burke. Her interest and support were essential to the success of this program.

APPENDIX — DETECTOR-PREAMPLIFIER ANALYSIS

For high frequency applications, a current-mode preamplifier is desired to reduce the capacitive loading due to the high junction capacitance of the PV detector. Preamplifier noise may be the limiting noise at high frequencies. Therefore, an analysis of detector frequency response and sensitivity must also include the preamplifier. In this appendix, such an analysis is performed.

SIGNAL RESPONSE

Figure 8 shows the equivalent circuit for the PV detector-preamplifier combination. Consider first the signal current produced by the ideal current generator i_s. If detector series resistance is not negligible, the signal current reaching the preamplifier input will be given by

$$i_i = i_s \left(\frac{Z_j}{Z_j + r_s} \right) \tag{1}$$

where the junction impedance Z_j is given by

$$Z_j = R_j \left(1 + \omega^2 R_j^2 C_j^2\right)^{-\frac{1}{2}} \tag{2}$$

At high frequencies, the capacitive reactance may dominate, thus

$$Z_j \approx \frac{1}{\omega C_j} \tag{3}$$

Consider a case where the junction capacitance is 4000 pf. Then, at a frequency of 1 MHz, Z_j = 40 ohms and the series resistance must be much less than this value to avoid loss of signal current.

AD-A118 091 SANTA BARBARA RESEARCH CENTER GOLETA CALIF F/G 17/5
DEVELOPMENT OF LARGE AREA PV HGCDTE DETECTORS FOR 10.6 MICROMET--ETC(U)
JUN 80 P R BRATT, K J RILEY DAAB07-76-C-0803

UNCLASSIFIED NL

2 of 2
AD
A118091

END
DATE
FILMED
9 82
DTIC

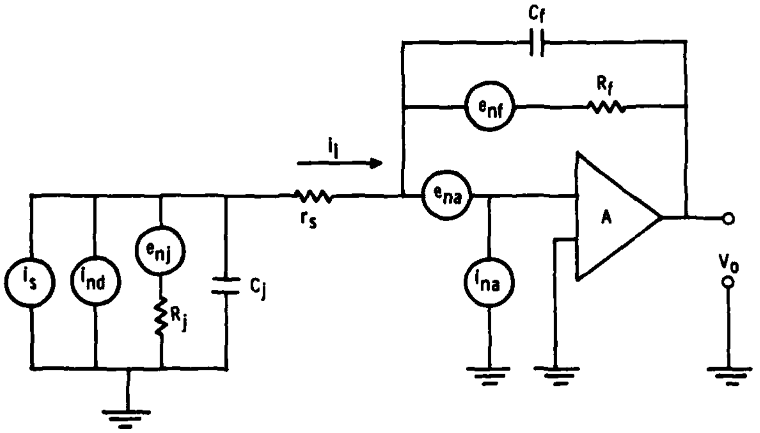

FIGURE 8. EQUIVALENT CIRCUIT DIAGRAM FOR THE PV DETECTOR-PREAMPLIFIER COMBINATION

The output signal voltage from the preamplifier is given by

$$V_{os} = \frac{-AZ_f i_s}{A + 1 + \left(\frac{Z_f}{Z_j + r_s}\right)} \left(\frac{Z_j}{Z_j + r_s}\right) \qquad (4)$$

where the feedback impedance Z_f is

$$Z_f = R_f \left(1 + \omega^2 R_f^2 C_f^2\right)^{-\frac{1}{2}} \qquad (5)$$

and A is the amplifier open loop gain. For low frequencies, where $Z_f \approx Z_j$, $r_s << Z_j$ and $A >> 1$, equation (4) reduces to

$$V_{os} \approx -R_f i_s \qquad (6)$$

The high frequency response is reduced to 1/2 the low frequency value at some frequency given by

$$f_h \approx \left[2\pi \left(\frac{R_f}{1 + A}\right) C_j\right]^{-1} \qquad (7)$$

The factor $R_f/(1 + A)$ is the "equivalent" input impedance of the current-mode preamplifier. It turns out that a practical value for A is about 50 and for R_f about 1000 ohms. Therefore, the junction capacitance C_j must be minimized to allow high frequency response. If C_j = 4000 pf, and the above values for A and R_f are used, then f_h = 2 MHz.

NOISE

The major noise sources are shown in the equivalent circuit diagram of Figure 8. They are: amplifier voltage and current noise, feedback resistor Johnson noise, detector Johnson noise, and detector photon generated shot noise. These combine to give a total noise voltage per unit of frequency bandwidth at the preamplifier output which can be expressed by the equation

$$\frac{V_{on}}{\sqrt{\Delta f}} = \left[\left(1 + \frac{Z_f}{Z_j}\right)^2 \left(e_{na}^2 + i_{na}^2\ Z_f^2\right) + \left(\frac{4kT_f}{R_f}\right) Z_f^2 + \left(\frac{4kT_j}{R_j}\right) Z_f^2 + 2e^2 \eta Q_B A_d Z_f^2\right]^{\frac{1}{2}} \tag{8}$$

The four terms in this equation represent the noise sources in the order listed above.

The preamplifier current noise can be neglected at high frequencies. With this approximation and some algebraic manipulations of equation (8), one can obtain

$$\frac{V_{on}}{\sqrt{\Delta f}} = \left\{\left|\left(\frac{1}{R_f} + \frac{1}{R_j}\right) + j\omega\ (C_f + C_j)\right|^2 e_{na}^2 + \frac{4kT_f}{R_f} + \frac{4kT_j}{R_j} + 2e^2 \eta Q_B A\right\}^{\frac{1}{2}} Z_f \tag{9}$$

This equation shows that the preamplifier voltage noise is boosted at higher frequencies while the other noise terms remain flat. The degree of high frequency boost is dependent on the magnitude of detector junction capacitance. Thus a minimized junction capacitance is necessary not only for extending the signal response to high frequency but also for minimizing noise at high frequency.

The corner frequency at which preamplifier noise boost commences is obtained by setting

$$\left(\frac{1}{R_f} + \frac{1}{R_j}\right) = 2\pi f\ (C_f + C_j)$$

and solving for f. This yields

$$f = \frac{1}{2\pi(C_f + C_j)}\left(\frac{1}{R_f} + \frac{1}{R_j}\right) \tag{10}$$

For a case where $R_f = R_j = 1000$ ohms, $C_j = 4000$ pf and C_f is negligible, one obtains $f = 8 \times 10^4$ Hz. Figure 7 shows an example of the calculated noise contributions as given in equation (9) for a particular detector whose characteristics were similar to those listed above.

The noise boost cannot continue indefinitely but will ultimately be rolled off at higher frequencies due to frequency limitations inherent in the transistors used or to high frequency rolloff purposely built into the preamplifier for stability reasons.

D* VERSUS FREQUENCY

Using equation (4) to calculate responsivity and equation (9) to calculate noise, D* may then be obtained as a function of frequency from the usual equation

$$D^*(\lambda_p, f) = \frac{R_v(\lambda_p, f)\sqrt{A_d}}{V_{on}(f)/\sqrt{\Delta f}} \tag{11}$$

A parametric study was made to ascertain the effect on $D^*(\lambda_p, f)$ produced by variations in the detector parameters R_j, C_j, and r_s. Values for D* versus frequency were calculated holding two parameters fixed, and allowing the third to vary. Figures 9, 10, and 11 show the results of this study. Other fixed parameters used in the calculations were as follows.

R_f = 1000 ohms
A = 50
T_f = 295°K
T_d = 77°K
e_{na} = 0.7 nv/Hz$^{\frac{1}{2}}$
A_d = 0.284 cm^2
η = 0.84
Q_B = 2×10^{15} photons/sec/cm^2
$I_s(\lambda_p)$ = 2.5 amps/watt
λ_p = 3.85 μm

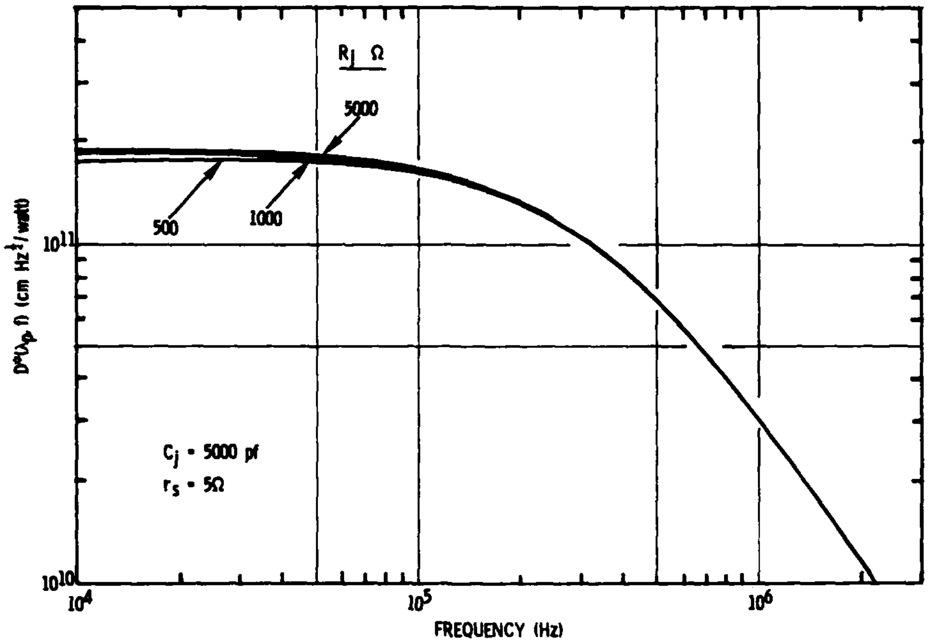

FIGURE 9. HIGH FREQUENCY D* DEPENDENCE ON JUNCTION RESISTANCE

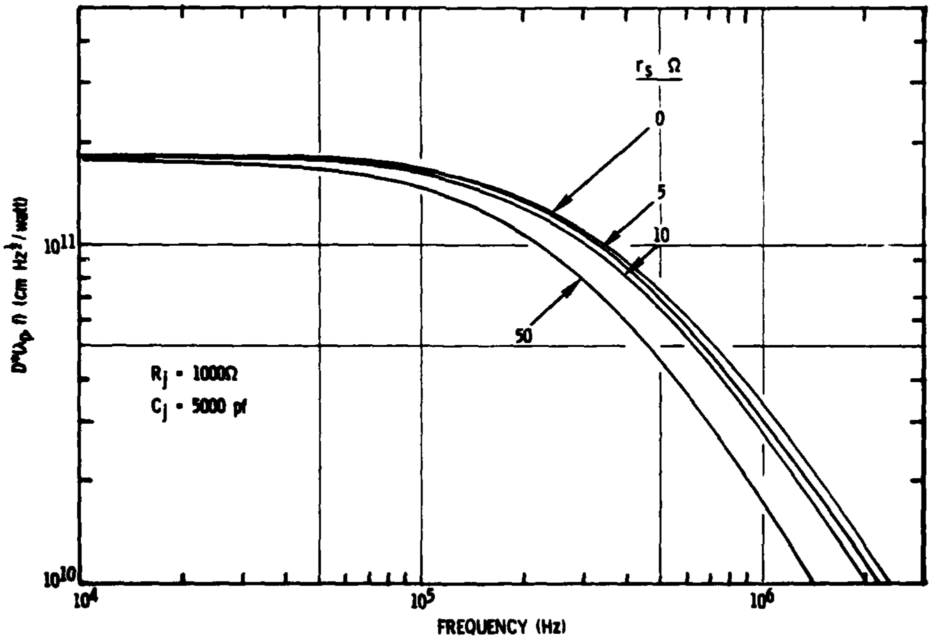

FIGURE 10. HIGH FREQUENCY D* DEPENDENCE ON SERIES RESISTANCE

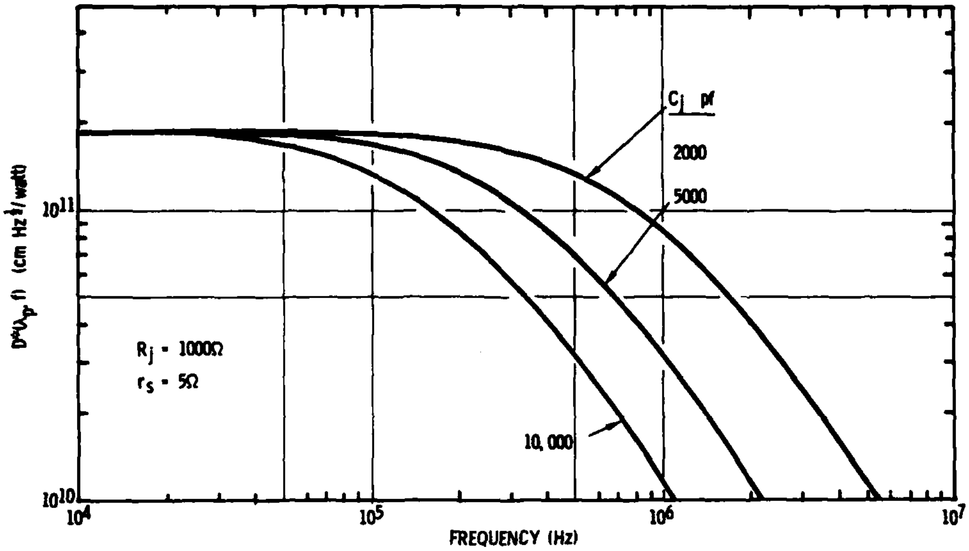

FIGURE 11. HIGH FREQUENCY D* DEPENDENCE ON JUNCTION CAPACITANCE

Figure 9 shows that little effect on D* is produced by variations in R_j. This is as expected since the junction impedance at high frequencies is controlled by the capacitive reactance, not by the junction resistance. Figure 10 shows that series resistance up to 10 ohms does not cause serious degradation of high frequency D*. Figure 11 shows that junction capacitance has the strongest effect on high frequency D*.

Appendix B

LARGE AREA PV HgCdTe QUADRANT ARRAYS FOR LASER DETECTION AT 10.6 μm

Appendix B

LARGE AREA PV HgCdTe QUADRANT ARRAYS FOR LASER DETECTION AT 10.6 μm*

K. J. Riley, P. R. Bratt, and A. H. Lockwood
Santa Barbara Research Center
Goleta, California

ABSTRACT

This paper describes the results of a program to develop large area PV HgCdTe quadrant arrays for detection of pulsed CO_2 laser radiation at 10.6 μm. Nominal detector area for each element of the quadrant was 1.15×10^{-2} cm^2. Detector fabrication consisted of boron ion implantation into p-type base material. Material parameters were chosen to minimize capacitance and series resistance and to maximize junction resistance, quantum efficiency and speed of response. R_oA products at 80°K ranged from 0.24 to 2.82 Ω-cm^2. Typical devices, when operated with an appropriate current mode preamplifier, had response times ranging from 25 to 60 ns and responsive quantum efficiencies ranging from 50 to 74%. High-frequency detectivity ranged from 2.0 to 4.6×10^{10} cm $Hz^{1/2}$/watt at 1 MHz when operated with a Joule-Thompson cryostat.

INTRODUCTION

The objective of this work was to design and fabricate large area PV HgCdTe quadrant arrays for applications in laser tracking with CO_2 lasers at 10.6 μm. Response time and sensitivity of the detectors should be sufficient to detect laser pulses having a 100-ns pulse width thereby requiring a frequency response extending into the [illegible]- to 5-MHz range. The ultimate goal is to develop quadrant arrays with individual element size of 2×2 mm^2 or greater. Here we report the results of some preliminary work using element sizes of 1×1 mm^2.

DETECTOR DESIGN

In designing a sensitive PV detector, four key areas need to be addressed: base material, junction formation, surface passivation, and device processing techniques. For high-frequency applications, these four areas must be optimized to achieve the low series resistance, low junction capacitance and high dynamic impedance required. A detailed analysis of the high-frequency performance of detector-preamplifier combinations has been given in a previous paper.[1]

Figure 1 shows a schematic of the quadrant arrays. N-on-p photodiodes were produced by boron ion implantation into p-type base material. HgCdTe samples cut from crystals grown by both the solid-state recrystallization and zone melt methods were used for diode fabrication. A variety of base dopings ranging from 1×10^{15} cm^{-3} to 1×10^{16} cm^{-3} were produced by diffusion of gold atoms to the solid solubility limit. For the devices reported on in this paper, the acceptor concentration

---

*This work was performed for the U. S. Army Electronics Command, Ft. Monmouth, NJ, under Contract No. DAAB07-76-C-0803, Technical Monitor, C. Loscoe.

ranged from 4 to 8×10^{15} cm^{-3} as shown by analysis of the Hall data presented in Figure 2. Photoconductive decay time data shown in Figure 3 indicate an electron lifetime of 2×10^{-7} sec limited by Shockley-Read recombination.

The doping profile in the boron implanted n-type layer was carefully controlled by adjusting the ion dose and energy. Figure 4 shows the calculated doping profiles in the vicinity of the junction based on Van der Pauw Hall measurements, MIS C-V, and SIMS measurements of boron implanted layers. The junction depth is very shallow so there is little optical absorption on the n-type side of the p-n junction. Minority carrier electrons generated on the p-type side have long diffusion lengths compared to $1/\alpha$, and therefore high collection efficiency is expected.

As indicated in Figure 1, quadrant array processing consisted of delineating mesa structures by standard photoresist masking and etching procedures after ion implantation of the whole surface. The bottom contact to the p-type base material was made by gold plating the backside of the HgCdTe chip before processing the quadrant array. The top contact to the n-type region was evaporated indium. A quarter-wave ZnS or In_2S_3 antireflection coating was applied to the top of the device.

DETECTOR PERFORMANCE MEASUREMENTS

Detector performance characteristics were first measured on quadrant arrays mounted in a metal dewar cooled with LN_2 and then in a glass package cooled with a Joule-Thompson cryostat. The temperature in the metal dewar was 78°K whereas the glass packages ran slightly warmer, around 80°K.

CURRENT VOLTAGE CURVES

Figure 5 shows the current-voltage characteristics of a quadrant array measured at 78°K. The zero bias dynamic resistance, R_o, and the R_oA product range from 145 to 285 Ω, and 1.8 to 3.6 Ω-cm^2, respectively. At 50-mv reverse bias, the dynamic impedance increases by about a factor of 3.5 giving reverse bias resistances of 180 to 1140 Ω. In forward bias the current is limited by a series resistance of about 4.3 Ω.

Figure 6 shows the measured R_oA product as a function of bandgap (determined from cutoff wavelength, λ_c) at approximately 80°K for three quadrant arrays. The R_oA products for the better devices are limited at 80°K by minority carrier diffusion from the p-type base material. These diffusion limited R_oA products have an energy gap dependence of n_i^{-2}:

$$R_oA = \frac{kT}{eJ_s} = \frac{N_a}{n_i^2 e}\left(\frac{\tau_n kT}{\mu_n e}\right)^{\frac{1}{2}}$$

Analysis of the data presented in Figure 6 indicates that the 0.1-eV R_oA products are limited by a $N_a \tau_n^{\frac{1}{2}}$ product of 1×10^{12} cm^{-3} $sec^{-\frac{1}{2}}$. This value is in good agreement with values deduced from bulk lifetime measurements made on p-type HgCdTe. Analysis of lifetime data, similar to that presented in Figure 3, shows that the electron lifetime is Shockley-Read limited and depends on the acceptor doping in the following manner:

$$\tau_n \approx \frac{2\times10^{24}}{N_a^2}$$

therefore, the diffusion limited R_oA product is expected to be independent of doping for these n-on-p device structures.

SPECTRAL RESPONSE

The spectral response for the quadrant array described above is shown in Figure 7. The cutoff wavelength for the four quadrants ranged from 11.0 to 11.5 µm at 78°K, giving a peak spectral response close to the 10.6-µm laser wavelength.

SENSITIVITY CONTOUR

The sensitivity contour was tested with a fine spot scanner. The radiation source was an 800°K blackbody which was focused to a spot size of approximately 0.002 inch in diameter. Translation of the spot across the detector sensitive area was achieved by keeping the spot fixed and moving the detector on an x-y precision translation stage. Figure 8 shows contour curves for the quadrant array designated QD-3. The sensitivity across a quadrant is extremely uniform, deviations being less than ±2%. The dip in the response near the edge of the array is due to the indium contact pad.

PULSE RESPONSE MEASUREMENTS

Detector pulse response times were measured using a GaAs laser diode. The laser output pulse width was 100 ns with a rise and fall time of less than 1 ns. The response time, defined as the time required for the signal amplitude to decay to 1/e of its maximum, ranged from 45 to 60 ns for Array No. QD-3 at 78°K when terminated with a 50-Ω load. These response times are RC limited. For small reverse bias ($\lesssim 0.1$ volt) the response time is proportional to $V^{-0.4}$ (Figure 9) as expected from the dependence of junction capacitance on applied voltage:

$$\frac{C_j}{A_j} = \left(\frac{\kappa\epsilon_o q N_A N_D}{2(N_A + N_D)(V_{bi} \pm V)}\right)^{\frac{1}{2}}$$

At large reverse bias ($\gtrsim 0.2$ volt), the response time has a much stronger dependence, approaching $V^{-2.0}$, presumably due to the reduced dynamic impedance as the bias is increased.

CAPACITANCE VERSUS VOLTAGE

To analyze the junctions formed by the ion-implantation process, some small area diodes were fabricated from the same HgCdTe slice that was used for QD-3. Because of the reduced area these devices exhibited higher zero bias resistance and lower capacitance enabling capacitance versus voltage measurements to be made. Although the junction area (4.64×10^{-4} cm^2) of these devices was 1/26 of the quadrant detector areas, the R_oA products were comparable. Figure 10 shows the junction capacitance as measured by a PAR 410 C-V meter versus reverse bias plotted on a log-log scale. The slope of the straight line region indicates that $C \propto V^{-0.59}$ close to the expected $V^{-0.50}$ for an abrupt junction with $V \geq V_{bi}$, the built-in voltage. The slope of a $1/C^2$ versus

V plot yields a value of 4.3×10^{14} cm^{-3} for the effective junction depletion region doping, $N_AN_D/(N_A + N_D)$. The capacitance per unit area at zero bias was 6.9×10^{-8} fd/cm^2, therefore the capacitance of a single large area quadrant detector is expected to be about 860 pf.

DETECTIVITY

Detectivity data were acquired on these detectors by direct measurements at low frequencies and by an indirect method at high frequencies. At low frequencies, signal and noise measurements were made using a low-noise current-mode preamplifier. At high frequencies, noise data were taken by direct measurements with a HP 312 high-frequency wave analyzer. Current responsivity in the MHz range was calculated by assuming a frequency dependence of:

$$I_R(\lambda_p, f) = I_R(\lambda_p, o) [1 + (2\pi f \tau)^2]^{-\frac{1}{2}}$$

where $I_R(\lambda_p, o)$ is the low-frequency value obtained from blackbody measurements and τ is the detector response time measured with the GaAs laser diode. Voltage responsivity referred to the output of the preamplifier is then

$$R_v(\lambda_p, f) = I_R(\lambda_p, f)R_f$$

where R_f is the feedback resistance. Figures 11 and 12 show plots of the calculated responsivity and measured noise for QD-3. The calculated detectivity at 1 MHz varied from 3.5 to 4.6×10^{10} cm $Hz^{\frac{1}{2}}$/watt. Quantum efficiencies calculated from the low-frequency current responsivity varied from 65 to 75%.

CONCLUSIONS

Tables I and II summarize the detector performance data taken on the two quadrant arrays shipped to ECOM on Phase I of this program. Techniques have been developed for the fabrication of large area PV HgCdTe quadrant detector arrays for use with CO_2 lasers. The p-type base material used in fabricating these arrays had moderately high acceptor concentrations, 5 to 8×10^{15} cm^{-3}. Since lower acceptor concentrations, 0.5 to 1×10^{15} cm^{-3}, are achievable, further reduction in device capacitance and therefore faster response times may be anticipated. The R_oA products for these n-on-p structures are limited by the Shockley-Read lifetime in the p-type base material. Improvements in R_oA product will depend on achieving better lifetimes in p-type material or by using special geometric structures.

ACKNOWLEDGMENTS

The authors would like to give special thanks to R. A. Cole and E. Y. Sutcliffe for the HgCdTe crystals, J. M. Myrosznyk and J. B. Shaw for assisting with process development and detector fabrication, S. L. Price and J. B. Knutsen for assisting with device characterization, and J. S. Lee and S. P. Ryan, III, who designed and built the preamplifier. The program technical monitor at Fort Monmouth was Claire Loscoe. Her interest and support contributed to the success of this program.

REFERENCES

1. P. R. Bratt and A. H. B. Vanderwyck, "Large Area PV HgCdTe Detectors for Laser Detection at 3.85 µm," Proc. IRIS Detector Specialty Group Meeting, U.S. Air Force Academy, Colorado, 22-23 March 1977.

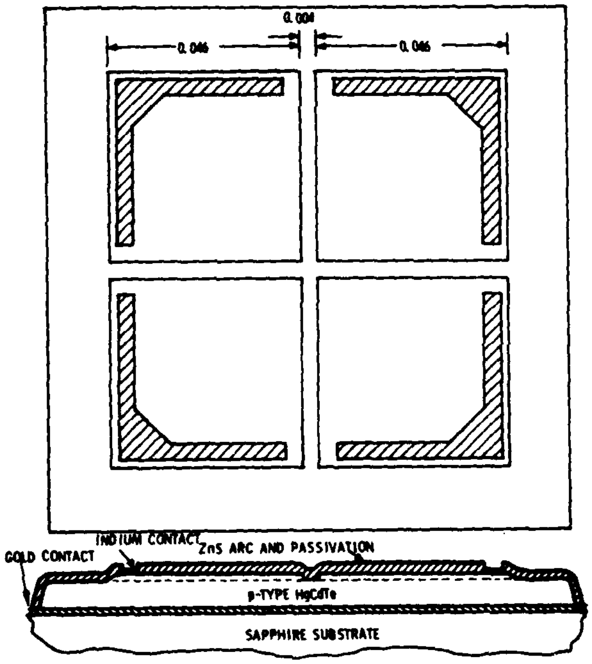

FIGURE 1. SCHEMATIC DIAGRAM OF 1 × 1 MM^2 PV HgCdTe QUADRANT DETECTOR

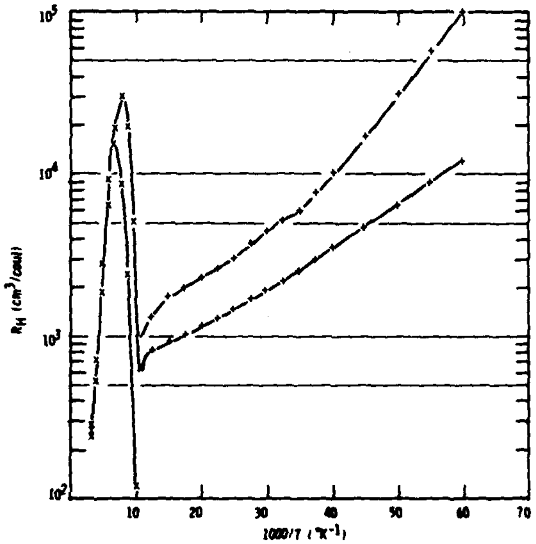

FIGURE 2. HALL COEFFICIENT VERSUS RECIPROCAL TEMPERATURE FOR HgCdTe WAFERS USED TO FABRICATE QUADRANT ARRAYS

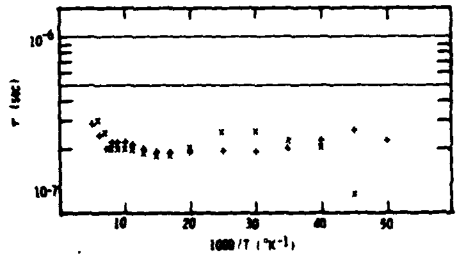

FIGURE 3. BULK PHOTOCONDUCTIVE LIFETIME FOR p-TYPE HgCdTe WAFERS SHOWN IN FIGURE 2

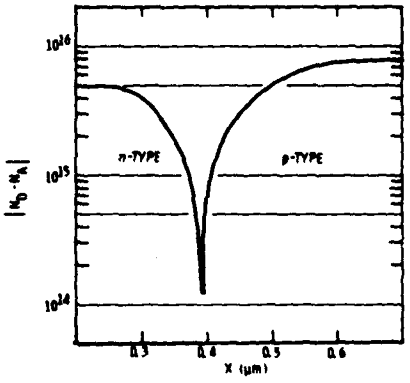

FIGURE 4. CALCULATED DOPING PROFILES IN THE VICINITY OF JUNCTION FOR BORON ION-IMPLANTED DIODES

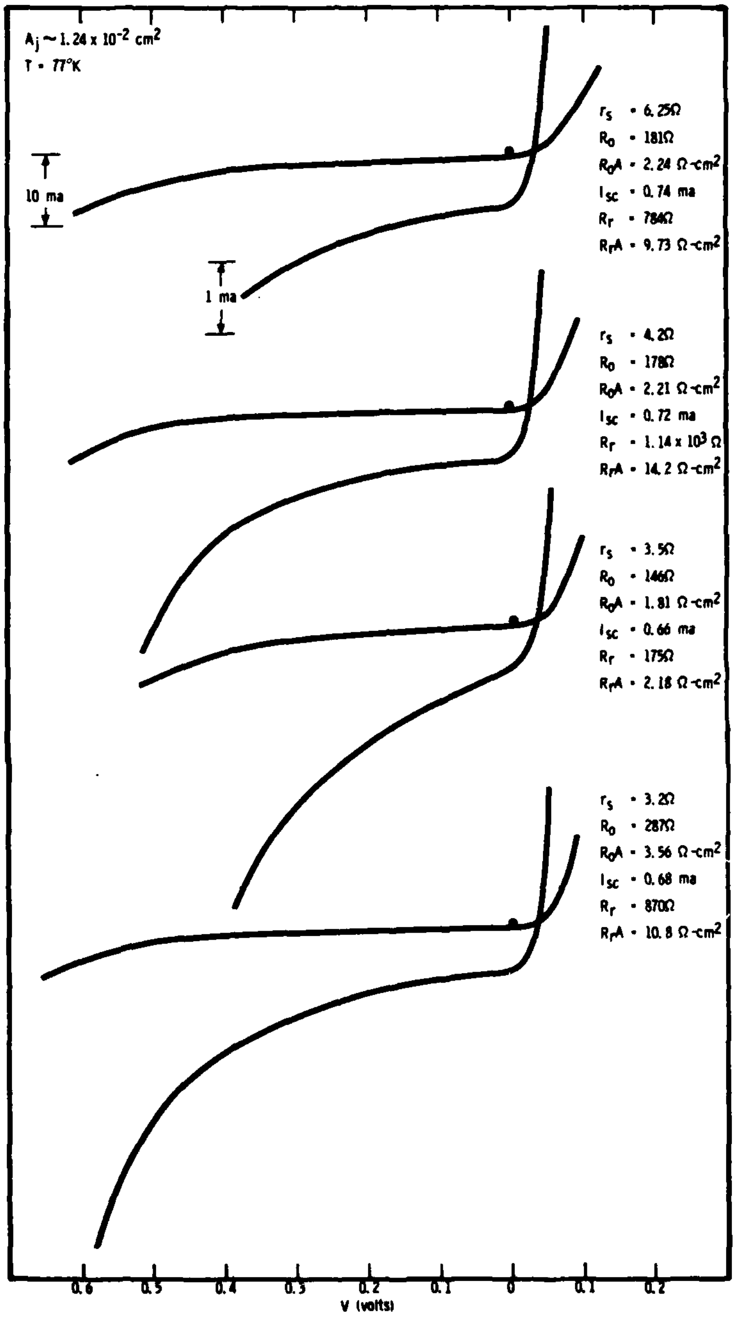

FIGURE 5. I-V CHARACTERISTICS TAKEN AT 78°K FOR PV HgCdTe QUADRANT ARRAY QD-3

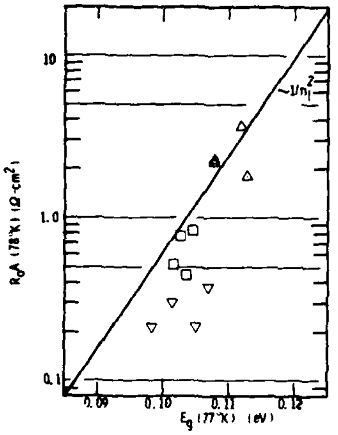

FIGURE 6. R_oA PRODUCT MEASURED AT 78°K AS A FUNCTION OF THE ENERGY GAP

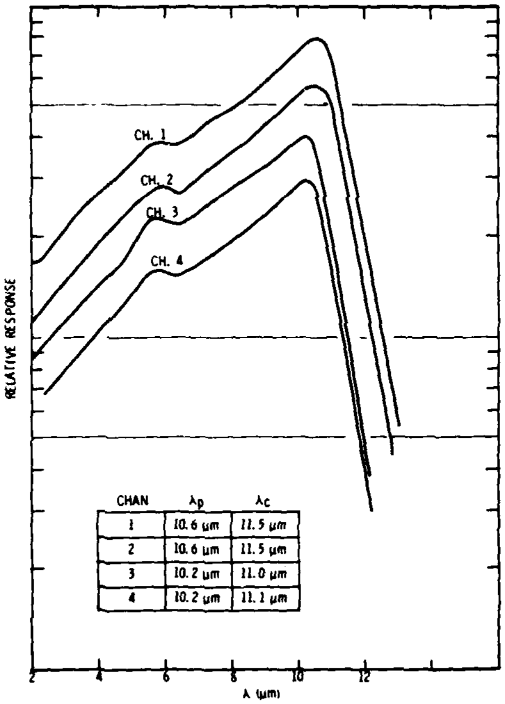

CHAN	λ_p	λ_c
1	10.6 μm	11.5 μm
2	10.6 μm	11.5 μm
3	10.2 μm	11.0 μm
4	10.2 μm	11.1 μm

FIGURE 7. RELATIVE SPECTRAL RESPONSE PER WATT FOR PV HgCdTe QUADRANT ARRAY QD-3

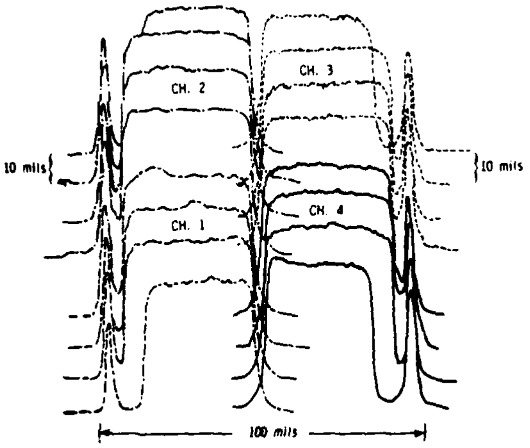

FIGURE 8. SENSITIVITY CONTOUR OF QD-3

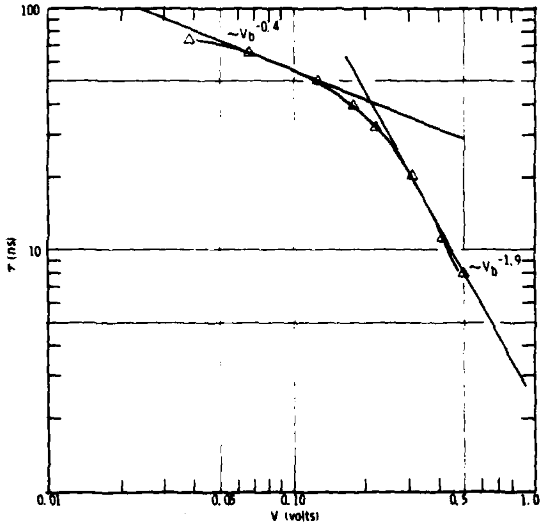

FIGURE 9. RC LIMITED LIFETIME PLOTTED AS A FUNCTION OF REVERSE BIAS

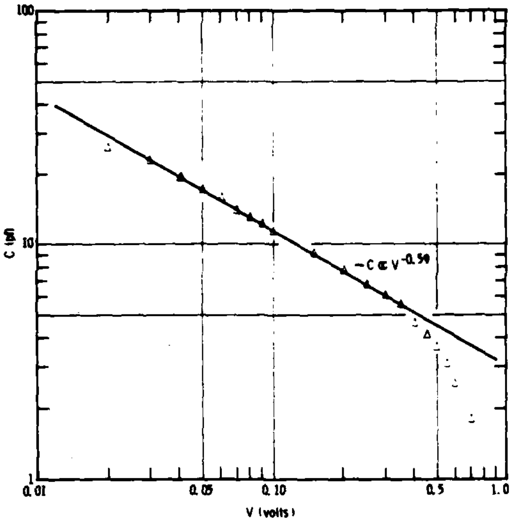

FIGURE 10. JUNCTION CAPACITANCE AS A FUNCTION OF REVERSE BIAS FOR A SMALL AREA DIODE

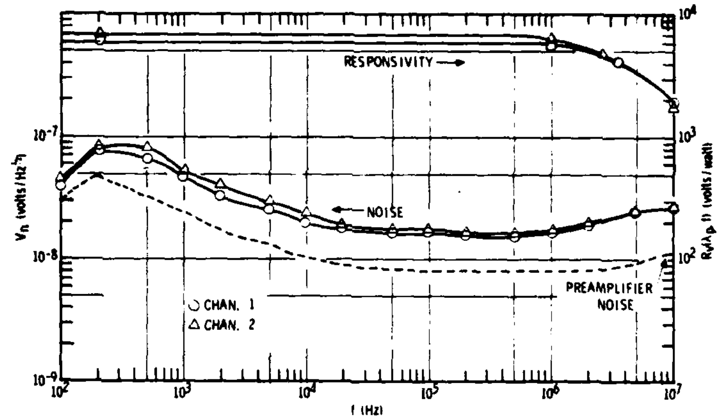

FIGURE 11. RESPONSIVITY AND NOISE AS A FUNCTION OF FREQUENCY FOR CHANNELS 1 AND 2 OF QD-3

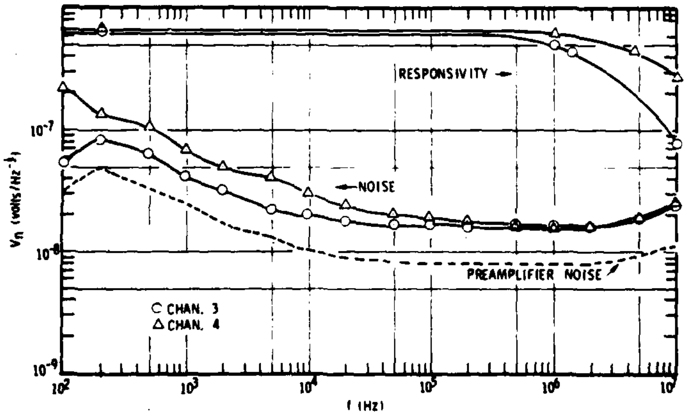

FIGURE 12. RESPONSIVITY AND NOISE AS A FUNCTION OF FREQUENCY FOR CHANNELS 3 AND 4 OF QD-3

TABLE I. DETECTOR PERFORMANCE DATA FOR PV HgCdTe QUADRANT ARRAY QD-3, T ≈ 80°K

MEASUREMENT	CH. 1	CH. 2	CH. 3	CH. 4
RESPONSE TIME (ns)	45	60	110	35
λ_c (μm)	11.5	11.5	11.0	11.1
R_0A (Ω-cm^2)	1.55	1.59	1.24	2.82
I_{sc} (ma)	0.75	0.84	0.78	0.76
$\eta(I_{sc})$ (%)	51	57	60	57
$\eta(I_r)$ (%)	64	74	68	72
SPOT SCAN UNIFORMITY (%)	±2	±2	±2	±2
I_r (λ_p, 0) (amps/watt)	5.90	6.89	6.30	6.69
I_r (λ_p, 1M) (amps/watt)	5.68	6.45	5.18	6.53
R_v (λ_p, 0) (volts/watt)	5900	6890	6300	6090
R_v (λ_p, 1M) (volts/watt)	5677	6447	5183	6534
D^*(λ_p, 1M) (cm Hz$^{1/2}$/watt)	4.00×10^{10}	4.38×10^{10}	3.52×10^{10}	4.61×10^{10}
f_{3db} (MHz)	3.5	2.7	1.4	4.5

TABLE II. DETECTOR PERFORMANCE DATA FOR PV HgCdTe QUADRANT ARRAY QD-4, T ≈ 80°K

MEASUREMENT	CH. 1	CH. 2	CH. 3	CH. 4
RESPONSE TIME (ns)	30	25	25	10
λ_c (μm)	11.6	12.6	11.8	12.2
R_0A (Ω-cm^2)	0.39	0.24	0.24	0.32
I_{sc} (ma)	1.01	0.98	0.98	1.02
$\eta(I_{sc})$ (%)	67	52	62	60
$\eta(I_r)$ (%)	74	52	41	53
SPOT SCAN UNIFORMITY (%)	±3	±5	±5	±4
I_r (λ_p, 0) (amps/watt)	6.89	5.31	3.94	5.21
I_r (λ_p, 1M) (amps/watt)	6.77	5.25	3.89	5.20
R_v (λ_p, 0) (volts/watt)	6890	5310	3892	5210
R_v (λ_p, 1M (volts/watt)	6771	5246	3892	5200
D^*(λ_p, 1M) (cm Hz$^{1/2}$/watt)	3.73×10^{10}	2.72×10^{10}	2.02×10^{10}	2.69×10^{10}
f_{3db} (MHz)	5.3	6.4	6.4	15.9

DATE
FILMED

8